ACTA MATERIALIA TRANSYLVANICA

Material Sciences Publications

Volume 6, Issue 1

ERDÉLYI MÚZEUM-EGYESÜLET
Cluj-Napoca
2023

A folyóirat megjelenését támogatta a Communitas Alapítvány, a Magyar Tudományos Akadémia, a Bethlen Gábor Alapkezelő Zrt. és az EME Műszaki Tudományok Szakosztálya / The publication of this magazine was supported by the Communitas Foundation, by the Hungarian Academy of Sciences, by the Bethlen Gábor Fund and by the TMS – Department of Engineering Sciences.

Kiadó / Publisher: Erdélyi Múzeum-Egyesület
Felelős kiadó / Responsible publisher: Biró Annamária
Olvasószerkesztő / Proofreader: Szenkovics Enikő (magyar), David Speight (English)
Szerkesztőségi titkár / Editorial secretary: Kisfaludi-Bak Zsombor
Borítóterv / Cover: Könczey Elemér
Nyomdai munkálatok / Printed at: F&F International Kft., Gyergyószentmiklós

ISSN 2601-1883, ISSN-L 2601-1883
DOI: 10.33924/amt-2023-01
A folyóirat honlapja: https://www.eme.ro/publication-hu/acta-mat/mat-main.htm
The journal website: https://www.eme.ro/publication/acta-mat/mat-main.htm

Az *Acta Materialia Transylvanica. Anyagtudományi Közlemények* az Erdélyi Múzeum-Egyesület (EME) Műszaki Tudományok Szakosztályának folyóirata, amely az anyagtudományok területéről közöl tudományos közleményeket: szakcikkeket, összefoglalókat (szemléket), tanulmányokat. A folyóirat célja összképet adni kiemelten a Kárpát-medencei kutatási irányokról, tudományos eredményeiről, s ezt széles körben terjeszteni is. A folyóirat az EME felvállalt céljaihoz híven a magyar szaknyelv ápolását is támogatja, így a nyomtatott folyóirat magyar nyelven jelenik meg, mely az Erdélyi digitális adattárban elérhető (https://eda.eme.ro/handle/10598/30356). A széles körű nemzetközi terjesztés érdekében a folyóirat teljes angol nyelvű változatát is közzétesszük.

Acta Materiala Transylvanica – Material Sciences Publications – is a journal of the Technical Sciences Department of the Transylvanian Museum Society, publishing scientific papers, issues, reviews and studies in the field of material sciences. Its mission is to provide and disseminate a comprehensive picture focusing on research trends and scientific results in the Carpathian basin. In accordance with the general mission of the Transylvanian Museum Society it aims to support specialized literature in Hungarian. The printed version of the journal is published in Hungarian and is available in the Transylvanian Digital Database (https://eda.eme.ro/handle/ 10598/30356). However, we would like to spread it internationally, therefore the full content of the journal will also be available in English.

Tartalom / Content

sciendo

Acta Materialia Transylvanica 6/1. (2023) 01–08.
DOI: Hungarian: https://doi.org/10.33923/amt-2023-01-01
English: https://doi.org/10.33924/amt-2023-01-01

ACTA MATERIALIA TRANSYLVANICA

The Reconstruction of the Creation of the Holy Crown

Miklós BARABÁSSY

KEMPELEN Tudósakadémia Alapítvány, https://barabassymiklos.academia.edu, Budapest, Hungary, miklos.barabassy@gmail.com

Abstract

Determining the place and time of an artefact's origination starts with archaeometry surveys. The aim of the study of the Holy Crown is to characterise in detail the parts of the crown – the frame, the filigree and the sockets, i.e. the metal parts – and the decorations (enamel, gemstones, beads), to determine the exact composition of the materials and to discover the place of origin. Archaeometry also includes the reconstruction of the technical and technological processes associated with artefacts. The absolute age of the artefacts can be determined using organic materials such as adhesives. This is basically a natural science. If we include the auxiliary sciences - photo-optical data recording, 3D modelling, which allows us to continue the study on the computer – it is possible to determine the relative date and place of the crown parts, using parallels with applied art, palaeography, etc. To date, no systematic archaeometry study has been carried out on the Holy Crown. There have been photographs, geometric measurements, visual inspections and descriptions by jewellers and engineers. If we want to write a scientific summary, we have a lot to draw on. The present article is such a summary, in which we attempt to reconstruct the technology of the Holy Crown, with the aim of pointing out the need for a complete archaeometry study.

Keywords*: Holy Crown, technology, archaeometry.*

1. Introduction

The Holy Crown shown in **Figure 1** is made up of two distinct parts; these are shown in **Figure 2**. The first is the vault, also known as the Latin crown, a cross-strap, which, judging by visual inspection, is made of a purer (less alloyed) material. The surface of the cross-straps is densely decorated. It is a common representation of the techniques and styles used in the jewellery workshops of Western Europe and the northern Alps. Latin inscriptions appear on the enamel designs.

The other part is the hoop crown, also known as the Greek crown, which reflects the shape of an open crown without the cross-strap. The material of the hoop appears to contain more alloying material than the support plates of the cross-strap. The enamel images belong to two strikingly different groups. One group consists of figural enamel designs with Greek inscriptions, while the other group consists of translucent glazed enamel, i.e. an ornamental element in the form of scales.

The technique is not very uniform, sometimes rough; the metalworkers described it as a work without a workshop.

From the early 1800s, when it became possible for the general public to view the crown, the names Greek and Latin crowns became widespread, and with them the two-crown theory. The essence of this is that there was an open crown originating in Byzantium and an attached vault of western origin. Before this, there was a consensus belief that the Holy Crown had been handed down to us from St Stephen, our first king, and that only those who were crowned with this crown could be kings. Already from the 13th century onwards, the Holy Crown doctrine, which is a legal system and a constitution, is gradually being developed. According to this view, the supreme sovereign authority belongs to the Holy Crown, and for several hundred years the people of the Holy Crown have been the Hungarian nation.

Habsburg absolutism could not tolerate this, and continually tried to diminish the freedom of

Figure 1. *Front view of the Hungarian Holy Crown. (Photo: György Bence Kovács)*

Figure 2. *Two separate structural units of the Hungarian Holy Crown: the crossband (top) and the rim (bottom).*

customary law, and subsequent communist and socialist governments tried to abolish the respect that had been built up around the Holy Crown and to adopt a constitution to reflect this.

When the Holy Crown was returned to Hungary at the beginning of 1978, a Crown Commission was set up, which did indeed take a scientific approach to the Crown, but some historians, influenced by the political methods of the time and of the past, anticipating the conclusions of the Commission, published several studies and books: all of them to prove the two-crown theory. Yet a group of five goldsmiths **[1]** managed to examine the crown twice. They, however, came to a position contrary to that of the historians, namely the unitary crown theory. The result was that the then Minister, on the recommendation of the Crown Commission, ordered all publications and films on the Holy Crown to be edited by historians **[2]**.

This move led to a split in the interested public. The Department of Humanities of the Academy of Sciences is the hallmark of one part, the smaller one: the adherents of the two-crown theory and the belief that the Holy Crown could certainly not have been the crown of St Stephen. This, let's face it, is destructive to the nimbus of the Holy Crown. The other part, the larger part, is represented by the so-called alternatives, who, whatever the philosophers may say, still consider the Holy Crown to be the crown of St Stephen, which is still the basis of the unity of the Hungarian nation and the foundation of our Constitution.

Well, it is this strong opposition that got me thinking. By their very nature, the humanities are not an exact science, and indeed, they deliberately exclude the representatives of exact science from their circles. In my opinion, whatever the results of the exact sciences may be, it will not destroy respect any more, but it may open up the possibility of a convergence of views in the light of established facts.

The only proof of the creation of the Holy Crown is the crown itself. My work is aimed at using the possibilities of applied scientific investigation to point out the technical regularities, and at using the interdisciplinarity of the natural sciences to bridge the gap between the results of the investigations offered by modern technology and those of the humanities.

2. Experimental and computational methods and source materials used for the thesis

As a project and process engineer, I have gained extensive experience in the creation of CAD models for engineering. As a first step, I created a 3D model of the Holy Crown using a CAD program. To do this I obtained, mainly from the photographer Károly Szelényi, a series of photographs of the Holy Crown taken twice, 20 years apart. I also used the data actually measured with a caliper by the goldsmith's group [1]. I also had access to photographs by Joachim Szvetnik [2]. During the months of modelling I had the opportunity to learn about the challenges that a 9th-13th century goldsmith and enameller had to face. So I looked for procedural descriptions from that period.

In the early 12th century, Theophilus Presbiter [3] summarised this. Again, it was of high importance to learn about enamel making and the soldering process of the time, which had been forgotten. Fortunately, Eghart Brepohl, the internationally renowned goldsmith, reconstructed Theophilus Presbiter's techniques and explained them in a book. But also of great help was Bosselmann Ruibicke, who compared Theopholus' technology with the technical descriptions of the Byzantine goldsmiths of 100 years earlier [4]. I also found a detailed description of the soldering process used to solder the filigree and the various settings [5]. It was a great help to take advantage of the facilities offered by my second home, the university library in Cologne.

It is important to underline the activities of the Crown Commission, which was founded in 1978 and which has produced a great deal of work and results. I have also been able to obtain the protocols of the Crown Commission thanks to the heritage of Joachim Szvetnik in Tiefkút [2]. Of course, there is not enough space here to list all the source material, but I must mention the important material of two Holy Crown conferences. One was held in Budapest in 1983 [6], the other in Paris [7]. Their papers were published, unfortunately only in foreign languages. I later published edited versions of the more important lectures on academia.edu, where I now have a following from more than 100 countries (more than 16,000 readings), including byzantologists, historians and art historians from universities around the world.

All my claims have been verified by experiments. I have obtained specimens in pure gold, but I have also used copper to test for fracture or other external influences. I describe these in detail in my book *The Holy Crown through the eyes of an engineer*. [8]

Last but not least, in order to verify the scientific validity of my claims, I have made a replica of the crown myself, which is an exact copy of the original, including the particularities that deserve special attention in the creation of the crown.

3. The key features of the manufacturing of the Holy Crown

The shape of the hoop ring is almost circular, with the cross-strap attached centrally (**Figure 3**). The other features are described separately.

3.1. Feature 1

The angles between the stems of the cross-strap are different from each other, in this sense the strap is inaccurate.

The rim is divided into eight wedge fields by eight enamel image sockets, with high precision. The front and rear wedge fields are wider, which suggests that this ring was probably made as a crown ring. The width of the other gem fields is identical (**Figure 4**).

3.2. Feature 2

The partition of the hoop is independent of all other crown parts. Thus the hoop ring could be a semi-finished piece used to make the crown.

If the sockets and gemfields on either side of the centre line of the frontal field are placed side by side, extended from the centre line, it is visible that the Kon side is 4.7 mm shorter (**Figure 4**). The distance between Kon and Damian is 1 mm nar-

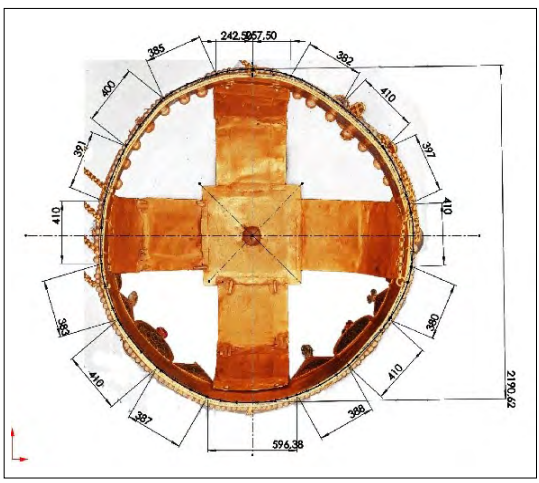

Figure 3. *Fit of the cross strap to the hoop.*

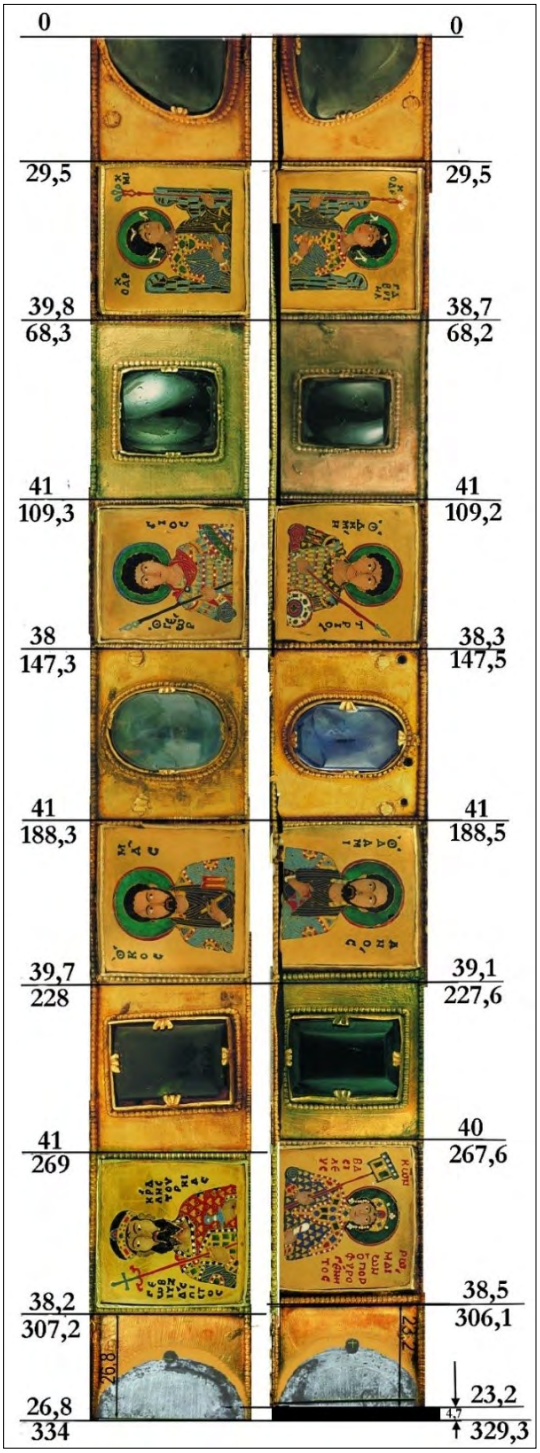

Figure 4. *The crown of the Hungarian Holy Crown lay out, with the size of the individual parts holding the decorations and the position of the circumference measured from the centre line of the frontal part.*

rower than the other gemfields. This means that the narrower side of the solder line of the stone field is increased by 1 mm, which optically reduces the asymmetry (**Figure 5**).

3.3. Feature 3

The solder line of the cross-strap ends visible in the back stone field is asymmetrical and is centered on the centerline of the back cross-strap stem.

Looking at the rear view of the crown (**Figure 5**) it is noticeable that the centre line of the rear panel is not in the centre line of the rear stone field, but is exactly in front of the rear stem of the cross-strap, in line with it. It can also be seen that the starter ring supporting the rear spike is also in line with it. These discrepancies are not accidental, however, but are related to other features.

3.4. Feature 4

The rear pediment element and the starter ring which supports the rear pendilias, although fixed to the hoop, are not aligned with the hoop but with the rear stalk of the crossbar.

This asymmetry is also repeated in the frontal part. The central socket of the frontal part is the Christ socket, which has triangular and curved pediment elements on either side, with the same common spread. Thus, their position is determined by the Christ socket, which, like the back moulding, is aligned with the front cross straps stem rather than with the central axis of symmetry of the front (front) field (**Figure 6**).

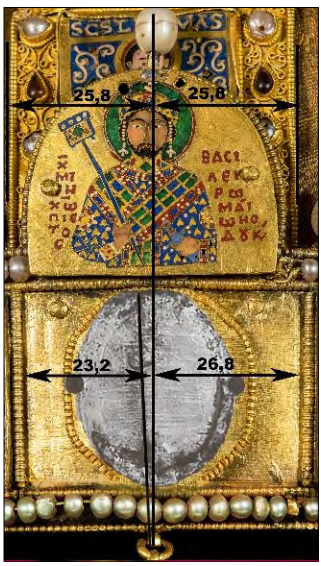

Figure 5. *Deviation from symmetry in the back field.*

3.5. Feature 5

The central image of Christ on the front of the frontal pediment is aligned with the forward stem of the cross-strap, so it is also asymmetrical in relation to the ring of the hoop; it is positioned exactly in front of the stem of the cross-strap. But the image also shows that the rings holding the true pearl string are also in line with the axis of symmetry of the cross-strap stem.

As a complement, it is also worth studying the welding of the hoop ends (**Figure 7**).

The joining of the ends is rather rudimentary and appears to be an afterthought. The two small holes that hold the ends together are not filled with solder and only a spot solder joint is visible (**Figure 7**). This is explained by the alignment required during assembly. It can also be seen that there was originally an oval gem, now replaced by an octagonal one. On the inside, the holes used for joining are clearly visible (**Figure 8**). The above features allow us to establish the technology used to produce the Holy Crown as a unique handcrafted product. A flowchart of the production process is shown in **Figure 9.**

4. The technology of the Holy Crown

The Holy Crown has two parts, the hoop ring and the cross strap, which do not fit to any other part of the crown, they were created independently. Like a hat, a crown has only one important dimension: the diameter of the hoop. So a hoop had to be first designed. In the case of the Holy Crown, the present-day hoop was divided into 8s with geometrical precision. Therefore, it can be argued that this does not necessarily prove that it was made for the cross-strap, but it does not rule it out.

In the next stage of crown creation, because of the features described in the previous chapter, it is not possible to imagine that the decoration of the hoop could have been made without the cross strap. Thus, the third part, the pediment, the rings holding the pendilias, the large stone at the back and the rings holding the string of pearls below the image of Christ form a separate crown part, since they are attached to the hoop ring but fit the cross-strap. The style of decoration of the cross-strap is coherent and was also created independently of the rest of the crown. It is important to note that the process used for the construction

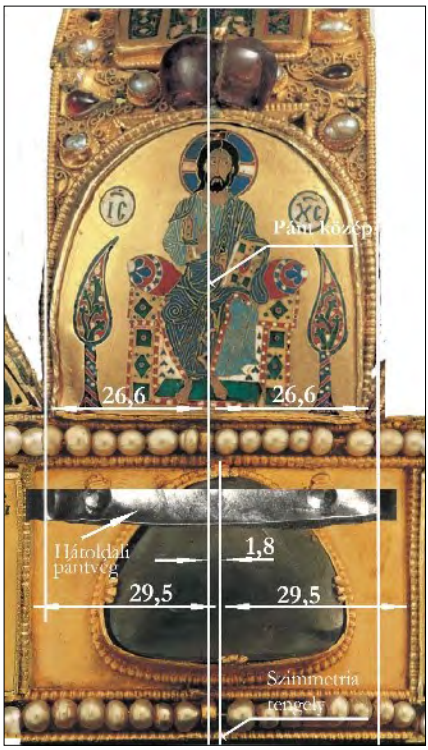

Figure 6. *Symmetry deviations of the frontal fields.*

Figure 7. *Tyre end weld location.* **[7]**

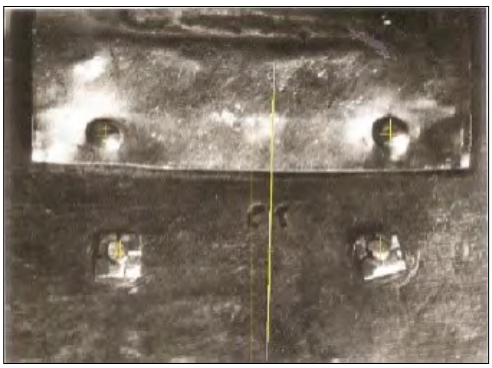

Figure 8. *Solder line of the hoop ends as seen from the inner side.* **[2]**

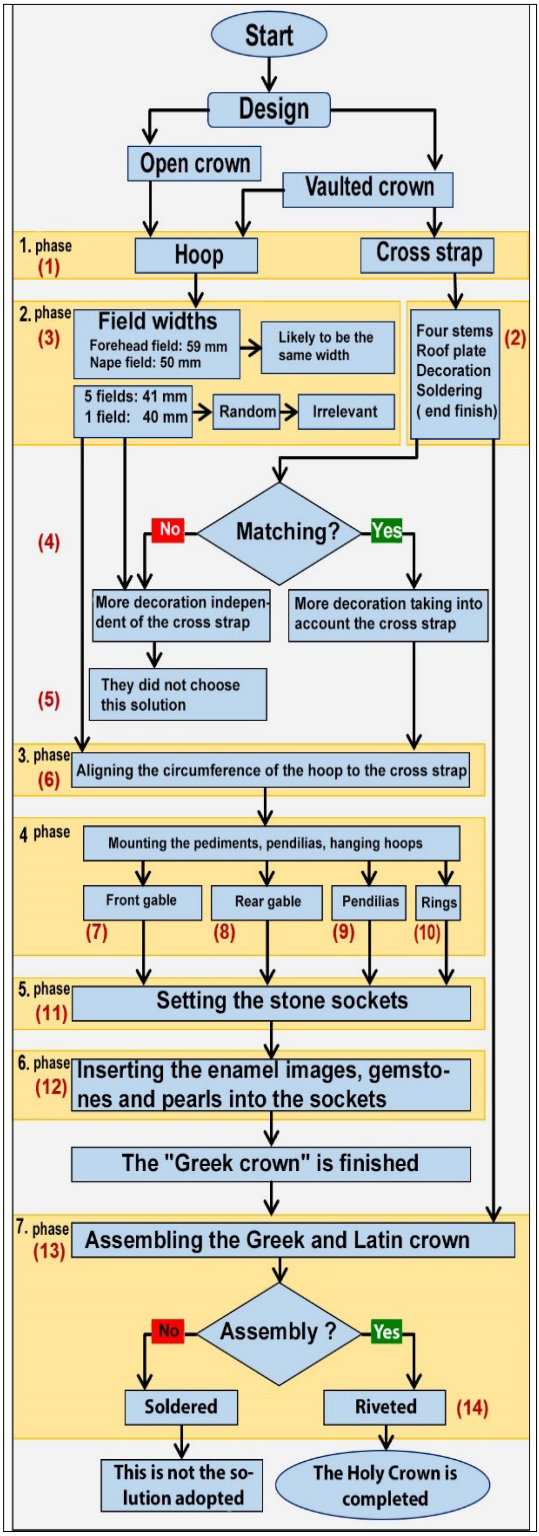

Figure 9. *Reconstruction of the technological flowchart of the manufacturing of the Holy Crown.*

implies not only a high level of expertise, but also a much higher degree of artistic expression than the „workshop-less" eclectic solution of the hoop. These two parts are assembled in the last step by riveting. The cross-strap was joined to the semi-finished tyre ring. A fitting direction had to be chosen, which in the case of the crown was the transverse direction, because space is tighter there and the asymmetry is less apparent in the case of wider fields. The fitting possibilities for the cross strap do not extend to the angles between the stems. Also, fitting the hoop could only be done by shortening the length of the hoop by cutting it out. Indeed, a piece was cut from it so that the ends were welded together exactly on the centre line of the cross-strap; this is shown in **Figures 5.**, **6** and **7**.

The rear cushion socket element is also not on the centre line of the field below it, but on the centre line of the rear crossbar. In the grayscale image, the dismantled current back stone is shown behind in **Figures 5.**, **7**.

The socket of the central image (Christ) of the pediment is clearly visible just in front of the front stem of the cross-strap. But it is equally visible that the rings holding the bead strings are also exactly aligned with the centre line of the cross-piece (**Figure 6**). Of course, the contemporary goldsmith had the possibility to place the pediment and the other ornamental elements listed symmetrically to the hoop division, but he did not do so; he aligned them with the cross-strap for a better appearance.

The back stone is secondary. After dismantling, you can see that the soldering is very rudimentary, spot soldered, and the material has not even flowed into the holes where it is being joined.

Figure 7 and **Figure 8** show the slightly inclined orientation of the hoop ends and the mounting holes from the outside and inside. The front ring supporting the rear pendilias is also aligned with the solder line of the ends in the direction of the rear cross strap stem.

5. Theses

The creation of the lower part of the Holy Crown is therefore not necessarily linked to a workshop or a specific time. It follows from the scientifically proven technological reconstruction that, although the pediments, the pendilias, the string of bead holders and the large stones are all part of the hoop crown, they were aligned with the cross-piece. So, in the process of creation, the place-

ment of the moulding and the dangles preceded the creation of the crossband, as they are aligned with it. A reproduction of the crown was made to verify the technology. By following the technological process, the creation can be repeated as often as you like and the result will always be the same. The condition of scientificity is thus verified.

The novelty of the thesis is related to the technology described. Knowing and using it, it is possible to determine what further investigations are needed to elucidate the place and time of the manufacture of the Holy Crown.

6. Application

The technological process described above cast doubts on the current mainstream philosophical opinions. Of course, the humanities cannot be the subject of this thesis, but my work opens up for the first time a justified possibility to involve the exact sciences in the study of the Crown and to point out what further investigations are needed to determine the production of the Holy Crown. These investigations are identified and defined by standard archaeometry.

In this context, I must highlight the most widely used for artefact examination, the XRF examination. Knowing the trace elements of gold plates can help to determine the place and time of their production, as there are already databases of tests carried out on artefacts. This alone, however, is not enough: art history and historical verification are also needed. It is, however, possible to determine, for example, whether the material of the pad and the tyre are the same. XRF tests can be used to determine the chemical composition of the enamel and jewel settings, thus making it possible to determine whether the parts of the Holy Crown belong together. By grouping the same gold alloy settings in the same group, it is possible to determine which parts were made in the same workshop at roughly the same time.

Along the same lines, if the blue and green enamel on the pediment matches with the blue and green enamel on the apostles of the cross-strap, it is highly probable that the whole crown was assembled in the same workshop.

Organic materials have been found in other prestigious museums. Dendrochronological or carbon isotopic analysis of the organic material may be able to infer certain repairs or dates of manufacture. These studies would make a major contribution to our understanding of how the Holy Crown was made.

7. Verification of the technology

In order to verify the correctness of the technology used, I have also found it necessary to make a crown copy. This copy is shown in **Figures 10** and **11**.

Even with the tools of the time (calipers, rulers), the exact division of the hoop was not particularly difficult. The crosspiece, on the other hand, was made in five parts by first soldering the filigree, the bead wire and the sockets to the stems and the roof plate, and then by riveting them together and soldering them. The cross strap dome shape and the soldering together are always done with some inaccuracy. The question arises, before the pediment is constructed or fitted, to what should it be fitted: to the hoop or to the cross strap?

The early goldsmith chose the cross strap. If this decision is followed for each crown made, the re-

Figure 10. *Copy of the Holy Crown from the front .*

Figure 11. *Copy of the Holy Crown from behind.*

sult will always be the same. Although the pediment and other ornamental elements are part of the „Greek crown", they are still aligned with the cross strap! This justifies the correctness of the technology of reconstruction

References

[1] Csomor L.: *Magyarország Szent Koronája*. Vay Ádám Múzeum Baráti Köre, Vaja, 1986. 29–34.
[2] Szvetnik Joachim hagyatéka: Koronabizottsági jegyzőkönyvek, jegyzetek, előadások anyaga, a mélykúti könyvtárból. A polgármester engedélyével. Mélykút 2017.
[3] Brehpohl E.: *Theophilus Presbyter und die mittelalterliche Goldschmiedekunst*. Böhlau, Wien, 1987.
[4] Bosselmann-Ruickbie A.: *Das Verhältnis der „Schedula diversarum artium" des Theophilus Presbyter zu byzantinischen Goldschmiedearbeiten: Grenzüberschreitende Wissensverbreitung im Mittelalter?* In: *Zwischen Kunsthandwerk und Kunst. Die „schedula diversarum artium"*. (eds.: Mauriège M., Westermann-Angerhausen H., Speer A.), DeGruyter, Berlin, 2014, 333–368.
[5] Eilbracht H.: *Filigran- und Granulationskunst im wikingischen Norden: Untersuchungen zum Transfer frühmittelalterlicher Gold- und Silberschmiedetechniken zwischen dem Kontinent und Nordeuropa*. Rheinland-Verlag, Köln, 1999.
[6] Köpeczi B., Székely Gy., Buckton D.: *Insignia Regni Hungarie I. Studien zur Machtsymbolik des mittelalterlichen Ungarn*. Magyar Nemzeti Múzeum, Budapest, 1983.
[7] *Acta Historiae Artium 43*. Akadémiai Kiadó, Budapest, 2002.
[8] Barabássy M.: *A magyar Szent Korona mérnöki szemmel*. PenClub, Budapest, 2020.

sciendo

Acta Materialia Transylvanica 6/1. (2023) 9–13.
DOI: Hungarian: https://doi.org/10.33923/amt-2023-01-02
English: https://doi.org/10.33924/amt-2023-01-02

ACTA MATERIALIA TRANSYLVANICA

Investigation of Corrosion Caused by Iron Contamination on the Surface of Stainless Steel Plates

Csaba BREZNAY,[1] Balázs VARBAI[2]

[1] *Budapest University of Technology and Economics, Faculty of Mechanical Engineering, Department of Materials Science and Engineering. Budapest, Hungary, breznay.csaba@edu.bme.hu*

[2] *Budapest University of Technology and Economics, Faculty of Mechanical Engineering, Department of Materials Science and Engineering. Budapest, Hungary, varbai.balazs@gpk.bme.hu*

Abstract

Corrosion caused by iron contamination, also known as rouging, is a possible type of corrosion of stainless steels. This type of corrosion is often confused with the corrosion of stainless steel itself. Rusty discoloration on the surface of a material considered corrosion resistant is a problem in the construction and pharmaceutical industries. Repairing rouging afterwards is usually costly, but can be prevented by good manufacturing practices and control.

In our research, we compared four commonly used stainless material grades with different surface treatments. We investigated the effect of scratches left by carbon steel on the surface of the samples and the time course of the process.

Keywords: *corrosion, rouging, stainless steel.*

1. Introduction

Stainless steel is defined as a ferrous alloy containing at least 10.5% chromium but not more than 1.2% carbon. Stainless steels can be classified into four groups according to their microstructure: ferritic, austenitic, martensitic and duplex (austenitic-ferritic) steels. They have excellent corrosion resistance due to the passive oxide layer formed by chromium. For a stainless steel to exhibit adequate corrosion resistance in a given medium, its surface must be clean and free from organic and metallic impurities. Corrosion is defined in ISO 8044:2003 (withdrawn, but last edition in Hungarian) as: „The physico-chemical interaction between a metal and its environment, resulting in a change in the properties of the metal and often in a deterioration of the functional characteristics of the metal, the environment or the technical system comprising them”[1]. Of particular importance is the corrosion caused by iron contamination (rouging), which usually occurs through contact with carbon steels. The most frequent causes are the use of inadequately cleaned auxiliary equipment and normal carbon steel tools; the cutting of raw material; production and assembly in production lines using mixed (normal carbon steel and stainless) steels. Corrosion caused by iron contamination can be simply a slight brownish (rusty) discolouration or even surface pitting corrosion [2–5]. Our experiments investigated the resistance of austenitic and duplex grades to rouging.

2. Test materials

The materials used for the experiments, their surface finishes, and the values of the pitting resistance equivalent numbers (PREN) are given in

Table 1. *Test materials, their surface finish and pitting corrosion resistance*

Grade	Surface finish	PREN
304	polished	18
316L	pickled, 2E	23
2205	brushed, 2E/2D	31
2304	pickled, 2E/2E	26

Table 1. 304 and 316L are two standard, widely used austenitic stainless steels with polished and pickled surface finishes. 2205 and 2304 are duplex stainless steels with brushed and pickled surface finishes.

The test specimens were „contaminated" with iron particles in two different ways before the test. As shown in **Figure 1,** one specimen was wire-brushed and the other was scratched with a sharpened piece of carbon steel.

In the case of the wire brush, the scratches are shallower but more numerous on the sample surface, and iron oxide from the wire brush was also deposited on the sample surface. In the case of scratching with the carbon steel piece, the scratches are deeper and fewer in number.

After scratching, the samples were stored under laboratory conditions in an atmosphere containing hydrochloric acid vapour to accelerate the corrosion process. Macro- and microscopic images of the samples were taken after two weeks and two months, respectively.

3. Results and discussion

3.1. Corrosion test results of the 304 grade specimen

The surface of the 304 grade, polished surface-finished specimen shows significant changes after only two weeks. The scratched specimen shows dense surface pitting corrosion, while the wire-brushed specimen shows rusty discolouration and scattered surface pitting corrosion (**Figure 2**).

The same sample examined after two months is shown in **Figure 3**.

A small area on the edge of the sample was masked before wire brushing, in order to have a reference for comparison with the iron contaminated material.

The masking was removed after the wire brushing was completed.

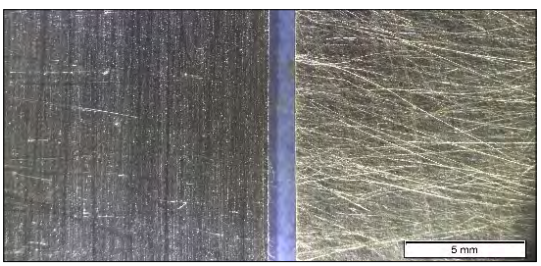

Figure 1. *Scratched (left) and wire-brushed surfaces, 2205 duplex, scale is 5 mm.*

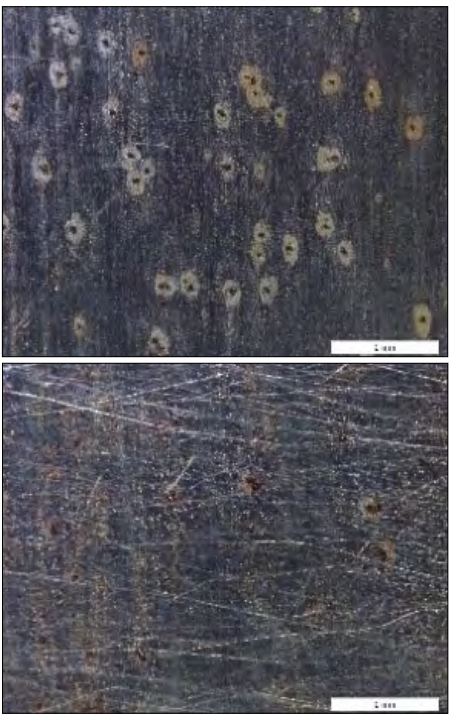

Figure 2. *Scratched (upper) and wire-brushed 304 test specimens after two weeks, scale is 2 mm.*

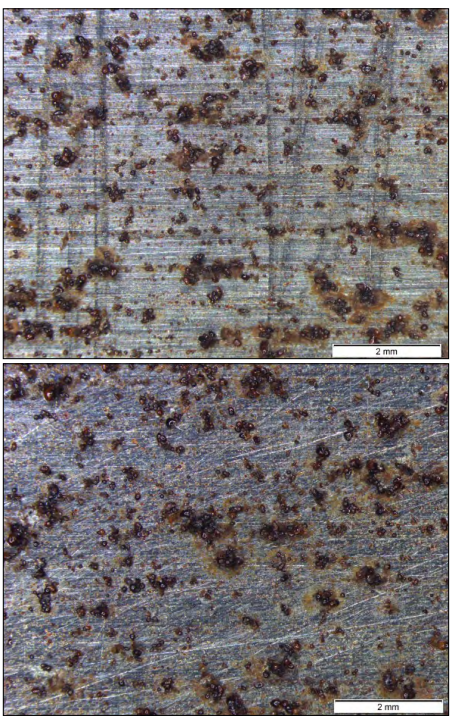

Figure 3. *Scratched (upper) and wire-brushed 304 test specimens after two months, scale is 2 mm.*

It can be clearly seen in Figures 4 and 5, that no discolouration or surface pitting has occurred on the masked surface. This phenomenon was observed in all test cases for each material grade tested.

3.2. Corrosion test results of the 316L grade specimen

On the pickled surface of the 316L sample, after two weeks, only scattered rust discolouration is visible (Figure 6).

However, after two months, large amounts of rust deposits and surface pitting were observed on the sample surface (Figure 7).

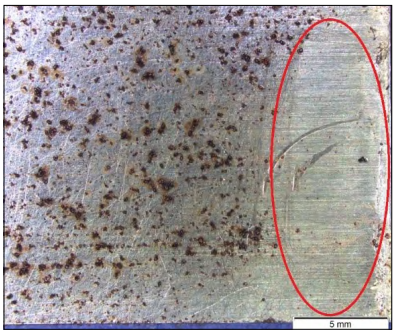

Figure 4. *The masked surface of the 304 specimen, after two months of exposure.*

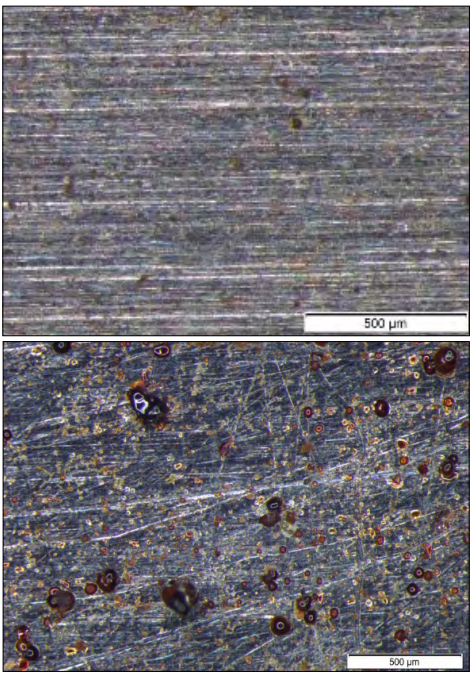

Figure 5. *The masked (upper) and iron-contaminated surface of the 304 specimen after two months, the scale is 500 µm.*

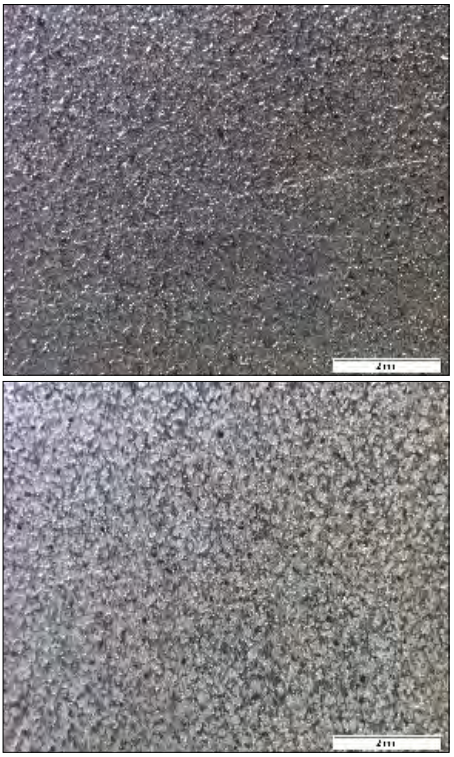

Figure 6. *Scratched (left) and wire-brushed 316L test specimens after two weeks, the scale is 2 mm.*

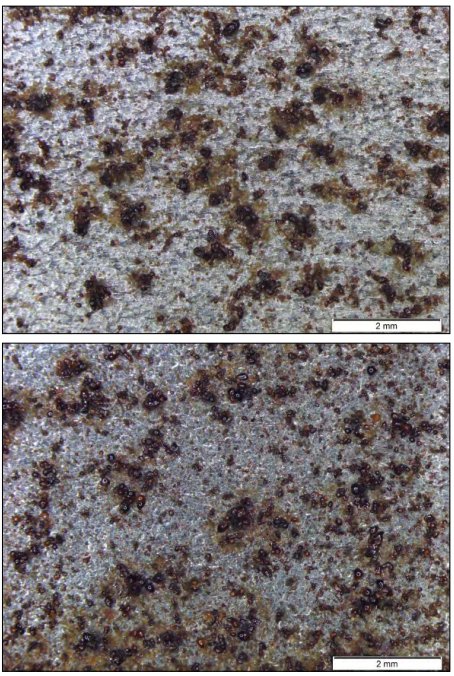

Figure 7. *Scratched (uooer) and wire-brushed 316L test specimens after two weeks, the scale is 2 mm.*

3.3. Corrosion test results of the 2205 grade specimen

he surface finish of the 2205 duplex sample is brushed. In contrast to the other samples, the surface of this material shows a rusty discolouration only in the scratches (**Figures 8–9**).

Of the four material grades tested, this material has the highest pitting resistance index (PREN), as a result, there was no surface pitting corrosion observed in the sample, even at high magnifications.

3.4. Corrosion test results of the 2304 grade specimen

On the pickled surface of the 2304 duplex specimen, a rusty discolouration is visible in patches on the scratched specimen, and a more or less uniform rusty discolouration is visible on the wire brushed specimen (**Figures 10–11. ábra**).

4. Conclusions

The rust that forms on the surface of the specimens is loose and can be easily wiped off the sur-

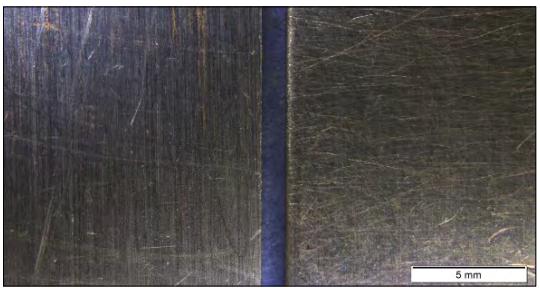

Figure 8. *Scratched (left) and wire-brushed 2205 specimens after two weeks, scale is 5 mm.*

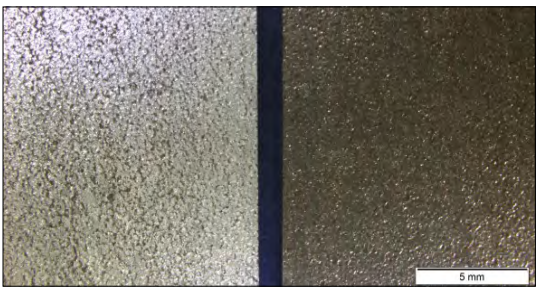

Figure 10. *Scratched (left) and wire-brushed 2304 specimens after two weeks, scale is 5 mm.*

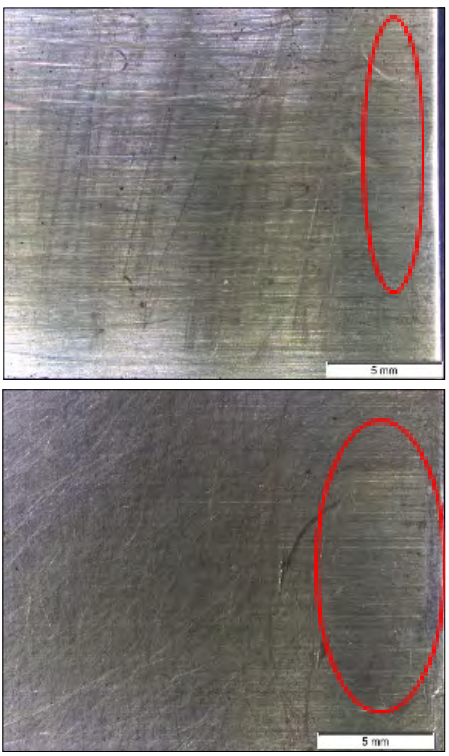

Figure 9. *Scratched (upper) and wire-brushed 2205 specimens after two months, scale is 5 mm.*

Figure 11. *Scratched (upper) and wire-brushed 2304 specimens after two months, scale is 5 mm.*

Figure 12. *The 1.4404 specimen surface after two months.*

face of the specimen, which will roll off with little force (**Figure 12**). The difficulty of repair is due to pitting corrosion of the surface.

It can be observed that the amount of rust deposited on the surface of the sample increases with time, and with it the number and depth of pits on the surface.

Acknowledgements

The publication was funded by the European Union through the ERASMUS+ Strategic Partnership Key Action 2, 2021-1-RO01-KA220-HED-000032181, ALLIES, with the support of the National Talent Programme of the Ministry of Innovation and Technology, NTP-SZKOLL-22-0080, and the National Research, Development and Innovation Office - NKFIH, (OTKA PD 138729).

References

[1] MSZ EN ISO 8044:2003 *Fémek és ötvözetek korróziója. Alapvető szakkifejezések és fogalommeghatározások (ISO 8044:1999)*. 2003.

[2] Crookes R.: *Rozsdamentes acélok pácolása és passziválása.* 2. ed., Anyagok és alkalmazások serie, vol. 4., Euro Inox, Brussels, 2010.

[3] Maller R. R.: *Passivation of stainless steel*. Trends in Food Science & Technology, 9/1. (1998).

[4] Corbett R. A.: *Rouging – A Discoloration of Stainless Steel Surfaces*. Materials Selection & Design, 2001. 64–66.

[5] Hornus E. C. et al.: *The Influence of Surface Iron Contamination on the Localized Corrosion Resistance of Austenitic and Duplex Stainless Steel, Studied with a Novel Rust Deposition Method*. Corrosion, 78/6. (2022). https://doi.org/10.5006/4067

sciendo

Acta Materialia Transylvanica 6/1. (2023) 14–22.
DOI: Hungarian: https://doi.org/10.33923/amt-2023-01-03
English: https://doi.org/10.33924/amt-2023-01-03

ACTA MATERIALIA TRANSYLVANICA

Effect of Production Parameters on Impact Energy of Ti-6Al-4V samples Produced by Additive Manufacturing

Dezső Gergely,[1] Szigeti Ferenc

[1] *University of Nyíregyháza, Institute of Engineering and Agriculture, Department of Physics and Production Engineering, Nyíregyháza, Hungary, dezso.gergely@nye.hu*

Abstract

Powder bed melting is an important additive manufacturing process. The process variants are gaining more and more space in the industry: especially in the industry that produces products made of special alloys with additive manufacturing. Selective laser melting is one variant of powder bed fusion processes. In this paper experimental study on impact energy of test specimens made from Ti-6Al-4V alloy, manufactured by selective laser melting is presented. Parameter setup of experiments are defined by design of experiment method, and an empirical formula is fitted to measured data. It is pointed out that impact energy is highly sensitive to manufacturing parameters studied here, and strong interactions are also observed. A formula is derived for costrained optimization on isoenergetic surfaces. Results can be applied for control of an important material property, impact strength of parts manufactured by selective laser melting.

Keywords*: powder bed fusion, selective laser melting, impact energy, scan speed, layer thickness.*

1. Introduction

As a result of a revolution of scientific research and development started in the middle of 20th century and continuing also nowadays, additive manufacturing (AM) finds more and more place in practical applications and industry.

It may play many different role in the process of design, production and maintenance including prototyping, casting pattern and core making, manufacturing tools, jigs or fixtures (especially with complex shape), producing blanks, fabricating end-use parts, repairing of parts. It is remarkable that powder bed fusion technologies are recently applicable in the first five of the mentioned areas. According to predictions, three quarters of furnishing and equipment parts and half of engine parts are expected to be manufactured by AM technologies in the aircraft industry until 2050 [1]. Application of AM in medical industry can be classified into five fields: medical models, surgical implants, surgical guides, external aids and bio-manufacturing. The number of scientific publications on medical applications of AM show an exponential increase in last 15 years [2, 3]. AM technologies nowadays are applied mainly on high added value segments of industry in relatively small, but increasing quantity. Today AM is still an intensive field of research, industrial activity and business. Whilst several hundred AM technologies have been developed till now indicating creativity of experts and promising development potential of the area, there are some challenges to solve before AM turns into a widely spread and cost effective manufacturing technology. Development in several disciplines is needed for stronger utilization of this technology, such as education and knowledge management, more powerful softwares supporting design for AM, overcoming limits of bed size and speed of manufacturing, new ideas and procedures in quality management since features of products are highly dependent on manufacturing parameters and accidental fluctuations associated with them [4].

Quality management of additively manufactured products is an intensive area of research and development. While AM generally has the great advantage of manufacturing products directly from CAD models with almost arbitrarily complex geometry, it has some challenges in the field of quality and process repeatability [5, 6].

In this paper, experimental research is introduced on parts manufactured by metal selective laser melting (SLM). This is a powder bed fusion additive manufacturing technology applying a highly intensive laser beam for totally melting the metal powder layer by layer.

The main materials used for metal SLM are steel and titanium alloys. Interest in titanium alloys rose sharply around 2010 as they proved to be biocompatible. With all metals, application of SLM for ceramic and composite materials is increasingly studied [7].

Ti6Al4V is one of most frequently used titanium alloys in industry. This results from its excellent properties such as good mass-strength ratio, high corrosion resistance, being non magnetic and its biocompatibility. This material is often applied in the vehicle industry, especially aircraft parts manufacturing, marine applications, in medicine for medical implants, in nuclear reactor technology, and many other fields. This material is available in the form of stock for conventional technologies producing wrought parts, and also for additive technologies as metal powder. In this study we are interested in parts made of Ti6Al4V by an additive manufacturing technology.

SLM is a widely applied technology for processing Ti6Al4V material. This is the technology which has the most industrial application mainly in aeronautical and biomedical areas, and attracts salient research attention because of its versatility. Besides the advantages of SLM it has three main challenges when it is applied to Ti6Al4V powder. Firstly, besides high material strength, manufactured parts have the feature of relatively low ductility. It correlates with high cooling rate during the SLM process, which results in martensitic material structure. Secondly, a challenge is the presence of microstructural defects such as balling and porosity greatly affecting fatigue resistance of parts. The third challenge is the presence of residual stresses in as-built parts derived from high temperature rates and gradients during the manufacturing process. All of the above challenging problems depend on a high number of parameters, since the entire SLM manufacturing process can be characterised by more than a hundred technical data However there are three parameters which play a special role in how material features develop in SLM: laser power, laser scanning speed and layer thickness. While these three challenging problems substantially impact how parts can be used in practice and industry, extensive research work is in progress currently on this area [8, 9]. Usually, post-processing is also required for achieving appropriate quality. For medical applications different post-processing treatments can be applied such as sandblasting, carborundum disc polishing or ultrasonication in isopropyl alcohol [10, 11].

Features of materials manufactured by SLM do not depend directly on a single process parameter, rather, on a combination of them. So when the aim is to investigate how those depend on manufacturing parameters, a multivariable study is necessary.

Impact energy is a material feature standing in strong relationship with ductility. In this paper we present our experimental research results on impact energy of Ti6Al4V specimens as a function of laser power, laser scanning speed and layer thickness.

2. Material and samples

2.1. Material

In our experiments samples were built from Ti6Al4V (TC4, Ti64) alloy material melted from EOS Titanium Ti64ELI powder. Chemical composition of this powder can be characterized as 5.5-6.75 wt% Al, 3.5-4.5 wt% V the balance is composed of Ti, and some elements like O, N, C, H and Fe are guaranted to be under a certain low limit. This is a Grade 25 titanium alloy, with reduced content of oxygen, nitrogen, carbon and iron, containing extra low interstitials (ELI), ensuring higher ductility and improved fatigue resistance related to Grade 5 Ti6Al4V materials. This is why it is suitable for medical implants and devices. The size of metal alloy powder particles varies in the range of 20-80 micrometers according to the data sheet [12].

2.2. Sample preparation

Test specimens were manufactured by an EOS M290/400W additive manufacturing machine, which implements selective laser melting of metal powders. Selective laser melting is a layer by layer additive manufacturing technology, which has two key steps: a coating of metallic powder is formed on a plate or tray, then a laser beam fuses the metal powder selectively in areas belonging to the part being fabricated. This is accomplished in a closed chamber filled with an inert atmosphere. The main parameters of this process are layer thickness, hatch distance, laser power and laser (scanning) speed, but there are several other parameters controlling properties of gas flow, la-

ser beam, scanning pattern, motion of actuators, thermal state of the chamber and others. Parameters usually vary depending on which region of the model is just built, that is internal (infill), bottom, top or some edge of it. Operating software of machines offer default parameter setup, and can also be changed by the user.

The shape of the samples was identitcal to a standard 10×10×55 mm Charpy impact test (or V-notch test) specimen (standard: MSZ EN ISO 148-1:2017 The specimens were manufactured in a laid position so that notches were on the top side.

Each test specimens was manufactured in the same orientation. This is highly important in the case of manufacturing technologies comprising special directions in space leading to anisotropy either in microstructure or material properties of the produced part. We performed a preliminary study with 5-5 test pieces for impact energy. We found that there was a 19.57% difference between mean values for specimens produced in standing and laid position. As expected, the smaller impact energy value belongs to the standing position, because in this case fractures grow along layers melted onto each other, that is layers separate from each other during the process of breaking. In the case of test parts manufactured in the laid position, when the notch is on the top side, layers have to split when the specimen breaks.

In our study the effect of production parameters on impact energy is investigated. Because there are a large number of manufacturing parameters, we selected three that are highly important: infill laser power (P), infill laser speed (u) and layer thickness (t). The main default values of them are summarized in **Table 1**.

It is important to emphasize that hatch distance (h), which is also an essential parameter, was kept constant in this study with a default value $h = 0.14$ mm.

Three levels of each of those were taken into account in our experiment plan. Levels are not equidistant, but are calculated proportionately with a multiplicative factor of 1.2. **Table 2** shows values of varied production parameters in experiments.

Energy input (e, [W/mm^3]) is a highly characteristic feature of a selective laser melting process. As seen from the unit, the production parameter commonly named “energy input” is a more precise specific power input, or indeed power density, and is the laser energy irradiated into 1 mm^3 volume of material in 1 second. It can be calculated from manufacturing parameters by the following formula:

$$e = \frac{P}{u \cdot 1s \cdot t \cdot h} \quad (1)$$

Here the meaning of proportionately selected levels can be understood, because in this way we have many different parameter sets with equal energy input (e) as **Tables 2** and **3** show, so we have an additional opportunity for evaluating experimental data taking into account this significant derived parameter. A full factorial experiment would consist of $3^3 = 27$ different parameter setup. This is a large number, so we decided to plan an orthogonal fractional factorial experiment with a 9 experimental parameter setup according to **Table 3**. This fractional factorial experiment plan is derived from Taguchi’s $L_9(3^4)$ orthogonal plan array by deleting fourth column **[13]**.

Table 1. *Names, notation and default values of four important parameters of the SLM process in the case of our additive manufacturing system*

Name of the parameter	Notation	Default value
laser power	P	280 W
laser scanning speed	u	1200 mm/s
layer thickness	t	0.03 mm

Table 2. *Levels of varied factors in experiments*

Factor	level -1	level 0	level 1
P (W)	233.33	280	336
u (mm/s)	1000	1200	1444
t (mm)	0.025	0.030	0.036

Table 3. *Parameter setup of partial factorial experiment plan, and energy input values belonging to those*

	Infill laser power [W]	Infill laser speed [mm/s]	Layer thickness [mm]	Energy input [W/mm^3]
A	233.33	1200	0.03	46.296
B	280	1000	0.03	66.667
C	336	1440	0.03	55.556
D	336	1200	0.025	80.000
E	233.33	1000	0.025	66.667
F	280	1440	0.025	55.556
G	280	1200	0.036	46.296
H	336	1000	0.036	66.667
I	233.33	1440	0.036	32.150

For comparison and control of results, samples were manufactured with an additional three parameter set, involving default parameter setup (*J*), as shown in **Table 4**. Five pieces of test specimens were produced for each parameter setup.

3. Results and evaluation

3.1. Experimental results

The Charpy impact test were performed according to standard MSZ EN ISO 148-1:2017. We applied Charpy impact test equipment PSW 15 with maximum impact energy 15 J and scale constant 0.1 J. There is a single exception; the sample series denoted as A, because the impact energy of that sample exceeded 15J. For this reason, in this case, we had to apply larger test equipment; the PSW 300. This is why the impact energy data in row A have only two siginificant figures. In this paper we use *K* as notation for impact energy. the unit of impact energy is the Joule (J) in this paper. Measurement results are summarized in **Table 5**.

Each experiment consisted of 5 measurements. This means that 5 test specimens manufactured with the same parameter setup were broken. Then, the mean value and standard deviation of impact energy were calculated. In our experiments standard deviations have relatively small values.

3.2. Evaluation of the measurement results

The impact energy is considered as a function of experimental factors. In our case:

$$K = K(P, u, t). \tag{2}$$

Our first goal was to find an empirical formula for this function. In our case an interpolation technique was appropriate, because we sought a formula, which adequately approximates measured impact energy values within the experimental parameter domain. Using a polynomial interpolation function is straightforward because of the nature of the phenomenon we study. Order of interpolation has to be determined so that we avoid overfitting. Now we have 12 measured data, it implies that the third order approximation was too high in order. Consequently we supposed a second order polynomial formula for interpolation as follows:

$$\begin{aligned} K(P,u,t) &= a_0 + a_1P + a_2u + a_3t + a_4P^2 \\ &+ a_5u^2 + a_6t^2 + a_7Pu + a_8Pt + a_9ut \end{aligned} \tag{3}$$

Table 4. *Three additional parameter setup for comparison*

	Infill laser power [W]	Infill laser speed [mm/s]	Layer thickness [mm]	Energy input [W/mm³]
J	280	1200	0.03	55.556
K	233.33	1000	0.03	55.555
L	280	1000	0.025	80.000

Table 5. *Summary of measurement results. Sample series codes (column 1), measurement results in J units (columns 2-6), mean values and standard deviations (columns 7 and 8 respectively).*

Sample code	1	2	3	4	5	Mean value	Standard deviation
A	18.0	18.0	16.0	16.0	16.0	16.8	1.10
B	15.0	13.7	14.6	11.9	13.9	13.8	1.19
C	10.2	10.3	10.7	10.2	11.4	10.6	0.51
D	8.4	8.2	10.1	8.9	8.3	8.8	0.79
E	11.0	9.8	8.6	9.5	10.2	9.8	0.88
F	12.7	10.0	11.3	10.8	11.6	11.3	1.00
G	12.8	14.2	12.6	13.0	14.3	13.4	0.81
H	11.3	11.7	11.3	11.1	10.6	11.2	0.40
I	11.3	10.2	10.2	11.7	12.2	11.1	0.90
J	11.4	9.6	10.4	12.1	11.7	11.0	1.02
K	11.2	10.3	10.6	11.3	9.8	10.6	0.63
L	10.3	9.1	9.0	8.6	8.9	9.2	0.65

Multiplicative parameters $a_0 \ldots a_9$ have derived dimensions so that, after evaluation of this formula unit of the result, let be J (Joule). For example

$$[a_0] = \mathrm{J}, \qquad [a_1] = \frac{\mathrm{J}}{\mathrm{W}} = \mathrm{s}$$

and so on. In the following we will not deal with and will not indicate dimensions of the $a_0 \ldots a_9$ iparameters, because we believe that writing out those would make formulas and tables unnecessarily unperspicuous.

We applied Scilab software for determining $a_0 \ldots a_9$ parameters in the function of *K*. These parameters were to ensure that difference between val-

ues of K and the measured data is as small as possible. In Scilab, the OPTIM function can be used for nonlinear optimization. It requires definition of the function to be optimized, its gradient as another vector function, and some parameters controlling the convergence of the algorithm. Our task is a general nonlinear optimization with a single, smooth objective function, without constraints. OPTIM uses L-BFGS method for optimization [14].

As result of nonlinear optimization we obtained the following function for K:

$$\begin{aligned} K(P,u,t) = & -70{,}745933 - 0{,}0008086\,P \\ & + 0{,}1064481\,u + 1329{,}3723\,t \\ & - 0{,}0001446\,P^2 - 0{,}0000315\,u^2 \\ & - 93{,}507847\,t^2 + 0{,}0000201\,Pu \\ & + 0{,}908954\,Pt - 1{,}1531936\,ut \end{aligned} \quad (4)$$

Values of the multiplicative parameters in this formula show how strongly a factor (*P, u, t*) and interaction of factors (*Pu, Pt, ut*) influence impact enegy (*K*). The larger the multiplicative parameter, the more sensitive the impact energy is for factor or the interaction it multiplies. So we can get a „compass" for control of impact energy of the material fused in our SLM machine. The empirical trivariate function defined by the formula (4) is demonstrated on Figure 1.

Only one thing obscures this picture. This is the significant difference in magnitude of factors *P, u* and *t*. Scanning speed in mm/s units is 5 orders of magnitude larger than layer thickness in mm units. This implies that a small change in *u* creates a great shift in *K*, but a small change in *t* results in far smaller effect if those have the same multiplicative factor. In other words multiplicative parameters are not comparable if the factors they multiply are not in the same order of magnitude.

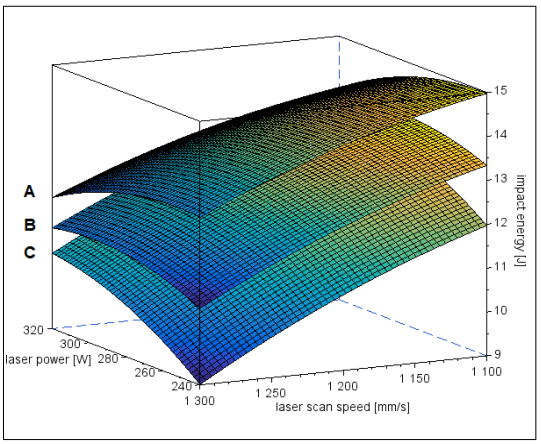

Figure 1. *Graph of empirical formula (4). Three different surfaces belong to different layer thickness values: A: t=0.036 mm, B: t=0.03 mm, C: t=0,025 mm.*

Nondimensionalization is a common means for transforming physical quantities into a form in which they become more comparable. It is worth substituting the *P, u* and *t* factors with a dimensionless variable and at the same time rescale multiplicative parameters. Let us introduce the following dimensionless variables:

$$x_P = \frac{P}{280\ W}, x_u = \frac{u}{1200\ m/s}, x_t = \frac{t}{0.03\ mm}. \quad (5)$$

We can say that we normalize variables to their default values. Nondimensionalized variables have dimensionless value 1 if *P, u* and *t* have the default value. For example $x_P = 1$ if $P = 280$W, and $x_P = 1{,}2$ if $P = 336$W. This means that in our experiments values of all the three process parameters correspond to one of the values 0.8, 1 or 1.2 of dimensionless parameters. Multiplicative prameters $a_0 \ldots a_9$ are rescaled as:

$$\begin{aligned} & b_0 = a_0,\ b_1 = a_1 \cdot 280\ W, b_2 = a_2 \cdot 1200 \frac{m}{s}, \\ & b_3 = a_3 \cdot 0{,}03\ mm, \qquad b_4 = a_4 \cdot (280\ W)^2, \\ & \qquad \ldots, \\ & b_7 = a_7 \cdot 280\ W \cdot 0{,}03\ mm \\ & b_8 = a_8 \cdot 1200 \frac{m}{s} \cdot\ 0{,}03\ mm. \end{aligned} \quad (6)$$

All of the new parameters $b_0 \ldots b_9$ have the same unit as *K*, that is the Joule. After nondimensionalization we have the following interpolation formula:

$$\begin{aligned} & K(P,u,t) \\ & \quad = -70{,}745933 - 0{,}226397\,x_P \\ & \quad + 127.73777\,x_u + 39.881168\,x_t \\ & \quad - 11.340299\,{x_P}^2 - 45.311942\,{x_u}^2 \\ & \quad - 0.0841571\,{x_t}^2 + 6.7491589\,x_P x_u \\ & \quad + 7.6352133\,x_P x_t - 41.51497\,x_u x_t \end{aligned} \quad (7)$$

In the formula (7) the coefficients are comparable. In first order terms the coefficients of laser scan speed and layer thickness are 100 times larger than those of laser power. In pure second order, member layer thickness has two magnitudes smaller weight than the other two. In interaction terms $x_u x_t$ has the largest coefficient, but $x_P x_u$ and $x_P x_t$ also have notable weight. From this overview we can conclude that each of three manufacturing parameters *P, u* and *t* has an effect on impact energy, none of them is negligible, but they stand in different mathematical relation with it.

3.3. Constrained optimization of the impact energy along an izoenergetic surface

Energy input, in other words power density, is an important feature of selective laser melting (SLM) technology. Several phenomena are strongly dependent on it, like thermal gradients during the manufacturing process, thermal stresses and deformations, and some accompaniment as balling and splatter. However it is not straightforward that there is direct relationship between energy input and a phenomenon or feature. When SLM technology is optimized, many times, multiple conditions are to be fulfilled, or at least minimized or maximized. In such a situation a constrained task may arise: to change the manufacturing parameter keeping energy input constant so that a special feature of the manufactured part, (such as impact energy), changes.

Our experimental parameter setup was developed so that many of those can be featured with same power density (energy input, e) value. We use this for investigating how impact energy depends on laser power density during the manufacturing process. According to **Tables 3** and **4** we can identify which experimental setups have identical energy input. This is summarized in **Table 6**.

In field of our three varied manufacturing parameter (laser power, laser scan speed and layer thickness) Formula (1) defines a surface for each value of energy. Such surfaces are called isoenergetic surfaces. The equation of these surfaces can be derived by rearrangement:

$$t = \frac{P}{u \cdot 1s \cdot e \cdot h} \tag{8}$$

Figure 2 shows izoenergetic surfaces belonging to values in first column of **Table 6.** Each experimental setup corresponds a point on some of these surfaces.

Now we derive from equations (4) and (6) a formula for impact energy along an isoenergetic surface. We eliminate layer thickness (t) from (4) by substituting (8):

$$\begin{aligned} K(P,u,e=constant) &= -70{,}745933 - 0.0008086\,P \\ &+ 0{,}1064481\,u + 1329{,}3723\,\frac{P}{u \cdot 1s \cdot e \cdot h} \\ &- 0{,}0001446\,P^2 - 0{,}0000315\,u^2 \\ &- 93{,}507847\left(\frac{P}{u \cdot 1s \cdot e \cdot h}\right)^2 + 0{,}0000201\,Pu \\ &+ 0{,}908954\,\frac{P^2}{u \cdot 1s \cdot e \cdot h} \\ &- 1{,}1531936\,\frac{P}{1s \cdot e \cdot h} \end{aligned} \tag{9}$$

As mentioned earlier, in our investigation, hatch distance h is also constant. This is a bivariate function of laser power (P) and laser scan speed (u). Here we note that at the place of formula (8) another variable could also be expressed, and eliminated, so impact energy along an isoenerget-

Table 6. *Experimental setups with same energy input*

Energy input, e, (W/mm³)	Codes	Number of them
32.150	I	1
46.296	A, G	2
55.556	C, F, J, K	4
66.667	B, E, H	3
80.000	D, L	2

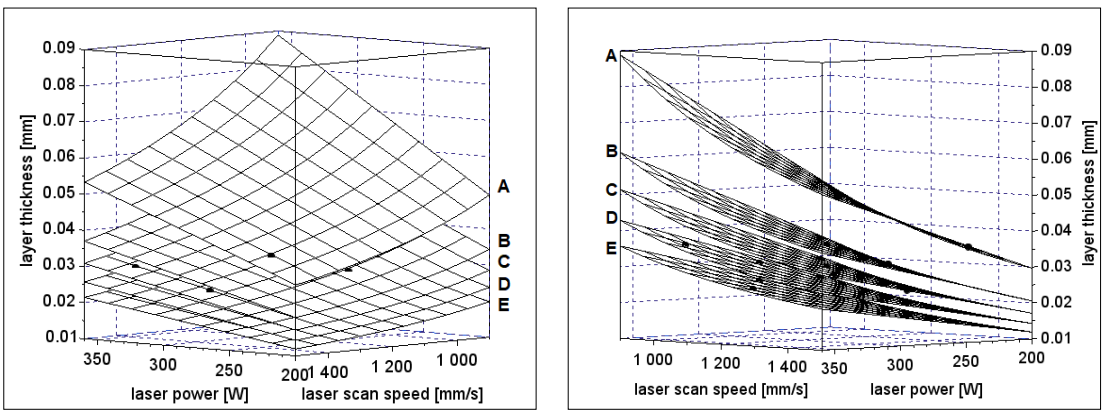

Figure 2. *Isoenergetic surfaces in the space of three manufacturing parameter varied in our experiments. A: 32.150 W/mm³, B: 46.296 W/mm³, C: 55.556 W/mm³, D: 66.667 W/mm³, E: 80.000 W/mm³, black dots indicate experimental setups, each dot belongs to one of the isoenergetic surfaces, both parts of the figure show the same diagram from different views.*

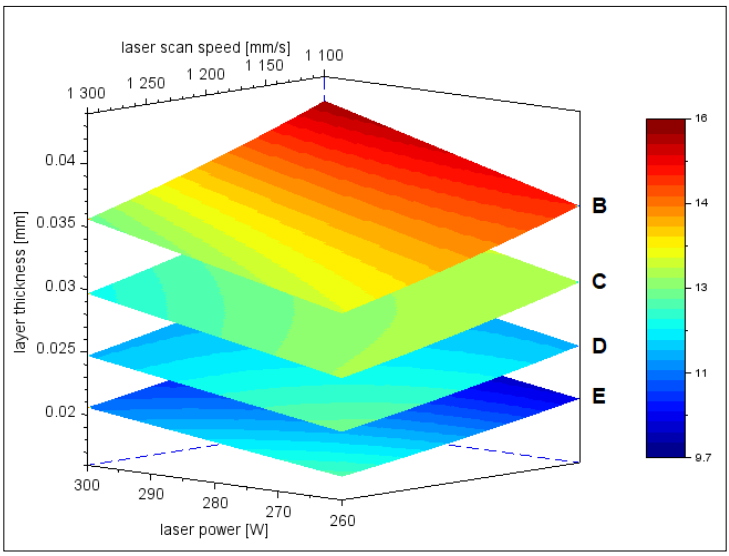

Figure 3. *Impact energies computed from formula (4) on isoenergetic surfaces in the space of three manufacturing parameters varied in our experiments. Isoenergetic surfaces belong to power densities: B: 46.296 W/mm³, C: 55.556 W/mm³, D: 66.667 W/mm³, E: 80.000 W/mm³. Impact energy in [J] units is visualized by colors, the legend shows the color codes.*

ic surface can be expressed as a function of P and t, or t and u. We continue with formula (9).

Figure 3 shows impact energy as a function of laser power and laser scan speed along isoenergetic surfaces belonging power density values involved in first column of **Table 6.**

The isoenergetic surface belonging to 32.150 W/mm³ was omitted because we have only one experimental point on it, and possibly that has the highest interpolation error.

It can be observed that the power density itself does not bear a direct relation with impact energy. This means that power density can not be applied as a control quantity when the ductility or the brittleness of a part has to be ifluenced. Indeed, the special parameter triplet of laser power, laser scan speed and layer thickness have to be used.

However it is possible to describe the impact energy as a function of three important manufacturing parameters, and give an expression of it along isoenergetic surfaces.

4. Discussion

It can be observed that the experimental factors laser power, laser scanning speed and layer thickness influence significantly the impact energy of the specimen, and impact energy of specimens manufactured with default values (denoted with J in **Table 4**) is placed near the middle of the range of measured values.

Impact energy of samples with code A is salient. We repeated the experiment, and got the same result. This indicates that there is a substantial change in internal structure of the material as the triplet of studied process parameters approaches towards parameter setup A. It seems to be worthy of a deeper study.

The empirical formula gained by interpolation on experimental data must be handled with care, because this can give acceptable approximation within the small part of the domain around the center point of parameter variation. Our results may be extended by a future experimental work with a larger number of experimental setups. In the case of a larger number of measurements, order of interpolation can also be increased without overfitting. A full third order interpolation in case of three variables needs at least 20 measurement points, possibly more.

Formula (4) shows that impact energy is far from a linear function of laser power, laser scan speed and layer thickness even within a small parameter window. Pure second order and interaction terms also have significant coefficients.

The complex nature of SLM (and generally additive manufacturing) technology can be presumed behind non-linear behaviour. The impact energy is substantially influenced by material porosity,

metallographic microstructure, surface quality and residual stress state. All of these features depend on manufacturing parameters.

5. Conclusions

The impact energy of samples manufactured by selective laser melting (SLM) was measured by V-notch impact test. Test specimens were manufactured with different process parameters. Three manufacturing parameters, the laser power, the laser scanning speed and the layer thickness were varied, while the hatch distance and other parameters were kept constant. Experimental parameter setups were constructed by fractional factorial design of the experiment.

The measurement results show significant difference. Least mean value is 8.8 J, while highest mean value is 16.8 J, which is more than double the previous. This indicates that the impact energy is a material property, which is highly sensitive for manufacturing parameters investigated in this study.

A quantitative trivariate empirical formula was fitted onto experimental data by interpolation procedure. This is a second order polinomial formula. It can be observed that pure second order and interaction terms have notable coefficiency, which means that impact energy is a strongly nonlinear function of production parameters.

A formula was derived for calculating impact energy along isoenergetic surfaces. Here isoenergetic means that parameter triplets represented by points of the surface are associated with the same energy input (power density).

While the impact energy is a highly important material feature, this empirical formula may be a useful tool to pre-indicate or optimize it as a function of SLM process parameters.

Acknowledgements

This work was supported by the application project GINOP-2.2.1-15-2017-00055 entitled „Research on osteosynthesis of implants and development of trabecular structures by application of additive manufacturing" cofunded by European Union and Hungarian Government.

Authors express thanks to Biomechanical Laboratory at University of Debrecen for manufacturing test specimens, and Material Test Laboratory at University of Nyíregyháza for measurements in the frame of project mentioned above.

This project was supported by the Scientific Council of the University of Nyíregyháza.

References

[1] Gisario A., Kazarian M., Martina F., Mehrpouya M.: *Metal Additive Manufacturing in the Commercial Aviation Industry: A Review.* Journal of Manufacturing Systems, 53. (2019) 124–149. https://doi.org/ 10.1016/j.jmsy.2019.08.005.

[2] Javaid M., Haleem A.: *Additive manufacturing applications in medical cases: A literature based review*. Alexandria Journal of Medicine, 54/4. (2018) 411–422. https://doi.org/10.1016/j.ajme.2017.09.003

[3] Esmaeilian B., Behdad S., Wang B.: *The evolution and future of manufacturing: A review*. Journal of Manufacturing Systems, 39. (2016) 79–100. https://doi.org/10.1016/j.jmsy.2019.08.005

[4] Thomas-Seale L. E. J., Kirkman-Brown J. C., Attallah M. M., Espino D. M., Shepherd D. E. T.: *The barriers to the progression of additive manufacture: Perspectives from UK industry*. International Journal of Production Economics, 198. (2018) 104–118. https://doi.org/10.1016/j.ijpe.2018.02.003

[5] Dezső G., Kósa P.: *Dimensional and shape accuracy of cylindrical and paralellepiped-like parts made by selective laser melting technology*. Annals of Faculty of Engineering Hunedoara, International Journal of Engineering, 18/1. (2020) 39–45.

[6] Buican G. R., Oancea G., Lancea C., Pop M. A.: *Influence of Layer Thickness on Internal Structure of Parts Manufactured from 316-L Steel Using SLM Technology*. Applied Mechanics and Materials, 809–810. (2015) 369–374. https://doi.org/10.4028/www.scientific.net/AMM.809-810.369.

[7] Yang H. et al.: *Six-Sigma Quality Management of Additive Manufacturing*. Proceedings of the IEEE, 109/4. (2021) 347–376. https://doi.org/10.1109/JPROC.2020.3034519

[8] Yap C. Y. et al.: *Review of selective laser melting: Materials and applications*. Applied Physics Reviews, 2/4. (2015) 041101. https://doi.org/10.1063/1.4935926

[9] Shipley H. et al.: *Optimisation of process parameters to address fundamental challenges during selective laser melting of Ti-6Al-4V: A review*. International Journal of Machine Tools and Manufacture, 128. (2018) 1–20. https://doi.org/10.1063/1.4935926

[10] Pacurar R., Balc N., Prem F.: *Research on how to improve the accuracy of the SLM metallic parts*. AIP Conference Proceedings, 1353/1. (2011) 1385–1390. https://doi.org/10.1063/1.3589710

[11] Cosma C., Balc N., Moldovan M., Morovic L., Gogola P., Borzan C.: *Post-processing of customized implants made by laser beam melting from pure Titanium*. Journal of Optoelectronics and Advanced Materials, 19/11–12. (2017) 738–747.

[12] Material data sheet: EOS Titanium Ti64ELI. EOS GmbH - Electro Optical Systems, 2014. https://www.sculpteo.com/media/imagecontent/EOS-Titanium-Ti64ELI.pdf (accessed on 25 May 2021)

[13] Aoki S., Takemura A.: *Design and Analysis of Fractional Factorial Experiments From the Viewpoint of Computational Algebraic Statistics*. Journal of Statistical Theory and Practice, 6/1. (2012) 147–161. https://doi.org/10.1080/15598608.2012.647556

[14] Baudin M., Couvert V., Steer S.: *Documentation of Scilab function OPTIM*. The Scilab Consortium – Digiteo / INRIA, 2010. https://www.scilab.org/sites/default/files/optimization_in_scilab.pdf (accessed on 25 May 2021)

sciendo

Acta Materialia Transylvanica 6/1. (2023) 23–28.
DOI: Hungarian: https://doi.org/10.33923/amt-2023-01-04
English: https://doi.org/10.33924/amt-2023-01-04

ACTA MATERIALIA TRANSYLVANICA

Investigation of the Machinability of GTD-111 Type Nickel-Base Superalloy During Face Milling

Gábor KÓNYA,[1] Norbert SZABÓ, Zsolt Ferenc KOVÁCS

John von Neumann University, GAMF Faculty Engineering and Computer Science, Dep. of Innovative Vehicles and Materials, Manufacturing Technology Research Group. Kecskemét, Hungary.
[1] konya.gabor@gamf.uni-neumann.hu

Abstract

In this paper, the authors investigate the effect of technological parameters on the face milling of GTD-111 type nickel-base superalloys. These alloys are among the most difficult to machine and are widely used as a base material for gas turbine components in the aerospace and energy industries. The aim of this paper is to determine, using the Taguchi method, those parameters that have the greatest influence on cutting force and tool wear. A rotary force meter was used to measure the cutting force and cutting torque, and then the inserts used were examined used under a microscope. Results show that feed per tooth has the greatest effect on cutting forces and tool wear. In order to avoid the formation of edge deposits, it is advisable to use higher cutting speeds and compressed air cooling.

Keywords: *nickel-base superalloy, face milling, cutting force, cutting torque, tool wear, ceramic tool .*

1. Introduction

The literature identifies four types of superalloys: nickel, cobalt, iron and titanium base superalloys [1]. Of these, nickel-base superalloys are mainly used in gas turbines for the aerospace and energy industries because these alloys retain their favourable mechanical and physical properties at high temperatures [2, 3]. These alloys are mainly used in the high temperature zones of gas turbines (HPC – High Pressure Compressor and HPT – High Pressure Turbine) (Figure 1), where operating temperatures reach 1400-1500 °C, operating pressures 40 bar in extremely corrosive environment, and operating speeds exceeding 10 000 rpm [4]. This extremely high temperature is necessary to increase the efficiency of gas turbines because, as with other thermal power engines, efficiency can be increased by increasing the difference between the maximum and minimum temperature of the working medium, which is why today's gas turbines have an efficiency of almost 60% [5].

The superalloys have high thermal strength, poor thermal conductivity, heat and corrosion resistance, but the parts made from them are often produced by cutting, despite the fact that

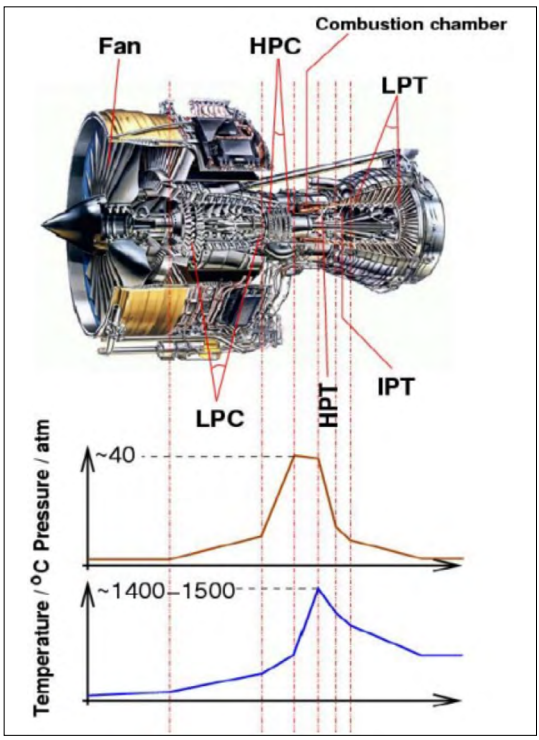

Figure 1. *Gas turbine showing the different zones with temperature and pressure conditions* [8]

their properties make them particularly difficult to machine [6]. In the present paper, the machinability of GTD-111 type Nickel-based superalloy was investigated during face milling, which has a significantly poorer machinability than Inconel 718, which is commonly investigated in today's research. Table 1 shows a comparison of the mechanical and physical properties of GTD-111, Inconel 718 and the widely known C45, presented as a reference material. Because of these properties, machinability of GTD-111 is significantly more difficult than machinability of Inconel 718, which has been generally tested in research, and compared to C45, GTD-111 has more than twice the tensile strength and only a quarter of the thermal conductivity.

Figure 2 shows the graph of the specific strength against temperature for commonly used metals. From the figure, it can be seen that nickel-based superalloys exhibit a high specific strength over a wide range of temperatures [7]. It illustrates very well why the machinability of these materials is so difficult and why so many researchers are working on this problem. Due to poor thermal conductivity, the large amount of heat generated during machining cannot escape into the chips and workpiece, and will therefore be concentrated at the edge of the bit. As a result, tools wear quickly and breakages are frequent.

Machining time is very important in manufacturing technology, where there is an increasing demand for cost-effective and environmentally friendly machining methods. This trend is reflected in the spread of high speed cutting (HSC) and hard cutting (HC). Due to the material properties of Nickel-based super alloys, and also due to the technology, high speed steels and brazed insert tools are not suitable to meet the demand, so carbide, ceramic, CBN (Cubic Boron Nitride) and diamond tool materials have emerged in this area.

In most cases, machining of Ni alloys by carbide cutting tools without coatings or with various coatings is carried out due to economic and technological constraints. This is particularly evident in the case of slot and other closed shape milling, for which the ceramic tools needed to machining them have only recently become available on the market and are also very expensive. Indexable end mills are more widely used for machining flat surfaces.

The use of ceramic cutting tools is justified because of their favourable properties, such as high hot hardness, good wear resistance, low thermal conductivity and excellent chemical stability [12]. These properties make them a good choice for machining super alloys, as they can be used at the temperature at which these super alloys are already annealing, thus the cutting forces reduces and so the low flexural strength of ceramic cutting tools is not problem.

In this paper, the authors investigate the effects of the cutting parameters used in the slot milling of GTD-111 type Nickel-based superalloy on the cutting forces and inserts failures. The aim is to find the parameter combination that results in the lowest tool load and tool wear.

Table 1. *The mechanical and physical properties comparison of the GTD-111, the Inconel 718 and the C45 steel* [9, 10]

	GTD-111	Inconel 718	C45
Tensile strength R_m (MPa)	1310	965	610
Hardness (HRC)	41.4	36	
Hardness (HB)			230
Elongation A_5 (%)	8	12	16
Density ρ (kg/m^3)	8000	8240	7700
Thermal conductivity λ (W/(m·K))	12.56	11.2	45.35

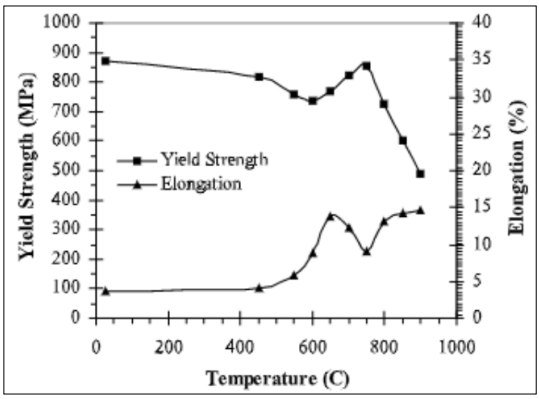

Figure 2. *Temperature dependence of yield strength and elongation of GTD-111.* [11]

2. Methodology of the experiment

This chapter describes the machining centre, measuring equipment, cutting tools and the methodology of the design of experimental (DoE).

2.1. Experimental setup

Because hard milling causes extreme demands on the machining centre, a robust and rigid one is required, therefore, the NCT EmL-850D machining centre was chosen. A Kistler 9125A24 type of rotary force meter was used to measure the cutting forces and torques, while a KISTLER 5697 type of signal processing unit was used for signal processing. The results were recorded using DynoWare software and evaluated using OriginPro 2021 software. The experimental setup is shown in **Figure 3**.

In the rotary force meter, the tool can be clamped with a collet chuck, but the face mill requires cylindrical mandrel chuck, so a special intermediate piece was manufactured. The drawing is show in **Figure 4**.

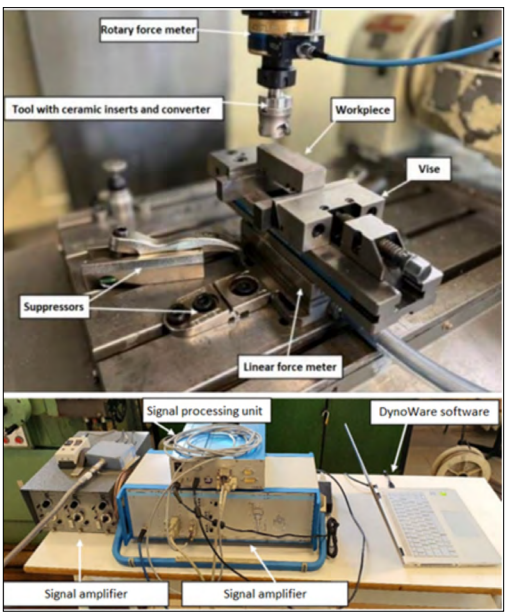

Figure 3. *Experimental setup.*

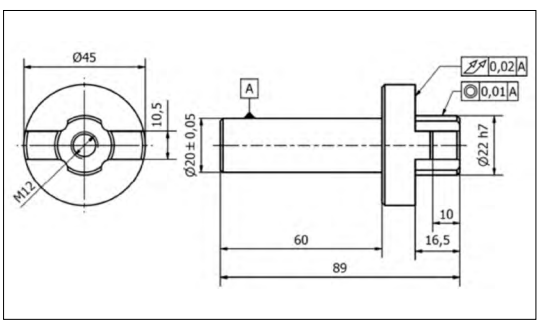

Figure 4. *Drawing of the intermediate piece required to clamp the tool.*

2.2. Tool used for the experiment

A TaeguTec BNGX 0904 CH-E04 ceramic insert and a TaeguTec TFMBN 350-22R09CH Ø40 mm face mill was used for the experiment (**Figure 5**).

2.3. Technological parameters used for the experiment

The experiments were performed according to the Taguchi experimental design, Minitab17® software was used to create the experimental design. The defined factors and levels are shown in **Table 2**, and the experimental design shown in **Table 3.** The choice of the technological parameters used was based on the manufacturer's recommendation.

During the experiments, down-milling was used, because when machining with ceramic tools, especially in difficult-to-cut materials, climb milling is harmful, as the tooth tries to cut the maximum chip thickness, which results in impact stress on the tool, which will break down faster due its low bending strength. In the case of down milling, the cut starts with zero chip thickness, essentially the tool is slightly milling into the material, resulting in a higher cutting zone temperature.

Table 2. *Milling factors and levels defined in the experimental design*

Milling factors		Levels		
		1.	2.	3.
A	Cutting speed v_c (m/min)	600	900	1200
B	Feed per tooth f_z (mm/tooth)	0.15	0.25	0.35
C	Depth of cut a_p (mm)	0.5	0.75	1

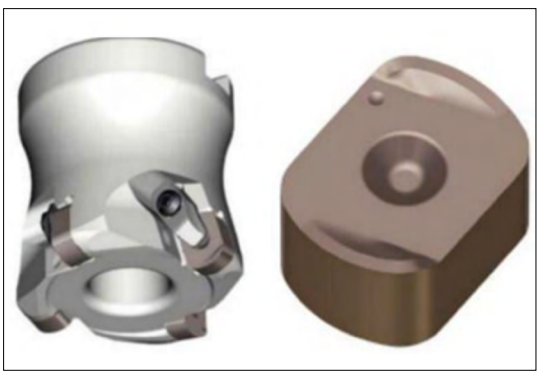

Figure 5. *The cutting tool holder and insert used for the experiment.*

Table 3. *The experimental design*

No. of experiment	a_p (mm)	f_z (mm/fog)	v_c (m/min)
1.	0.5	0.15	600
2.	0.5	0.25	900
3.	0.5	0.35	1200
4.	0.75	0.15	600
5.	0.75	0.25	900
6.	0.75	0.35	1200
7.	1	0.15	600
8.	1	0.25	900
9.	1	0.35	1200

The chip removal curve was determined empirically at a value of 70°. The associated cutting width was 16,5 mm. The machined length was 130 mm for each experiment.

3. Results

This chapter presents the results of experiment. Experiments 3., 6. and 9. are flawed, because the relationship between the cutting speed and the feed rate was not calculated, so during machining it was observed that the feed rate was higher than the cutting speed, which resulted in damage to the tool body as observed in **Figure 6.** Thus, experiments 3., 6. and 9. cannot be evaluated.

3.1. Cutting forces and torques

The cutting forces in the „z" direction measured during the experiments are shown in **Figures 7–9**, while the cutting torques are shown in **Figures 10–12**.

Based on the measurement results shown in **Figures 7–12**, it can be concluded that, in general, the cutting forces and torques increase in a linear relation to the increase in the depth of cut and feed per tooth. The lowest tool load is observed in experiment 1, while the highest is observed in experiment 5. It can be concluded that the feed per tooth has the greatest impact on the tool load.

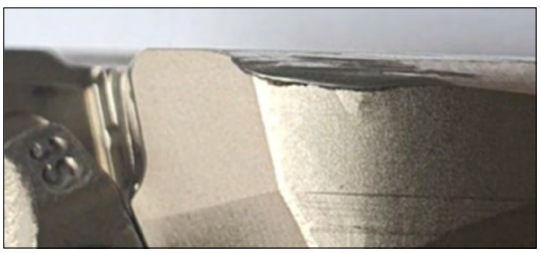

Figure 6. *Damaged tool body.*

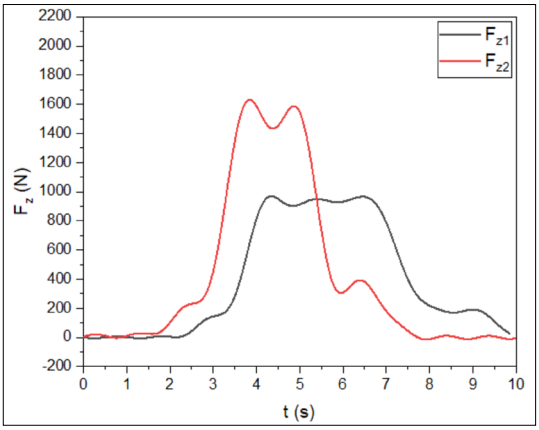

Figure 7. *Cutting forces F_z measured in the Experiments 1-2. as a function of machining time.*

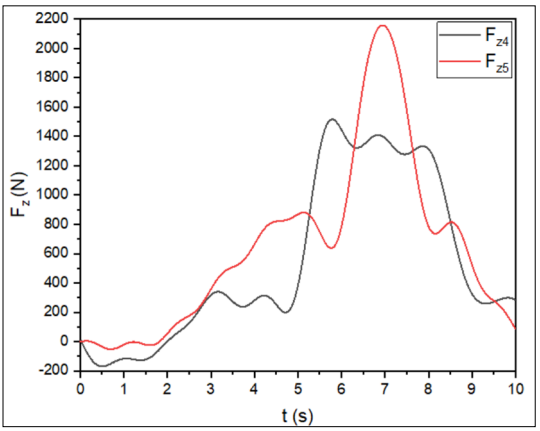

Figure 8. *Cutting forces F_z measured in the Experiments 4-5. as a function of machining time.*

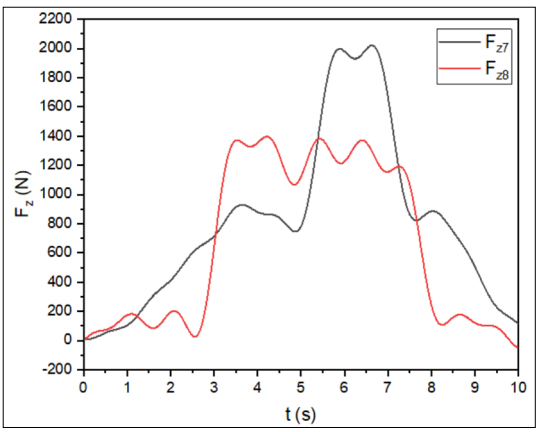

Figure 9. *Cutting forces F_z measured in the Experiments 7-8. as a function of machining time.*

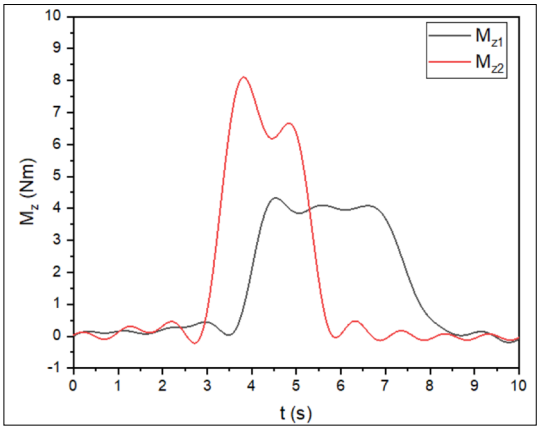

Figure 10. *Cutting toques M_z measured in the Experiments 1-2. as a function of machining time.*

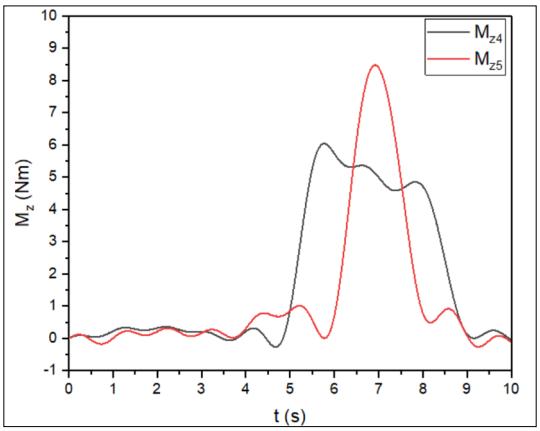

Figure 11. *Cutting toques M_z measured in the Experiments 4-5. as a function of machining time.*

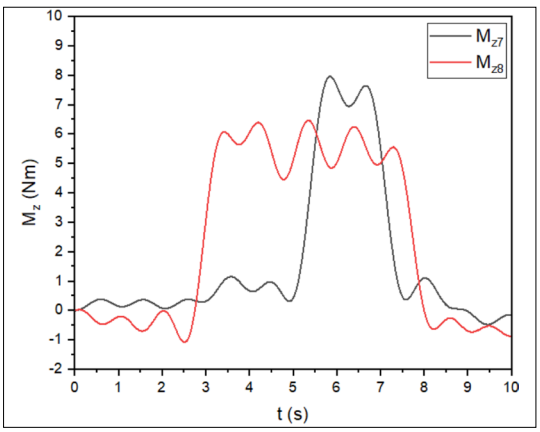

Figure 12. *Cutting toques M_z measured in the Experiments 7-8. as a function of machining time.*

3.2. Investigation of cutting inserts

Photographs of the inserts used during machining are shown in **Figure 13**. During the machining process the formation of built-up edge along the tool edge was typical, and some wear was also observed. One insert is broken, most likely due to impact effect during machining.

The built-up edge rate could be greatly reduced if compressed air cooling was used to improve chip separation. Holes are provided in the tool body for this purpose, but the machine centre used for the research is not suitable for such cooling. Experience shows that higher cutting speed is preferable.

4. Conclusion

In this research, the authors investigated the machinability of GTD-111 type Nickel-based superalloy during face milling. Using Taguchi-method, an experimental plan was prepared and the applied cutting forces and torques were measured during the experiments. The authors have stated the following conclusions:

- it is advisable to check the correctness of the experimental design before carrying out the experiments;
- of the technological parameters, the feed per tooth has the greatest impact on the machining process;
- it is advisable to use a higher cutting speed to avoid the formation of built-up edge;
- compressed air cooling is recommended when machining with ceramic tools.

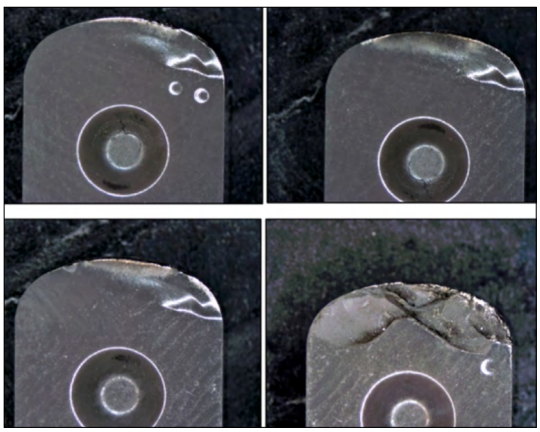

Figure 13. *The cutting inserts used during experiments.*

References

[1] Thellaputta G. R., Chandra P. S., Rao C. S. P.: *Machinability of Nickel Based Superalloys: A Review*. Materials Today: Proceedings, 4/2. (2017) 3712–3721. https://doi.org.10.1016/J.MATPR.2017.02.266

[2] Kun K., Kodácsy J., Vaczkó D., Kovács Zs. F.: *Machinability of Ni-based Superalloys by Indexable End Mills.* Acta Materialia Transylvanica, 2/1. (2019) 49–54. https://doi.org/10.33924/amt-2019-01-08

[3] Ulutan D., Ozel T.: *Machining induced surface integrity in titanium and nickel alloys: A review.* International Journal of Machine Tools and Manufacture, 51/3. (2011) 250–280. https://doi.org/10.1016/J.IJMACHTOOLS.2010.11.003

[4] Olufayo O. A., Boulaares D. M., Songmene V.: *Machining/machinability of Rene 65 superalloy for aerospace applications*. In: Proceedings of 2020 IEEE 11th International Conference on Mechanical and Intelligent Manufacturing Technologies, ICMIMT 2020. South Africa, 2020. 1–7. https://doi.org/10.1109/ICMIMT49010.2020.9041189

[5] CNC Media, *Szuperötvözetek egykristályok – drágakövek a gázturbinákban.* (accessed on: 2023. 02. 07.) https://www.cnc.hu/2014/01/szuperotvozet-egykristalyok-dragakovek-a-gazturbinakban/

[6] Kodácsy J., Kovács Zs. F., Viharos Zs. J.: A *Ni-bázisú szuperötvözetek megmunkálhatósága horonymaráskor*. Gradus, 2/2. (2015) 142–146.

[7] Kónya G., Kovács Zs. F., Kókai E.: *Milling of Nickel-based superalloy by trochoidal strategies.* In: 2022 IEEE 22nd International Symposium on Computational Intelligence and Informatics and 8th IEEE International Conference on Recent Achievements in Mechatronics, Automation, Computer Science and Robotics (CINTI-MACRo), Magyarország, 2022. 1–6. https://doi.org/10.1109/CINTI-MACRo57952.2022.10029453

[8] Sourmail T.: *Coatings for Turbine Blades.* 2003. http://servidor.demec.ufpr.br/disciplinas/EME715/AT%20PGMEC/Artigos%20para%20Semin%C3%A1rio/artigo%20cambridge%20coatings.pdf (accessed on: 2023. 02. 03.)

[9] Kodácsy J., Viharos Zs. J., Kovács Zs. F.: *A forgácsolhatóság meghatározásának módszerei Ni-bázisú szuperötvözetek horonymarásakor*. Gépgyártás, 15/2. (2015) 125–129.

[10] Zhang B. Y., Zeng Y. N., Pang X., Li S. Q., Liu X., Deng W. J.: *Feasibility analysis and process characteristics of selective laser ablation assisted milling Inconel 718.* Advances in Manufacturing, 10. (2022) 495–519. https://doi.org/10.1007/s40436-021-00384-9

[11] Sajjadi S. A., Nategh S., Guthrie R. I. L.: *Study of microstructure and mechanical properties of high performance Ni-base superalloy GTD-111*. Materials Science and Engineering, 325/1–2. (2022) 484–489. https://doi.org/10.1016/S0921-5093(01)01709-9

[12] Diniz A. E., Ferrer J. A. G.: *A comparison between silicon nitride-based ceramic and coated carbide tools in the face milling of irregular surfaces*. Journal of Materials Processing Technology, 206/1–3. (2008) 294–304. https://doi.org/10.1016/j.jmatprotec.2007.12.035

sciendo

Acta Materialia Transylvanica 6/1. (2023) 29–32.
DOI: Hungarian: https://doi.org/10.33923/amt-2023-01-05
English: https://doi.org/10.33924/amt-2023-01-05

ACTA MATERIALIA TRANSYLVANICA

Effects of Plasma Nitriding Temperature on the Properties of 1.3207 Type High Speed Steel

Krisztián KORSÓS,[1] Dorina KOVÁCS[2]

[1] *Budapest University of Technology and Economics, Faculty of Mechanical Engineering, Department of Materials Science and Technology, Hungary, korsos.krisztian@edu.bme.hu*

[2] *Budapest University of Technology and Economics, Faculty of Mechanical Engineering, Department of Materials Science and Technology, Hungary, kovacs.dorina@gpk.bme.hu*

Abstract

Active screen plasma nitriding on HS 10-4-3-10 high-speed steel specimens was performed at three different low nitriding temperatures while trying to keep the other nitriding parameters uniform. In addition, two extra samples were made to increase the treatment time. Optical microscopic investigation and microhardness testing were performed on the segments of the samples, and their qualitative composition was determined by energy-dispersive X-ray spectrometry. Based on the measurements, it is stated that the hardness of the surface can be increased 50% with active screen plasma nitriding.

Keywords*: active screen, plasma nitriding, high-speed steel.*

1. Introduction

In the 21st century, the requirements for steel are becoming stricter, and the expectations more complex. Different mechanical properties are often required on the surface and cross-section of the material. In this case, creating a heterogeneous microstructure in a cross-section can be a solution. There are two options for this: changing the microstructure of the surface, or modifying the chemical composition in the surface layer. The latter group of solutions includes the thermochemical process we chose, nitriding. [1, 2]

In this thermochemical surface treatment through adsorption and diffusion, nitrogen is delivered to the material's surface, where it creates metalloid phases and a high hardness and wear-resistant layer. The quality of nitriding is influenced by the carbon and other alloy content of the steel in addition to the process parameters. The effect of alloying elements is based primarily on their affinity for nitrogen, similar to iron. Based on the free energy required for the formation of different nitrides, the stability of each alloy can be deduced, and in this way, can be distinguished as strong, medium, and weak nitride formers. Alloys have two significant effects during nitriding: it reacts with nitrogen through diffusion, forming hard nitrides and increasing the surface hardness, and it decelerates the diffusion of nitrogen, thus reducing the depth of the formed layer. From an industrial perspective, the hardest surface is not desirable, but the goal is to create a deep, mechanically resistant layer using the most economical production method [3].

In previous research, high-speed steels were already treated with a traditional, direct current plasma nitriding process [4, 5]. Akbari et al. [6] determined that after 8 hours of nitriding, a 140 µm diffusion zone was created without a compound layer containing scattered Fe3N and Fe4N precipitates. During our research, we carried out active screen plasma nitriding at different temperatures on the 1.3207 high-speed steel material quality in order to discover whether these properties of high-speed steel with excellent hardness and wear resistance can be increased, given the typically high alloy content of high-speed steels.

2. Experimental methodology

The next chapter will describe the chosen material, technology, and methods.

2.1. Material

The chosen steel has outstanding hardness and wear resistance among commercially available high-speed steels yet poor machinability. From the point of steel using view, it is an excellent turning and milling tool for roughing and finishing work, woodworking tools, heavy-duty cold working tools and tool inserts.

The alloys of the selected material are nitride formers, and their quantity is also high in the steel, so because of the treatment, an outstanding surface hardness and thin layer thickness will be expected at the same time [7].

The material quality used for the research nominally includes the following alloys based on the ISO 4957 standard: 1.2 – 1.35% C, ≤0.4% Mn, ≤0.45% Si, ≤0.03% S, 3.8–4.5% Cr, 3.2–3.9% Mo, 3.0–3.5% V, 9.0–10.0% W, 9.5–10.5% Co, and Fe.

The samples were used for the treatment, also known as 1.3207 (HS10–4–3–10) steel. It was acquired in the form of a 12×3×160 mm rod. This steel is also commercially available under the name HSS CO10.

2.2. Active screen plasma nitriding

The active screen was used during the surface treatment process, which was made from unalloyed steel with a diameter of 100 mm and a hole diameter of 8 mm.

The effect of the material of the screen and its distance from the sample was neglected, considering that all 5 test specimens were affected uniformly by these parameters.

The voltage and the pressure of the 75% N_2 - 25% H_2 gas mixture were kept at the same value. Since the primary goal is to maintain the temperature set for the sample, it was sometimes necessary to slightly deviate from the uniform pressure or voltage during the entire treatment time. The treatment parameters and produced samples are listed in Table 1:

2.3. Methods

The sample cross-sections were prepared by grinding on SiC paper after the surface treatment, followed by polishing with 3 and 1 μm diamond suspension. The completed samples were etched with a Beraha II-type etchant [8].

The formed surface layer was examined with a scanning electron microscope (type: Zeiss Evo Ma 10), and the surface nitrogen content of the samples was measured with an energy dispersive X-ray spectrometer, thus proving the success of the surface treatments, establishing the effectiveness of the different treatment temperatures.

Finally, microhardness tests were carried out with a load of 200 grams to record the hardness profile and the surface hardness of the samples, for which a Buehler 1100 type microhardness tester was used.

3. Results and discussion

Based on the scanning electron microscope examinations, no compound layer was formed on the surface of the high-speed steel samples during the entire treatment in the temperature range and treatment times, which can also be observed in Figures 1. and 2. The surface composition analysis made with an energy dispersive X-ray spectrometer reliably measured the nitrogen content of all samples (Table 2). The measurement was carried out along the cross-sectional, on the part marked with yellow in Figure 2.

It can be concluded that a compound layer was not formed on the samples, but a diffusion layer was formed. The nitrogen content was increased with increasing treatment temperature or treatment time.

This phenomenon can be attributed to faster diffusion at higher temperatures or to the time available for the phenomenon to occur [9].

The result of the hardness measurement can be seen in Figure 3.

Table 1. *Nitriding parameters of the samples produced for the examinations*

No.	Temperature (°C)	Time (h)
1	360	5
2	440	5
3	520	5
4	360	8
5	520	8

Table 2. *Measurement data on the cross-sectional in the subsurface (weight ratio, %)*

No.	N	V	Mo	W	Co
1	3.03	1.25	1.93	5.15	9.57
2	4.56	1.09	2.3	4.21	9.91
3	6.18	5.75	4.35	11.7	9.79
4	6.99	2.73	3.90	8.56	8.55
5	13.0	2.46	4.33	9.45	9.52

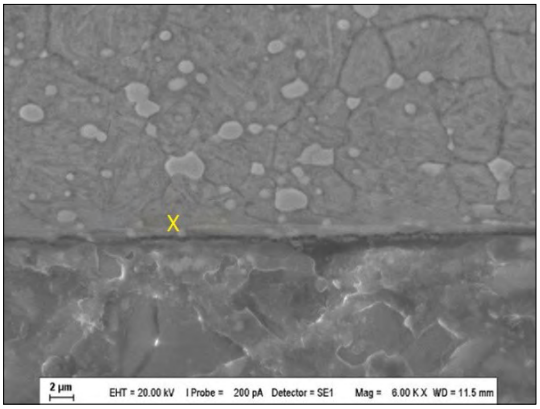

Figure 1. *Cross-section of the sample treated at 520 °C for 5 hours (yellow cross marks the measurement spots).*

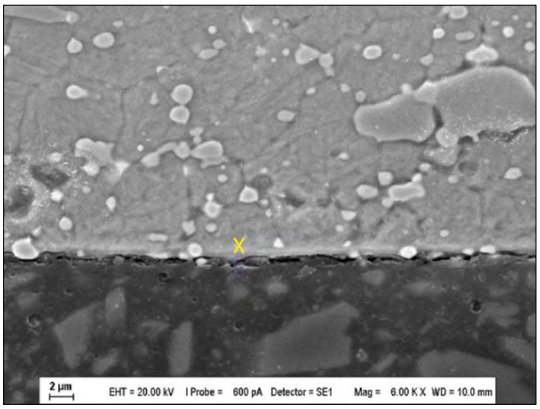

Figure 2. *Section of the sample treated at 520 °C for 8 hours (yellow cross marks the measurement spots)*

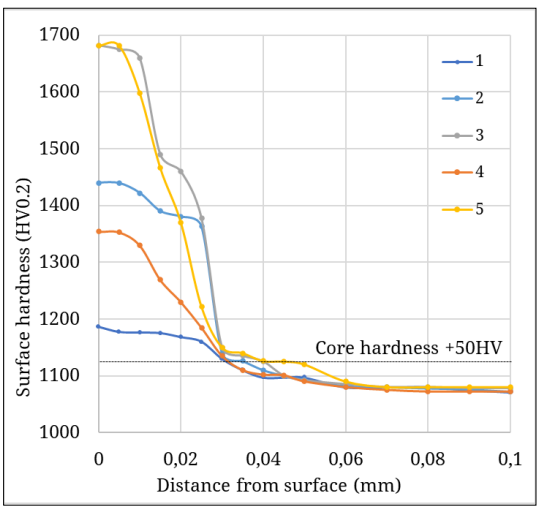

Figure 3. *Hardness profile of samples.*

Table 3. *The layer thickness of the diffusion zone*

No.	Layer thickness (µm)
1	31
2	36
3	40
4	33
5	45

It can be clearly seen that the maximum hardness was increased with increasing temperature. Based on the ISO 18203:2016 standard, the developed diffusion layer thicknesses were determined using the curves. The value of the surface layer thickness was equal to the point where the core hardness + 50HV was reached. **[10]**. **Table 3** contains the determined values.

4. Conclusions

With the technology of active screen plasma nitriding of high-speed steels, the surface hardness can be increased even at low temperatures, while at higher applied temperatures, the hardness value increases significantly. By increasing the time, the surface hardness can be effectively increased at lower temperatures but not at higher temperatures.

The layer thickness of the diffusion zone can be increased minimally during the nitriding of high-speed steels by increasing the temperature, but no compound layer was formed. By increasing the treatment time, the thickness of the formed diffusion layer can be increased more significantly.

It is concluded that a compound layer cannot be formed by active screen plasma nitriding during a processing time of 5–8 hours, while the diffusion zone was created even at the lowest test temperature.

Acknowledgement

This work was supported by the National Research, Development and Innovation Office (NKFIH), under grant agreement OTKA PD_22 142307.

References

[1] Szabó A., Szlancsik A.: *Titán alapú aktív ernyős plazmanitridálás.* In: XXVIII. Nemzetközi Gépészeti Konferencia – OGÉT 2020. Kolozsvár, Románia, 354. 2020. 85–88.

[2] Naeem M., Qadeer M., Mujahid Z., Rehman N. U., Díaz-Guillén J. C., Sousa R. R. M, Shafiq M.: *Time-resolved plasma diagnostics of cathodic cage plasma nitriding system with variable pulsed duty*

cycle and surface modification of plain carbon steel. Surface and Coatings Technology, 464. (2023) https://doi.org/10.1016/j.surfcoat.2023.129542.

[3] Thelning K.: *Steel and its Heat Treatment.* Butterworths, 1984. 492–544.

[4] Tier M., Bloyce A., Bell T., Strohaecker T.: *Wear of plasma nitrided high speed steel,* Surface Engineering, 14/3. (1998) 223–228. https://doi.org/10.1179/sur.1998.14.3.223

[5] Kwietniewski C., Fontana W., Moraes C., Rocha A.da S., Hirsch T., Reguly A.: *Nitrided layer embrittlement due to edge effect on duplex treated AISI M2 high-speed steel*. Surface and Coatings Technology, 179/1. (2004) 27–32. https://doi.org/10.1016/S0257-8972(03)00795-3.

[6] Akbari A., Mohammadzadeh R., Templier C., Riviere J.P.: *Effect of the initial microstructure on the plasma nitriding behavior of AISI M2 high speed steel.* Surface and Coatings Technology, 204/24. (2010) 4114–4120. https://doi.org/10.1016/j.surfcoat.2010.05.042

[7] Davis J. R.: *Machining* ASM International, Ohio, ASM Handbook, 16. (1989) 51–59.

[8] Renkó J. B., Szabó P. J.: *Investigation of the Effect of Over-Etching During Color Etching.* Acta Materialia Transylvanica, 5/1. (2022) 29–34. https://doi.org/10.33924/amt-2022-01-07

[9] *Liquid nitriding of steels*. In: ASM Handbook 4A.: *Steel Heat Treating. Fundamentals and Processes.* (Szerk.: Dossett J. L., Totten G. E.), ASM International, Ohio, (1991) 680–689.

[10] ISO 18203:2016: Steel – Determination of the thickness of surface-hardened layers.

sciendo

Acta Materialia Transylvanica 6/1. (2023) 33–37.
DOI: Hungarian: https://doi.org/10.33923/amt-2023-01-06
English: https://doi.org/10.33924/amt-2023-01-06

ACTA MATERIALIA TRANSYLVANICA

Effects of injection Moulding Parameters on the Produced Parts

György LEDNICZKY,[1] Zoltán WELTSCH[2]

[1] *John von Neumann University, GAMF Faculty Engineering and Computer Science, Dep. of Innovati-ve Vehicles and Materials, Manufacturing Technology Research Group, Kecskemét, Hungary, ledniczky.gyorgy@gamf.uni-neumann.hu*

[2] *John von Neumann University, GAMF Faculty Engineering and Computer Science, Dep. of Innovati-ve Vehicles and Materials, Manufacturing Technology Research Group, Kecskemét, Hungary, weltsch.zoltan@sze.hu*

Abstract

The publication deals with an innovative technology called powder-based metal injection moulding, which is a combination of traditional polymer injection moulding and powder metallurgy. With the technology, it is possible to produce metal components with complex geometry in large series. There is an extremely large selection of materials that can be used, mostly steel, copper, titanium or nickel-based alloys. In this research, the material used is type 17-4PH, martensitic corrosion-resistant steel, and since it is a widely used material, it is examined in many international articles and research studies, and it is also common in industry, so it is advisable to use this type of material for further comparability. Little information can be found in the literature about spraying parameters and their effects, which is why this research focusses on this. On the other hand, these data can also serve as useful information for the industry. During the production of so-called green products, the effects of product shrinkage were measured by changing the most important parameters and comparing the effects of these parameters to traditional polymer injection moulding.

Keywords*: metal injection moulding, shrinkage, stainless steel.*

1. Introduction

In industry, an increasingly widely used process is metal injection moulding (MIM), which allows for the production of complex geometry metal components with high precision and in large quantities. One of the major application areas of this process is the automotive industry, where it is employed for the production of relatively small-sized products. There is a wide range of materials that can be used, but iron-based alloys, titanium alloys, and copper alloys are predominantly used. A literature review reveals very limited information regarding the impact of moulding parameters on the properties of the product. Therefore, the first step in the research is to investigate how the moulding parameters affect the shrinkage of the product and to what extent this resembles what is observed in plastic injection moulding [1].

1.1. Metal injection moulding technology

Metal injection moulding can be described as a combination of traditional injection moulding and powder metallurgy. It involves using a granular feedstock with high metal powder content (95% by weight) and a binder consisting of 5% thermoplastic material. This feedstock is injected into a mould using an injection moulding machine. The resulting product is called a „green part." To create a porous structure throughout the entire cross-section of the product, the amount of binder needs to be reduced. There are various methods for removing the binder, depending on the specific binder system [2]. It is important for the binder to create a porous product while still providing enough binding strength to hold the powder particles together. The product with reduced binder content is referred to as a „brown part." The next step in the process is the sintering

phase. The part is heated in a high-temperature furnace below the melting point until it reaches the desired density characteristic of the material. At this stage, the component acquires its metallic properties and sound [1]. The overall process can be seen in Figure 1.

So it can be seen that I am examining a narrow range of the MIM process, namely the injection moulding phase.

1.2. Effect of parameters on shrinkage

By changing the moulding parameters, it is possible to modify the dimensions of the injection-moulded product, which is directly related to shrinkage. The melt temperature, mould temperature, and post-injection pressure are among the main influencing factors. In the case of MIM, we may not observe the same processes as in plastic injection moulding, as the processed feedstock contains only a small percentage of polymer materials and is three-component due to the two-stage binder removal. Increasing the mould and melt temperature generally increases the shrinkage value. Increasing the post-injection pressure achieves a decreasing effect on shrinkage [4, 5].

2. Experiment and methodology

In this chapter, we present the tools used for measuring moulding parameters, the materials used, the mould, and the parameters of the experiment.

2.1. The raw material of the experiment

The selected material is martensitic corrosion-resistant steel, commercially known as 17-4PH, and its main components are listed in Table 1. [6]. This material is commonly used in both MIM and additive manufacturing processes, which is why it is advantageous to use it [7]. Apart from its corrosion resistance, it exhibits excellent mechanical properties, making it widely utilized in various industrial applications. It is frequently employed in aerospace and space technology, as well as in the oil and gas industry. It is used for the production of screws, springs, nails, gears, and also finds applications in the medical field for manufacturing surgical instruments. The binder used in the process consists of two main components: polypropylene and wax, which are mixed with the metal powder at a ratio of 6% by weight [8].

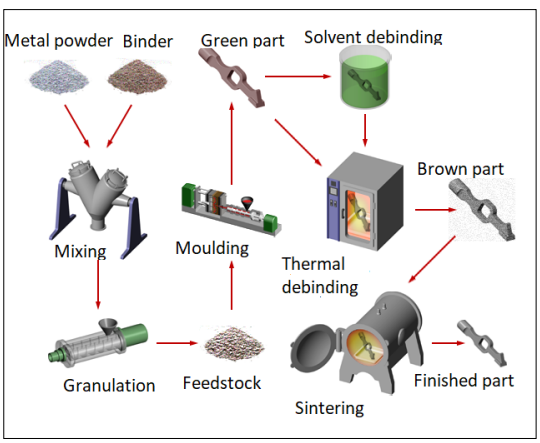

Figure 1. *The process flowchart of metal injection moulding [3]*

2.2. Test tool

To conduct the tests, we used a production mould specifically designed for creating a test specimen that weighed approximately 36 grams. This mould is capable of facilitating various types of tests. It is equipped with cooling channels on each side and features a central inlet from which a short runner feeds the mould cavity. The mould used for the experiment is illustrated in Figure 2. AFT Hungary Ltd provided us with the tool and the possibility to test the tool.

Table 1. *A 17-4 PH corrosion-resistant steel main components 1.4542 [7]*

%	Cr	Mn	Si	Ni	Cu
Min.	15,0	–	–	3,50	3,00
Max.	17,5	1,00	0,70	5,00	5,00

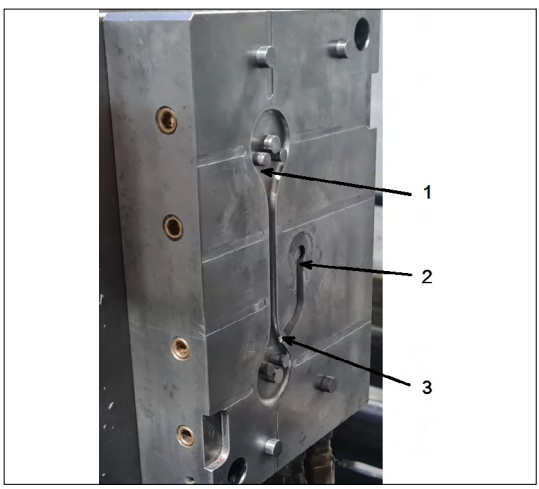

Figure 2. *The tool used for the test. 1- Cavity, 2-Runner, 3-Gate*

2.3. Technological parameters

To determine the precise moulding parameters, we conducted preliminary injection moulding trials. In order to examine the effects of the parameters, it was necessary to establish an optimal set of technological settings within the processing limits. The switching point was set at 99% cavity filling (Figure 3) with the dosing quantity continuously increasing.

The melt temperature was selected as the average processing temperature of the polyethylene (PE) component of the binder, and the value of the holding pressure was set to the midpoint between the two extremes of the processing limits. The optimal mould temperature was determined empirically through experimental observations.

Table 2. *The defined processing parameters*

Parameter	Value
Injection volume	6.56 cm^3/s
Injection pressure	903 bar
Postpress time	2 s
Post pressure	827 bar
Cooling time	15 s
Tool temperature	45°
Melt temperature	205 °C

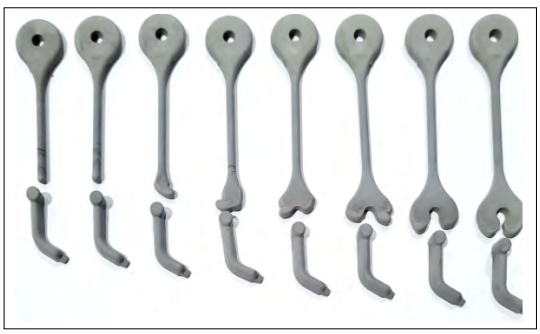

Figure 3. *Fill sequence to define the switching point.*

2.4. Changed parameters

During the experiment design, the primary objective was to vary the key parameters, namely melt temperature, mould temperature, and holding pressure, individually in each case. As a result, 16 different technological settings were generated. The first 5 shots were disregarded to allow the process to stabilize and reach thermal equilibrium. Subsequently, for each configuration, 10 test specimens were produced, with 5 of them left as green parts, while the other 5 underwent additional steps (binder removal, sintering).

Table 3. *The changed parameters and corresponding values*

Variable	Back press.	Tool temp.	Melt temp.
Deviation -	550 bar	25°C	195°C
Deviation -	690 bar	35°C	200°C
Average alue	827 bar	45°C	205°C
Deviation +	965 bar	55°C	210°C
Deviation +	1103 bar	65°C	215°C
Deviation +	1241 bar	75°C	220°C

3. Results

After completing the trial injections, we proceeded with the evaluation of the results. Initially, we examined the samples that had not undergone sintering or binder removal. However, due to the variation in injection moulding parameters, the products exhibited flash along the parting line (Figure 4) which would have affected the measurement of hole distances. To obtain more accurate measurement results, we manually deburred all the holes in the fabricated samples. As a result, the distances between the holes could be precisely measured.

Following the removal of flash, we measured the distances between the holes (Figure 5) using an optical measuring machine. Therefore, the values of linear shrinkage correspond to these distances.

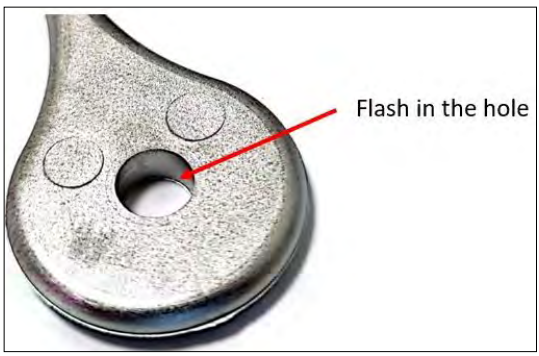

Figure 4. *Burring of the test specimen's hole.*

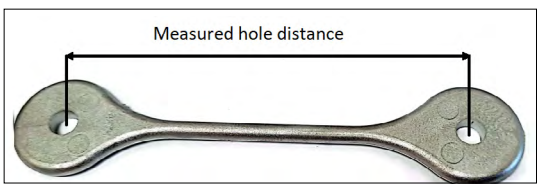

Figure 5. *Measured value of linear shrinkage.*

The obtained results were plotted on a diagram, illustrating the relationship between the variable property and shrinkage. The data represents the average of samples taken after 5 shots from the new material.

Shrinkage was determined using the following equation:

$$Shrinkage = \left(\frac{tool\ distance}{part\ distance} - 1\right) \cdot 100$$

The parameter that mostly influences the product size is the tool temperature (**Figure 6**). The shrinkage ranged from 0.34% to 0.72%, which can be considered a significant deviation, resulting in a dimensional difference of approximately 0.4 mm over a test length of 100 mm.

The curve shows an increasing trend similar to plastic injection moulding but only up to a temperature of 55°C. Beyond this temperature, the shrinkage value starts to decrease again. During the trials, it was observed that at higher tool temperatures, the products would come out of the mould with a „wet" appearance. This could potentially be attributed to wax exudation from the binder (**Figure 7**) As a result, metal particles could replace the exuded wax, resulting in a smaller shrinkage factor. It is hypothesized that this could be measured based on the percentage composition of the components.

The relationship between shrinkage and the variation of applied pressure differs from that of polymers. Based on the results, shrinkage reaches its maximum around 900 bar (**Figure 8**), leading to less shrinkage at higher or lower pressure values. It should be emphasized that the impact of applied pressure on shrinkage is significantly smaller compared to that of tool temperature.

The deviations from plastic processing parameters can be attributed to several factors; however, further research is required to fully understand them.

Among the parameters studied, the variation in melt temperature had the least effect on product dimensions, and the scatter of the curve was significant compared to the deviations (**Figure 9**).

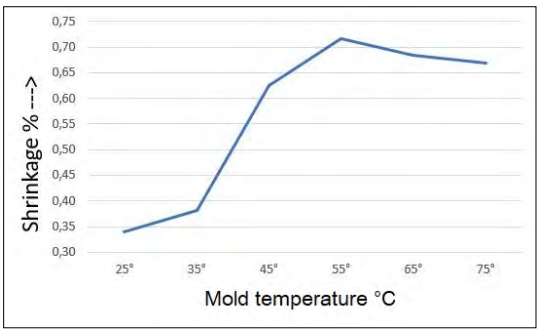

Figure 6. *Effect of tool temperature on shrinkage.*

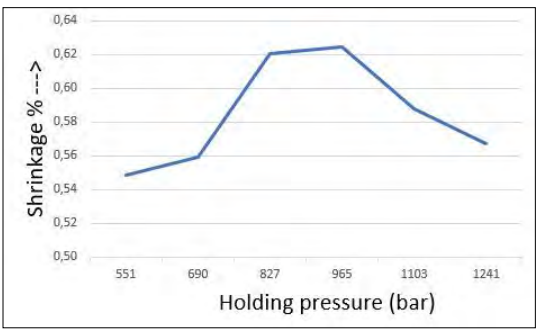

Figure 8. *Effect of holding pressure on shrinkage.*

Figure 7. *Wet product surface, possible wax separation.*

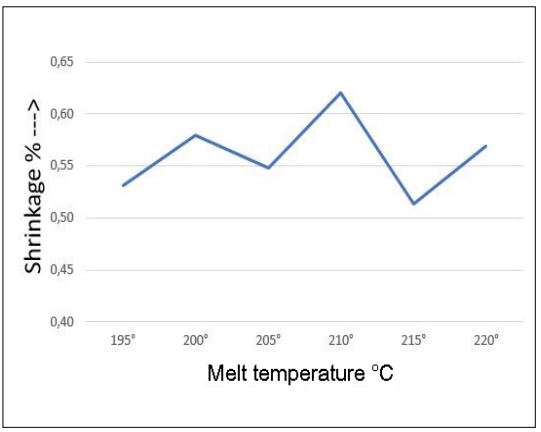

Figure 9. *Effect of melt on shrinkage.*

4. Conclusions

Based on the results of the conducted experiments, it can be summarized that the general principles of polymer injection moulding may not necessarily be applicable to metal powder processing. The physical properties of the materials show significant differences, such as varying density, viscosity, thermal conductivity, and the behaviour of a three-component system needs to be examined.

However, the preliminary measurement results are not sufficient to draw definitive conclusions. Further tests and investigations are necessary to validate the obtained results and ensure their reliability. Therefore, additional examinations are required to apply more effective methods for optimizing the injection moulding process and improving the quality of the final product.

Based on the tests, it can be assumed that other factors also influence shrinkage, especially in the case of pressure and mould temperature. The most significant effect is observed when changing the mould temperature. The influence of melt temperature is not known, and measurement errors may occur, which require further measurements.

Acknowledgment

We thank AFT-Hungary Kft. for their generous help in securing the raw materials and technology.
This work was supported by the Janos Bolyai Research Scholarship of the Hungarian Academy of Sciences.

References

[1] Heaney D. F.: *Handbook of Metal Injection Molding*. 2. kiadás Woodhead Publishing Series in Metals and Surface Engineering, Cambridge, (2019) 1–25.

[2] Petzoldt F., Eifert H., Hartwig T., Kramer L., Veltl G., Pest A.: *Broadening the Scope of MIM*. Materials and Manufacturing Processes, 12/4. (1997) 691–711. https://doi.org/10.1080/10426919708935176

[3] Custom Part USA, *Metal Injection Molding* https://www.custompartnet.com/wu/metal-injection-molding (accessed on: 2023. 03. 01.).

[4] Barriere Th., Liu B., Gelin J. C.: *Determination of the optimal process parameters in metal injection molding from experiments and numerical modeling*. Journal of Materials Processing Technology, 143–144. (2003) 636–644. https://doi.org/10.1016/S0924-0136(03)00473-4.

[5] Tseng W. J.: *Statistical analysis of process parameters influencing dimensional control in ceramic injection molding*. Journal of Materials Processing Technology 79/1–3. (1998) 242–250. https://doi.org/10.1016/S0924-0136(98)00019-3

[6] Amatek Specialty Metal Products. *Specialty Powders 17.4 PH Alloy Powder* https://www.powderclad.com/products/specialty-powders/17-4-ph-alloy-powder

[7] Singh G., Missiaen J.-M., Bouvard D., Chaix J.-M: *Additive manufacturing of 17–4 PH steel using metal injection molding feedstock: Analysis of 3D extrusion printing, debinding and sintering*. Additive Manufacturing, 47. (2021) 102287. https://doi.org/10.1016/j.addma.2021.102287.

[8] Hamidi M. F. F. A., Harun W. S. W., Khalil N. Z., Ghani S. A. C., Azir M. Z.: *Study of solvent debinding parameters for metal injection moulded 316L stainless steel.* IOP Conference Series: Materials Science and Engineering, 257. (2017) 012035. https://doi.org/10.1088/1757-899X/257/1/012035.

sciendo

Acta Materialia Transylvanica 6/1. (2023) 38–41.
DOI: Hungarian: https://doi.org/10.33923/amt-2023-01-07
English: https://doi.org/10.33924/amt-2023-01-07

ACTA MATERIALIA TRANSYLVANICA

Fabrication of In-situ Syntactic Aluminium Foam-Filled Steel Tubes

Gábor PADOS,[1,2,a*] Alexandra KEMÉNY,[1,2,b] Benedek SZOVÁK,[1,2,c] Dóra KÁROLY,[1,2,d] Imre Norbert ORBULOV[1,2,e]

[1] *Department of Materials Science and Engineering, Faculty of Mechanical Engineering, Budapest University of Technology and Economics. Budapest, Hungary.*

[2] *MTA-BME Lendület Composite Metal Foams Research Group, Budapest, Hungary.*

[a*]*padosgabor@edu.bme.hu,* [b] *kemeny.alexandra@gpk.bme.hu,* [c] *szovak.benedek@edu.bme.hu,*

[d] *karoly.dora@gpk.bme.hu,* [e] *orbulov.imre.norbert@gpk.bme.hu*

Abstract

In all areas of industry, when choosing a material, compromises must be made since there is no material with all the properties that are preferential for any use. In the automotive sector, lighter and less dense materials can provide a considerable advantage, for example, lower fuel consumption due to weight reduction. Specialists dealing with materials science within metal foams have been trying to exploit the low density, high specific strength and high energy absorption capacity of metal foams in as many ways as possible for a long time. This research describes the one-step production method of syntactic metal foams with an aluminum matrix infiltrated into a thin-walled steel tube, intended to create functional structures with a strong adhesive bond and metal foam filling in a feasible way.

Keywords*: metal matrix syntactic foam, foam-filled tubes, low-pressure infiltration.*

1. Introduction

Syntactic metal foams are produced mainly by themselves and not as functional, structural elements [1–3]. Recently, however, more and more research has been dealing with metal foam-filled tubes (FFTs), which examine metal foams placed in tubes of a certain wall thickness. Because the properties of metal foams can be further increased if they are filled in hollow closed (metal) sections, the metal foam filling and the closed section surrounding it can support each other[4].

The tubes filled with metal foams are more resistant to different types of loads than the metal foams themselves. Compression and bending are the two most important stresses in such structures, which is why researchers mainly characterize foam-filled tubes with these properties. The production of these structures can be done in two ways: in one step, which is called the in-situ method or in multiple stages, which is called ex-situ. In the case of the in-situ method, the foam production process already takes place in the closed section. In contrast, in the case of the ex-situ method, the metal foam is reduced to the appropriate size after production, then placed in a pipe or fixed in some way.

Linul et al. [5, 6] investigated the effect of different temperatures on the axial quasi-static compaction of metal foams placed in circular tubes. The material of the foam was A356 (AlSi7Mg). The closed-cell foams were produced by stir casting and cut into Ø20×20 mm pieces. The density of the foams was 0.38–0.46 g/cm³. The specimens were placed in circular X5CrNi18-10 stainless steel tubes. Their outer dimensions were Ø22×20 mm, with a wall thickness of 1 mm, without any adhesive. In that research, quasi-static compression tests were performed with a crosshead speed of 10 mm/min at room temperature and elevated temperatures (150°C, 300°C and 450°C). The compressed specimens were examined by scanning electron microscopy (SEM) and optical microscopy (OM) methods. As the temperature increased,

the brittle behavior of the aluminum foam changed to a ductile one, and above 150°C, the peak stress difference between the empty tubes and the foam-filled tubes started to decrease due to the softening of the aluminum foam filling. It was also observed that the foam in the tube reduced the size and distribution of microcracks.

Only a few in-situ produced metal foam-filled tubes can be found in the scientific literature, detailed below.

Duarte et al [7] manufactured closed-cell AlSi7 foams with a solid aluminum skin using the powder compact foaming technique by placing the foamable precursor in an AlMgSi0.5 tube and holding it there at 700°C for 12 minutes. The manufacturing method resulted in a tight fit of the foam but reduced strength and energy absorption due to quasi-static and dynamic axial compression in the tube material.

Kemény et al. [8] manufactured samples created in one step by low-pressure infiltration, where the molten matrix material (AlSi12) was poured directly into an AlMgSi0.5 tube filled with expanded clay aggregates. The small difference in melting point of the matrix and the tube material required precise adjustment of the infiltration parameters. The outer diameter of the produced specimens was Ø50 mm, and the inner diameter was Ø40 mm. The manufacturing process in that research is very similar to the process used in the present research; however, an important difference is the material and wall thickness of the tube used during the one-step production, as well as the difference in the equipment used.

Chilla [9] and his research group investigated X2CrNiMo17-12-2 stainless steel tubes filled with closed-cell aluminum foam. The outer dimensions were Ø31.7×100 mm, and the wall thickness was 1.85 mm. Three types of test specimens were produced; in the first type, the metal foam was ex-situ inserted into the steel tube with a tight fit; in the second type of test specimens, the aluminum precursor was placed in the tube before foaming and foamed there, intending to form cohesion between the foam material and the tube material. In the third type of specimen, the inner surface of the steel tubes was galvanized with copper before foaming in the tube so that the copper layer promoted the formation of a strong bond between the foam and the tube. This was proven to be a successful procedure since after the aluminum foaming, the continuous copper coating disappeared, and a reaction product was formed on the interface between the foam and the pipe, which also contained aluminum, copper, tin and tin with iron.

Taherishargh et al. [10] produced syntactic metal foams filled into tubes in one step using the vacuum infiltration method. The specimens were made from an AlSi7Mg matrix and 2.0–2.8 mm expanded perlite particles. The infiltration took place inside X5CrNi18-10 stainless steel tubes, which had an outer diameter of Ø25.4 mm and a wall thickness of 0.9 mm and 1.2 mm. The specimens were examined with computed tomography (CT) and energy dispersive X-ray spectrometer (EDS) and were subjected to quasi-static axial compression and a three-point bend test. For compression, the crosshead speed was 3 mm/min, and for the bend tests, 0.1 mm/s and 284 mm/s crosshead speeds were applied up to 30 mm displacement. The overall properties of the 0.9 mm wall specimens were better, and EDS confirmed the bond between the matrix and the tube. The tensile strength was estimated based on flexural properties.

Movahedi and his research group [11] produced structures with circular tubes of Ø28×30 mm outer dimensions surrounded by syntactic metal foam. The specimens were produced in one step by counter-gravity infiltration, using Zn27Al-2Cu0.015Mg alloy, 2.0–2.8 mm expanded perlite aggregates and AlMgSi0.5 tubes. A tube with Ø12×36 mm outer dimensions and a wall thickness of 1.6 mm was placed in the mould's centre before infiltration, surrounded by expanded perlite particles. Scanning electron microscopy (SEM) images showed a tight fit between the tube and the matrix material, but EDS analysis showed no chemical reaction at the interface.

2. Materials and methods

During the research, in-situ syntactic metal foam-filled tubes were produced from an aluminum alloy matrix (Al-Si10MnMg – Silafont-36) and mild steel (S235) tubes, which had a wall thickness of 1 mm and an outer diameter of Ø30 mm. Lightweight expanded clay aggregate particles (LECAP) sold by Liapor GmbH & Co. KG were used as fillers.

3. In-situ manufacturing

The manufacturing process was managed with the assistance of pre-manufactured steel crucibles, which were 40×50 mm cross-section, 280 mm high rectangular-based, hollow section crucibles, and a thin-walled steel tube was welded inside

to the center of their base (Figure 1). The manufacturing process began with coating the inside of the steel crucibles and the outer surface of the welded steel tube with graphite emulsion. Then, the space between the outlet tube section that was welded to the side of the steel crucible and the thin-walled steel tube in the steel crucible was filled with alumina padding to prevent the melt from flowing through. There was also an outlet on the side of the thin-walled steel tube. The gap between the section and the tube was filled with aluminum padding up to a height of ~5 mm from the top of the outlet. After that, casting sand was used to fill the gap to the top of the inner tube, made of sand, bentonite and water. The function of the casting sand was to stop the molten aluminum from flowing between the tube and the section wall, thus avoiding an unnecessary amount of material adhering to the FFT. Due to the high thermal load capacity of the sand, it will not stick to the steel tube, so that it can be easily cleaned from the surface after casting. Another layer of alumina padding was placed around the upper part of the inner tube on top of the sand layer. The inner steel tube was filled with LECAPs with a diameter of Ø3.5–4.0 mm, and fixed in place with a stainless steel net on top, which prevents the displacement and floating of the LECAPs to the surface.

The steel crucibles were then placed in a Lindberg/Blue M furnace for preheating and heated to 400°C. The crucibles were kept at this temperature in the furnace for at least 45 minutes, so the temperature at all points was the same as that of the furnace. During the preheating, the AlSi10MnMg block serving as the matrix material was melted in an IND F-10 induction melting furnace until it was red. When it reached this condition, the induction furnace was turned off, and while the molten aluminum was cooling, the temperature of the melt was measured using a Maxthermo MD-3003 type K digital thermometer. In the used matrix material – filler particle – thin-walled steel tube system, a melt temperature of 820°C was necessary for successful fabrication, so the infiltration took place completely, even with the low preheating temperature. The pressure required for infiltration was applied to the crucible through a well-insulated pipe. The pressure came from a high-pressure argon bottle through a reducer, and a pressure of 0.4 MPa was used to press down the molten matrix material. After infiltration, the crucible was cooled under running cold water, then the outer crucible was removed, and in-situ FFTs in the state shown in the picture below (Figure 2) were obtained.

Finally, the unnecessary aluminum was cut off from the top of the steel tube, resulting in a syntactic metal foam-filled functional structure produced in one step. The cross-sectional view can be seen in Figure 3.

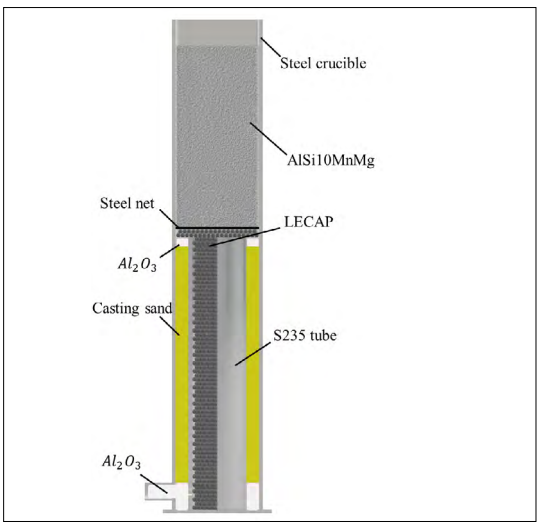

Figure 1. *Schematic figure of the in-situ foam-filled steel tube production.*

Figure 2. *In-situ produced syntactic metal foam-filled steel tube, after cooling.*

Figure 3. *Thin-walled in-situ syntactic FFT.*

The bulk density of the structure was determined based on geometric and mass measurements; its value was 2.30 ± 0.01 g/cm³, which is ~15% less than the density of the aluminium alloy used, and ~70% less than the density of the steel tube.

4. Conclusions

The following conclusions were drawn from the results of the research:

- low-pressure infiltration is a suitable melt route process for the one-step production of syntactic metal foam-filled steel tubes;
- during the research, a suitable mold was created for production;
- as a result, a functional structure was obtained with low density, which only needs to be cut before installation;
- further research of the manufactured structure is expected, primarily mapping its compression and bending properties based on the methods found in the literature.

Acknowledgements

The publication of the work reported herein has been supported by the NTP-SZKOLL-22-0080 National Talent Programme of the Ministry of Human Capacities. The research reported in this paper and carried out at BME has been supported by the NRDI Fund (TKP2022 IEs, Grant No. BME-IE-NAT; TKP2022 NC, Grant No. BME-NCS) based on the charter of bolster issued by the NRDI Office under the auspices of the Ministry for Innovation and Technology. This work was supported by the National Research, Development and Innovation Office (NKFIH) under grant agreement OTKA-FK_21 138505.

References

[1] Hong K., Kádár C., Knapek M., Drozdenko D., Jenei P., Kim M. Y., Choe H, Máthis K., Park H., Gubicza J.: *Comparison of morphology and compressive deformation behavior of copper foams manufactured via freeze-casting and space-holder methods*. Journal of Materials Research and Technology, 15/nov-dec. (2021) 6855–6865. https://doi.org/10.1016/j.jmrt.2021.11.108.

[2] Jenei P., Kádár C., Szabó Á., Hung S. M., Kuo C. J., Choe H., Gubicza J.: *Mechanical behavior of freeze-cast Ti foams with varied porosity*. Materials Science and Engineering: A, 855. (2022) 143911. https://doi.org/10.1016/j.msea.2022.143911.

[3] Bálint A., Szlancsik A.: *Mechanical properties of iron hollow sphere reinforced metal matrix syntactic foams*. Materials Science Forum 812. (2015) 3–8. https://doi.org/10.4028/www.scientific.net/MSF.812.3.

[4] Banhart J.: *Metal foams – From fundamental research to applications [C]*. Frontiers in the Design of Materials (FDM 2005).

[5] Movahedi N., Linul E.: *Quasi-static compressive behavior of the ex-situ aluminum-alloy foam-filled tubes under elevated temperature conditions*. Materials Letters, 206. (2017) 182–184. https://doi.org/10.1016/j.matlet.2017.07.018.

[6] Linul E., Movahedi N., Marsavina L.: *The temperature effect on the axial quasi-static compressive behavior of ex-situ aluminum foam-filled tubes*. Composite Structures, 180. (2017) 709–722. https://doi.org/10.1016/j.compstruct.2017.08.034.

[7] Duarte I., Vesenjak M., Krstulović-Opara L., Ren Z.: *Static and dynamic axial crush performance of in-situ foam-filled tubes*. Composite Structures, 124. (2015) 128–139. https://doi.org/10.1016/j.compstruct.2015.01.014.

[8] Kemény A., Leveles B., Kincses D. B., Károly D.: *Manufacturing and Investigation of In Situ and Ex Situ Produced Aluminum Matrix Foam-Filled Tubes*. Advanced Engineering Materials, 24/1. (2022) 2100365:1–8. https://doi.org/10.1002/adem.202100365.

[9] Chilla V., Mondal D. P., Ram G. D. J., Mukherjee M.: *Processing of in-situ aluminium foam-filled stainless steel tube with foam-tube bonding for enhanced crashworthiness*. Journal of Manufacturing Processes, 82. (2022) 488–500. https://doi.org/10.1016/j.jmapro.2022.08.020.

[10] Taherishargh M., Vesenjak M., Belova I. V., Krstulović-Opara L., Murch G. E., Fiedler T.: *In situ manufacturing and mechanical properties of syntactic foam filled tubes*. Materials & Design, 99. (2016) 356–368. https://doi.org/10.1016/j.matdes.2016.03.077.

[11] Movahedi N., Murch G. E., Belova I. V., Fiedler T.: *Manufacturing and compressive properties of tube-filled metal syntactic foams*. Journal of Alloys and Compounds, 822. (2020) 153465. https://doi.org/10.1016/j.jallcom.2019.153465.

sciendo

Acta Materialia Transylvanica 6/1. (2023) 42–52.
DOI: Hungarian: https://doi.org/10.33923/amt-2023-01-08
English: https://doi.org/10.33924/amt-2023-01-08

ACTA MATERIALIA TRANSYLVANICA

Proof of the Elongation Reserve of Longitudinally Compressed Wood by Tensile Tests

Tamás SAJDIK,[1] Mátyás BÁDER[2*]

[1] *University of Sopron, Faculty of Wood Engineering and Creative In-dustries, Institute of Wood Technology and Technical Sciences. Sopron, Hungary, sajdiktomi@gmail.com*

[2] *University of Sopron, Faculty of Wood Engineering and Creative In-dustries, Institute of Wood Technology and Technical Sciences. Sopron, Hungary, bader.matyas@uni-sopron.hu*

Abstract

This paper deals with the proof of the theory of elongation reserve remaining in wood after compression parallel to the grain. After compression, the wood becomes much more pliable and the force required for bending is reduced. At the end of the 1-minute fixation following 20% compression, the compressive stress in the beech samples was reduced to an average of 72.3%, while the oak samples showed a 65.6% change. The remaining shortening at this time was 3-5%. At the end of the 3-hours fixation, the compressive stress had decreased to 37.1% for beech and 27.9% for oak, resulting in a residual shortening of 12-18%. An average maximum tensile force of 1.76 kN was required for untreated beech samples, which resulted in a 1.55 mm increase in size parallel to the grain. For specimens fixated for a short-time, a tensile force of 1.06 kN caused a 3.66 mm increase in size, while for specimens fixated for a long-time, a force of 0.85 kN caused an 8.79 mm increase in size. The trends were similar for oaks. The higher moisture content provided a significantly larger increase in size during the tensile tests. The existence of the elongation reserve was clearly confirmed.

Keywords*: wood compression parallel to the grain, compressive stress, tensile strength, tensile test, elongation reserve.*

1. Introduction

1.1. The anatomical structure of wood

Wood, as a natural composite, has been an important raw material for mankind since ancient times. It consists of three main components, cellulose, lignin and hemicelluloses. Before moving on to wood compression along the grain (pleating), it is important to clarify the general structure and cell structure of wood. Cells are usually made up of several cell walls; the outer wall is called the primary cell wall, while the subsequent layer is usually called the secondary cell wall, however, it is three-layered, they are distinguished by separate symbols (S1, S2, S3) (**Figure 1**).

The structure of the cells is very important from a mechanical point of view since strength is a determining factor in the fields of use of wood. The cells have an elongated structure; the cells that ensure the strength of wood are called fibers. In terms of the structure of the trunk, two large groups can be distinguished: heartwood and sapwood. The heartwood is an internal part of the trunk and does not play a role in active physiological processes. Its extractive material content is typically extremely high compared to sapwood, and the heartwood provides the appropriate strength. However, living cells are also needed around the inactive cells, which ensure the biological life of the tree. This function is performed by the sapwood, in which the vessels and tracheids serve as water and nutrient transport channels. However, it is important to mention that their structure has been discussed in general so far. The properties differ from tree to tree, but tree species can be grouped in several ways. Good examples of these are the marked differences between the hardwood groups of the ring-porous and the diffuse-porous. Thanks to these differences, the wood species can be used in several

sectors. Nowadays, wood modification is widely researched and used for a variety of purposes. Its purpose is to improve the properties of certain wood species and increase their range of use.

1.2. Assuming the existence of the elongation reserve

As a result of the treatment, pleating results in a permanent shortening of the wood. Several changes take place in the wood during the compression, and accordingly, several theories have come to light to explain the significantly improved pliability. The primary theory is that during pleating, a reserve of elongation is created in the wood by the buckling of the cell walls. In other words, the buckled cell walls are able to straighten later (first appearances: [2, 3]). This is important because the failure of the wood during bending typically occurs in the tension zone (disruption), due to its low elasticity. The aim of this research is to prove or disprove, based on the measured results and their analysis, whether there really is an elongation reserve in the wood after pleating.

1.3. The history of compression

We distinguish two large groups in terms of compressing. Compression can be done parallel to the grain or perpendicular to the grain (Figure 2). The difference between the anatomical directions is also reflected in the goals of the modifications. With compression parallel to the grain, the material will be much more flexible, while with compression perpendicular to the grain, we can increase the density, thereby making the wood much harder.

The bending of wood as a process was already used in ancient Egypt. At that time, wood was only steamed, which softened the material and made it bendable. This made it possible to change the shape more easily without breaking the material. Once set to the correct shape, cooling and drying were used to finalize the change with minimal spring-back. The method is still popularly used today, however, the steaming process is very complicated and only economical in large-scale industrial series production. Nevertheless, softening methods have also been developed, as Kollman [4] mentions in his study. There are cooking methods where the wood is treated in alum or in anhydrous liquid ammonia.

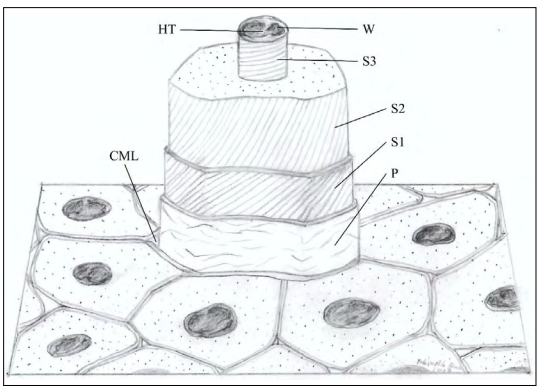

Figure 1. *Structure of the cell wall. (source: [1])*

1.4. The development of the pleating

This process was first introduced in the German Empire in 1917, which made it possible to bend wood at room temperature [5]. The method made it easier to bend the wood without much force, and had the advantage that the compressed material did not need to be reheated to achieve a high degree of bendability. An important part of the process was cooking or steaming before pleating, which softened the fibers enough to allow pleating without ruining the material. The pleated wood can be bent at any temperature. After the modification, the pleated wood was cooled, thanks to which it became further processable and could be cut into boards and other timber. Regarding the applied procedure, it can be stated that in this case it is a thermo-hydromechanical modification.

In 1917, an another patent was published in the German Empire, which further developed the previous patent for large-scale production [6]. In this development, the fixing time (the period during which the compressed wood is held in a compressed state) was to be triggered by means of a clamping device. Normally, after pressing, the material is left to fix inside the machine, which further strengthens the changes in properties caused by compression, but in this case the machine cannot be used for further compression.

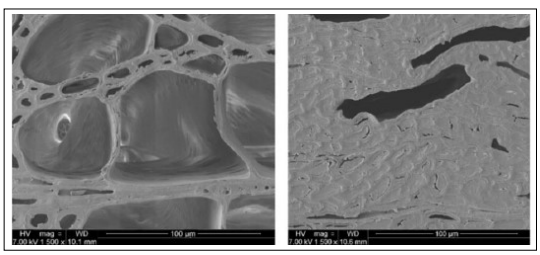

Figure 2. *Microscopic image of beech wood before and after perpendicular compression to the grain direction (source: [3])*

With the help of the developed device, the material could be taken out of the machine in a fixed state, ensuring permanent fixation, and then cooled. Meanwhile, the machine could already start compressing the next piece of wood. Unfortunately, the operation was so complex that the technology and production processes of the time did not allow its spread in the wood industry. This type was further developed in 1926 [7]. Holzveredelung GmbH created a machine based on Hanemann's preliminary patents, and it could already be successfully integrated into the industrial processes of the time and production became realistically feasible. An internal insert was developed, thanks to which the wood could be taken out of the machine immediately after pressing and kept it in a fixated state. In the meantime, it was already possible to refill the compression device with the new wood (**Figure 3**). In the decades that have passed since then, experts have initiated and implemented numerous developments, so that since the 1990s, PLC-controlled compression equipment has been available.

Pleating has been possible at the University of Sopron since 2015. Measurements and compression force are provided by an Instron 4208 universal material testing machine (Instron Corporation, USA). The compression process itself takes place in a machine unit specially developed for this purpose, which is described in subsection 2.2. The machine provides the possibility to compress 20×20×200 and 20×30×200 mm specimens pleating. Its maximum compression capability allows the tested material to be compressed to a ratio up to 33% smaller than its original length in the grain direction. Heating is built into the side walls ensuring the right temperature, and the side plates can move together with the wood being compressed in order to achieve the right compression ratio [8, 9].

The great advantage of pleating wood is that it is very economical in terms of raw material use. Curved furniture elements are mostly made of glued or glued-laminated elements, which require a lot of glue and wood. On the other hand, wood compressed along the grain provides a cost-effective solution.

Pleated wood is extremely versatile in terms of areas of application. As already mentioned, it can be perfectly used for creating curved furniture elements, as well as for vibration-damped tool handles, curved picture frames, car interior coverings, sports equipment, in the toy industry and musical instruments [3, 4, 10].

For pleated wood, production oversizing can be avoided, since even the finished form can be bent without breaking, in addition to all this, the direction of the grain follows the shape throughout, there are no fibers running out to the side. However, the disadvantage of the process is that discoloration due to steaming has to be taken into account. Thus, it is necessary to choose where it should be used aesthetically.

1.5. Tömörítésre alkalmas fafajok

Based on preliminary studies and research, it can be stated that a wide range of wood species can be used for compression. There is a large selection of hardwood species, most of them are especially suitable for compression, for example beech (*Fagus sylvatica* v. *Fagus* ssp.), oak (*Quercus* ssp., *Quercus petraea, Quercus velutina*), black cherry (*Prumus serotina*), ash (*Fraximus excelsior, Fraximus americana*), and silver maple (*Acer saccharinum*) and pear wood, too [4]. Differences can be read in various literature when we are interested in robinia, poplar or linden. The compression properties of these wood species are doubtful.

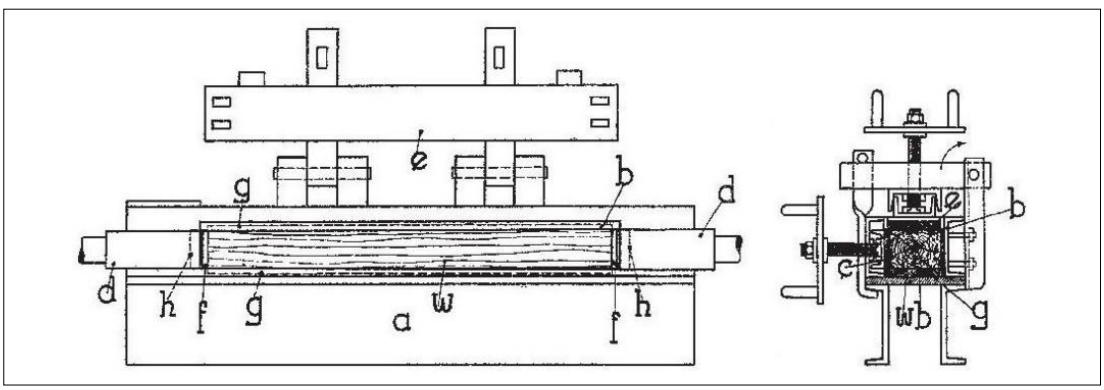

Figure 3. *The first compressing machine produced for industrial use. (source:* [7]*)*

In order for the wood to be pleated without problems, special attention must be paid to the quality of the material to be used. Only the knot-free, narrow annual-ring wood of a straight-growing tree can be used for compression. The direction of the fibers of the material must be parallel to the longitudinal edges of the workpiece, which means that a maximum deviation of 7° can be accepted. The quality of the material itself is much more important for compression than the method by which it was cut from the log, in this case this aspect is negligible information [11]. For wood prone to false grain, special attention must be paid to the fact that the wood to be used must not contain false heartwood, as it has different mechanical properties and would impair the final result. From the point of view of knots, large knots are to be avoided, however, pin knots are allowed on the surface, but these are not very desirable either, since these points absorb the greatest stress, which means that in the case of tensile tests, possible failure will take place on these weakened cross-sections. When designing the specimens, it is also important to take into account the shape factor, because the cross-section of the material changes as a result of steaming and cooking. This is due to changes in moisture content. It is also possible to compress bundled specimens. However, it is important that only one wood species can be compressed in a bundle, and their placement in the machine is only possible if they behave as one material.

In the cellular structure of wood, we distinguish between two types of water, free water and bound water. The free water is found inside the cells, in the cell lumina, while the bound water tends to settle on the walls of the cells. Fiber saturation point (FSP) is the state when there is no free water in the cell lumina, but the bound water accumulates in the largest possible amount on the walls of the cells. The fiber saturation point is different for each wood species, for beech it is 35.6%, while for oak it is 24.5% [12]. If we average the different FSPs of the wood species, we would get roughly 30%. Thanks to this value, it is also used in practice for large amounts of wood. For compression, mostly green wood is suitable, but with a moisture content of at least 16% [13]. . According to other literature, the moisture content of the wood suitable for compression is 2-8% less than the *FSP* [14].

2. Materials and methods, description of technology processes

2.1. Fiber softening process

The modification process consists of three important parts: fiber softening, compression itself and post-treatments. Thanks to the hollow cell structure of the wood, compression can be carried out non-destructively, however, since the untreated material is very stiff, it must always be steamed/cooked beforehand in order to make it easier to form and to soften the fibers. From a chemical point of view, hemicelluloses and lignin change under the influence of the right amount of heat and moisture, which allows the mechanical properties of wood to decrease, like the modulus of elasticity. The cellulose fibers form a rigid structure in the cell wall, however, under the influence of heat and moisture, the matrix material consisting mainly of lignin and hemicelluloses softens [15], and the cells can slide over each other during compression and bending. During steaming, wood begins to decompose at approximately 100 °C. Initially, damage to the hemicelluloses is observed, due to which the resistance of the wood to pressure decreases, in other words this condition is particularly advantageous for compression in the direction of the grain. According to specialist literature, the reference value for overheating of wood is 2 min/mm [16, 17], taking this value into account, the appropriate steaming time must be defined depending on the cross-section to be compressed.

Overall, it can be stated that before compression, the wood must always be steamed at a temperature between 80-100 °C for better pliability, so that the level of fiber softening will be adequate to start compression (Figure 4).

Figure 4. *The vessel used for steaming the specimens.*

2.2. Application of Instron 4208 material testing machine for pleating

As previously mentioned, fiber compression has been possible at the University of Sopron since 2015. In order to apply the technology, a machine (Instron 4208) capable of exerting a suitable amount of force was needed, as well as a compression unit that could be connected to the machine (**Figure 5**).

The construction of the compression unit is simple and performs its function perfectly. It consists of two main parts. From a rigid-walled compression chamber, the inner side walls of which can move with the compressed material, and from a heated outer side wall, which ensures the right temperature for the duration of compression (**Figure 6**).

The settings of the compression program were suitable for all specimens, we only changed one parameter, the fixation time. The size of the fixation time largely determines the degree of change in the material properties, the longer the fixation time causes a greater permanent shortening and, with this, the elongation reserve probably also increases.

In the course of the research, we examined two tree species, beech (*Fagus sylvatica*) and sessile oak (*Quercus petraea*), and two fixation times were used for each tree species, a fixation time of one minute (fixated for a short time) and 3 hours (fixated for a long time), respectively. According to this, we could separate four groups of compressed specimens in addition to the untreated ones.

2.3. Pleating

Once the fiber softening process is complete, the pleating can begin. The object to be compressed is placed in the compression chamber, where the specimens are using high pressure, in which case a size reduction of up to 33% can be achieved without destroying the material. It is important to mention that the maximum compression value of 33% is determined by the laboratory compression equipment we use. Every type of wood has a compressibility limit, beyond which the material undergoes substantial structural destruction, so it breaks down and will not be suitable for casting. Based on previous, unpublished research, for example, the highest compressibility ratio before failure in oak is 21-23%, while in the case of beech it can reach up to 30%. During our tests, the compression was carried out with a 20% decrease in size in the fiber direction for all specimen groups, thereby guaranteeing adequate compression without significant structural damage. The relative compression rate was 25%/min **[1]**.

When the appropriate pressing ratio is reached, fixation can begin, where its internal stresses de-

Figure 5. *Compression unit close up.*

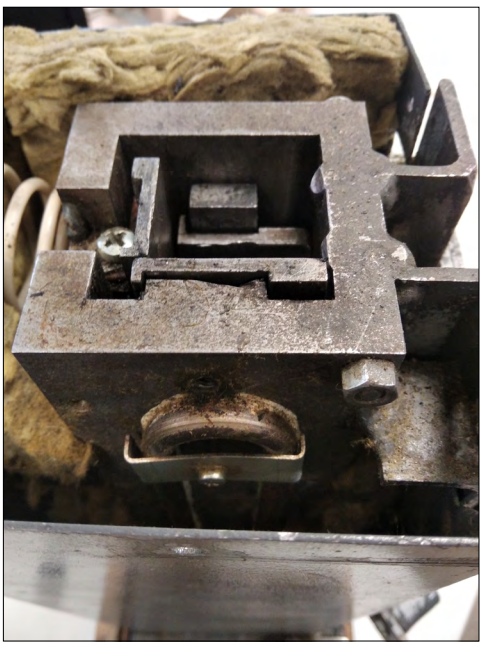

Figure 6. *The internal structure of compression unit.*

crease and its permanent shortening and bendability increase. It is important to mention that the longer the fixing is done, the less the material will bounce back.

2.4. Post-treatment of pleated wood

Once the test pieces are removed from the compression chamber, post-treatment processes can begin. Since it has to be steamed before compression, it has a high moisture content after the process is finished, so the next step is the drying, as a post-treatment. Several methods can be used for drying, the choice of which depends on the specific area of use of wood. However, it is important to mention that the flexibility of the wood deteriorates rapidly during drying. At a moisture content of 0-5%, it often happens that wood compressed in the grain direction is more brittle than untreated wood. Overall, it can be concluded that drying, as a post-treatment process, serves as a final operation. The compressed material is bent into the desired shape, and then this change in shape is finalized by drying. However, it is important that the bent material must be dried attached to the bending template, so that there will certainly be no deviations in shape after the process is finished. Previous studies have shown [9], that the bendability of pleated wood is greatest when it is close to fiber saturation point.

The bendability of the compressed material can be preserved, but this requires a suitable moisture content. This means that, subject to the appropriate climatic conditions, it is not important to use the pleated wood immediately, but it can be perfectly stored, thus facilitating the mass production of factories with a large consumption of material.

2.5. The process of forming the tensile samples

During the process, we compressed 20×30×200 mm specimens (Figure 7), but they were still too large to be subjected to tensile tests.

Each large specimen was sliced into small test specimens 2 mm thick (2×20×160–200 mm depending on the treatment), it was usually possible to create 4 small samples from one large specimen, also taking into account the width of the cutting gap (Figure 8).

The sliced samples were routed to a standardized profile using a plunge router machine, which were already suitable for carrying out the tensile tests (Figure 9). The tested part was 2×8×50 mm for each tensile sample.

Figure 7. *20×30×200 mm beech specimen.*

Figure 8. *Thin specimens cut from larger beech specimens in order of compressed and fixated for a long time, fixated for a short time and untreated.*

Figure 9. *Fixated for a long time, fixated for a short time and untreated small samples in sequence, with a profile designed for tensile testing.*

In Figure 8 the specimen on the left is clearly curved, so the profile was designed in line with the original shape. During the three-hour fixated pleating, most of the large specimens were bent after being removed from the compression equipment. As we mentioned also in subsection 1.5, it is important that all fibers are located parallel in the specimen, in order to preserve parallelism, the design of the tensile sample must be adjusted to the curvature of the material, so there will be no fiber run-out, which can lead to incorrect measurements in the tensile test.

For both beech and oak, a total of three specimen groups were created. We examined the mechanical properties of wood specimens fixated for a long time, fixated for a short time and untreated. The three main specimen groups underwent different pre-treatments, the purpose of which was to be able to carry out a wider range of tests.

During the first type of pre-treatment, the samples were conditioned to a moisture content of 12% at a temperature of 20 °C at a humidity of 65% (normal conditions). In the second type of pre-treatment, the samples were first dried to 0% moisture content and then climatized under normal conditions. In the third type of pre-treatment, the samples were stored in wet state close to green moisture content, which was achieved by freezing so that the water formed solid molecules in the wood, thereby disabling evaporation and the appearance of biotic pesticides. We examined an average of 40 tensile samples per specimen group, in other words the data of a total of 240 samples were processed.

2.6. Tensile tests

After the design of the samples and the compilation of the specimen groups was completed, the specimens were subjected to tensile tests. We used a Tinius Olsen H10KT (Tinius Olsen Ltd. Redhill, England) material testing machine to carry out the tests. The lower grip has a fixed position, while the upper grip can move in the direction of the „z” coordinate (Figure 10).

Since the strength and elongation of the fixated for a long time, fixated for a short time and untreated specimens were significantly different, we chose a different tension rate for each group of specimens. Our aim was for all samples to fail in a uniform time interval as defined by the associated test standards (ISO 13061-6:2014 [18]) Considering the failure times, the correct rate was 3 mm/s for untreated samples, 4 mm/s for fixated for a short time samples, and 8 mm/s for fixated for a long time samples.

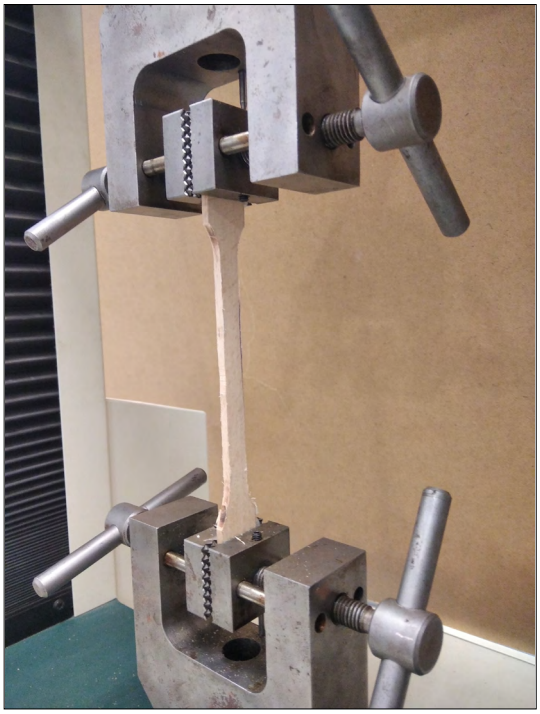

Figure 10. *Clamping a tensile sample into the material testing machine.*

3. Results and evaluation

3.1. The changes in compressive stress due to fixation

During compression along the grain, wood is in plasticized state, thus preventing its destruction. Achieving a compression ratio of 20% requires significant force, which all of our samples withstood without damage. In the moment when the compression ratio of 20% was reached, the actual compression force divided by the cross-section gave the highest compression stress. Keeping the 20% compression ratio at a constant value (fixation), the compression stress initially quickly decreases and then the decrease gradually slows, as is typical for the stress relaxation of viscoelastic materials.

The beech and oak specimens reacted differently to the compression. As shown in Figure 11 after 20% compression, the compressive stress of the beech specimens decreased to 72.3% after 1 minute of fixation, while the same was 65.6% for the oak specimens. Long fixation (compressed for 3 hours) reduced the compressive stress to 37.1% for beech and 27.9% for oak. It should be noted that the significant difference is also a

consequence of cooling to room temperature. At the same time, the structure of the specimens changed significantly as a result of both compression and fixation for a long time, as has already been demonstrated by numerous microscopic analyses [9]. Analyzing the permanent shortening values, it can be said that in all cases the oaks suffered a greater permanent deformation than the beeches. After 20% compression and short fixation, the shape change was 3-5%, while long-term fixation resulted in a permanent shortening of the specimens of 12-18%. These are very significant changes, which are coupled with serious changes of the anatomical-physical-mechanical properties. This is reported in Figure 11, which shows both the averages of the maximum compressive stresses and the averages of the compressive stresses measured at the end of the fixations. In general, it can be said that a third of the compressive stress created during compression is removed during one-minute fixation, while a three-hour fixation reduces the compressive stress significantly more, by two-thirds.

3.2. Relationships between the degree of rebound and the magnitude of the exerted force

For specimens conditioned to 12% moisture content at 20 °C temperature and 65% relative humidity (normal condition), it can be observed for both wood species that the tensile forces are opposite to the size changes along the grain, as can be seen in Figures 12. and 13. The tensile force applied to the untreated beech samples was 1.76 kN on average until the moment of rupture with an average increase in length along the grain of 1.55 mm. For the samples fixated for a short time a smaller force was required, on average 1.06 kN, to achieve an average 3.66 mm increase in length in the fiber direction, however, the most spectacular results were obtained for the samples fixated for a long time. An average force of just 0.85 kN was enough to increase the length by averagely 8.79 mm. This means that the magnitude of the tensile force changes opposite to the fixation time for a given amount of elongation. For specimens fixated for a long time, which were under continuous pressure for 3 hours, we can achieve greater increase in fiber direction with much less force. This finding was also true for all other samples during the measurements.

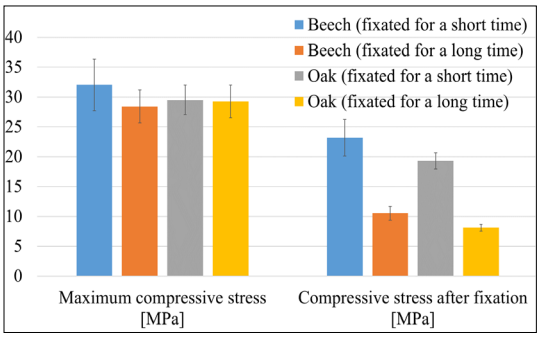

Figure 11. *Compressive stresses after pleating and after different times of fixation.*

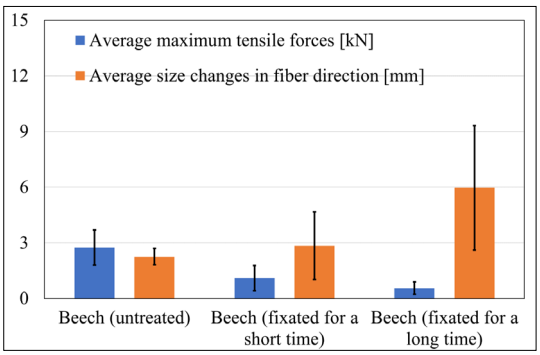

Figure 12. *Correlations of tensile tests of beech wood.*

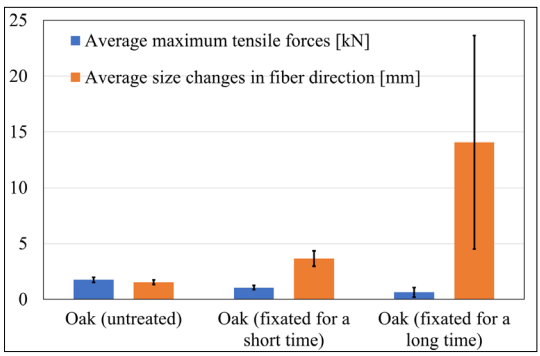

Figure 13. *Correlations of tensile tests of oak wood.*

3.3. Dimension changes depending on the fixation time

For both tree species, the length of the specimens differs depending on the treatment (untreated, fixated for a short time and fixated for a long time groups). It can be perfectly demonstrated that fixation for a long time is the most effective procedure in terms of the ability to change

the size in the grain direction, as can be seen in Figures 14. and 15. This is in line with the finding of Báder and Németh [19] according to the deflection of the compressed samples by 20% during a 4-point bending test: these samples have 3-4 times higher pliability compared to the untreated ones, while the fixated for a long time can withstand at least a six-fold deflection.

3.4. The influence of moisture content on the dimension changes during the tensile tests

Figures 16 and 17 summarize the averages of the dimension changes parallel to the grain for all three sample groups and for both wood species. It is perfectly visible that in almost all cases the samples with the highest moisture content had the largest deformation during the tensile tests. This finding also supports the results of previous research [9], that the bendability/elongability of wood is greatest when it is in a state close to fiber saturation point. The other sample groups contained much less water than these sample groups, so it was closest to the fiber saturation point.

3.5. Relationship of specimen groups close to the green state

Interestingly, a lot of similarities can be observed between the length change along the fibers - tensile force graphs of both wood species in Figures 18 and 19. The graphs of the untreated specimens slope sharply upwards, thus, a large force is necessary to achieve a small length change. For the specimens fixated for a short time significantly less force is needed for the same length change along the fibers and the maximum length change is greater, compared to the untreated specimens. Finally, the graphs of the specimens fixated for a long time show the most spectacular deviation, since here, thanks to the large-scale changes in cell structure [19] the largest maximum length change can be achieved with relatively low maximum force compared to the untreated specimens.

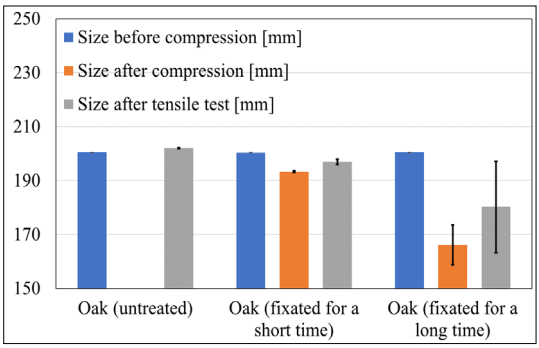

Figure 14. *Average size of oak samples parallel to the fibers in the different phases of the test.*

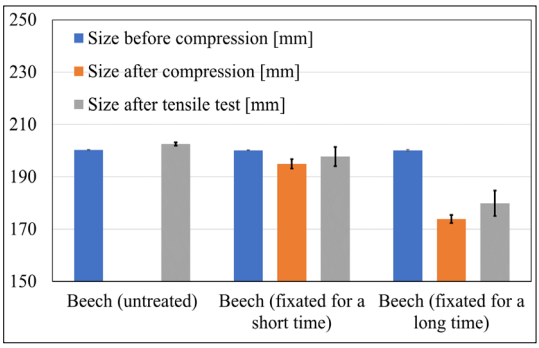

Figure 15. *Average size of beech samples parallel to the fibers in the different phases of the test.*

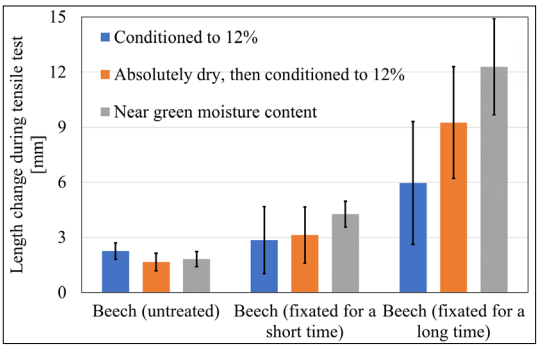

Figure 16. *Average length change of beech samples during tensile tests at different moisture contents.*

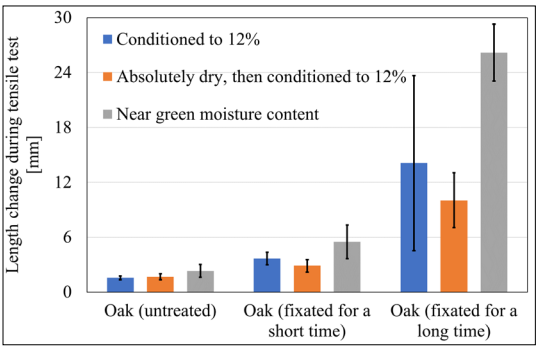

Figure 17. *Average length change of oak samples during tensile tests at different moisture contents.*

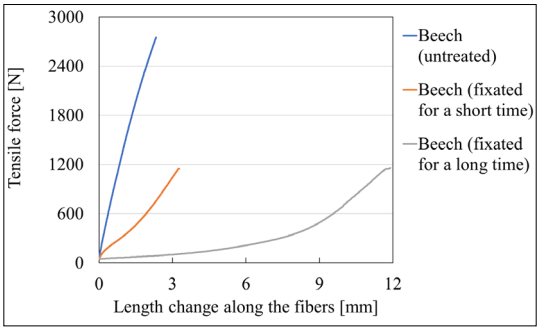

Figure 18. *Force - length change graphs for representative specimens of all three beech sample groups with near green moisture content.*

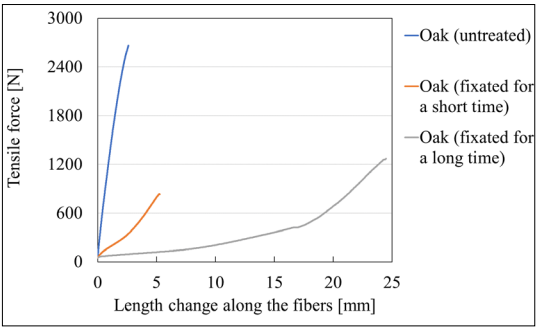

Figure 19. *Force - length change graphs for representative specimens of all three oak sample groups with near green moisture content.*

4. Conclusions

The aim of the study is to prove the theory of the elongation reserve of the pleated wood, as well as to examine and compare the mechanical effects of the various changes in material structure associated with the modification process with the mechanical properties of untreated wood.

The data and diagrams illustrated above serve as proof of the existence of the elongation reserve. The knowledge of this can serve as an important factor in further research on pleating, as well as in the application of pleated wood in the furniture industry, where curved elements can be made. By taking into account the elongation reserve, the change in dimensions and flexibility of the compressed material can be calculated more precisely, which will facilitate the production of curved elements in the future.

During the tests, we not only found evidence for the existence of the elongation reserve, but also found a clear explanation for the findings of previous tests: the significant increase in the pliability of wood compressed along the grain is the result of the improvement of the ability to increase in size along the grain. In addition, we proved that the ability of the specimens to increase in size along the grain is significantly higher at a moisture content close to the fiber saturation point than at a moisture content of 12%.

In the future, we will expand the number of tested sample groups, which will be subjected to other pre-treatments before the tensile tests, such samples with a moisture content of 20-25% and samples dried artificially.

Acknowledgement

Supported by the ÚNKP-22-1-I-SOE-76 New National Excellence Program of the Ministry for Culture and Innovation from the source of the National Research, Development and Innovation fund.

References

[1] Báder M.: *A természetes faanyag tulajdonságainak módosítása termo-hidromechanikus és vegyi eljárásokkal.* Doktori értekezés, Soproni Egyetem, Sopron, 2021. 1–138.

[2] Hanemann M.: *Processes for making wood everlastingly flexible*. US Patent Office No. 1 457 974, USA, 1920.

[3] Vorreiter L.: *Holztechnologisches Handbuch.* Band I. Georg Fromme & Co., Wien, 1949. 1–548.

[4] Kollmann F. F. P.: *Technologie des Holzes und der Holzwerkstoffe II.* Springer-Verlag, München, 1955. 1–1183.

[5] Hanemann M.: *Holzaufbereitungsverfahren*. Deutsches Reich Reichspatentamt No. 318197, Germany, 1917.

[6] Hanemann M.: *Holzaufbereitungsverfahren – Zusatz zum Patent 318197*. Deutsches Reich Reichspatentamt No. 321629, Németország, 1917.

[7] Holzveredelung Ltd.: *Verfahren und Vorrichtung zur Herstellung von weichbiegsamen Holz*. Deutsches Reich Reichspatentamt, No. 458923, Germany, 1926.

[8] Báder M., Németh R.: *Faanyagok rostirányú tömörítésének kísérleti körülményei – 1. rész.* Gradus, 4/2. (2017) 403–411.

[9] Báder M., Németh R.: *Moisture-dependent mechanical properties of longitudinally compressed wood.* European Journal of Wood and Wood Products, 77. (2019) 1009–1019. https://doi.org/10.1007/s00107-019-01448-1

[10] Báder M., Németh R., Ábrahám J.: *Faanyag rostirányú tömörítésével kapcsolatos elméleti és gyakorlati kérdések áttekintése – 2. rész: Történelem és szabadalmak. A tömörítési folyamat tulajdonságai és a tömörítést követő eljárások*. Faipar, 63/1. (2015) 10–20.

[11] Szabó I.: *Fahajlítás*. In: *Faipari kézikönyv II.* (ed.: Molnárné P. P.). Faipari Tudományos Alapítvány, Sopron, 2002. 60–61.

[12] Molnár S.: *Faanyagismeret*. Mezőgazdasági Szaktudás Kiadó, Budapest, 1999. 1–469.
[13] Buchter J., Adelhoej J., Ljoerring J., Hansen O.: *Introducing Compressed Wood*. Danish Technological Institute, Department of Wood and Furniture, Taastrup, 1993. 1–32.
[14] Kuzsella L.: *Rostirányú tömörítés hatása a bükk faanyag szerkezetére és mechanikai tulajdonságaira.* Doktori értekezés, Miskolci Egyetem, Miskolc, 2011. 1–151.
[15] Winkler A.: *Farostlemezek*. Mezőgazdasági Szaktudás Kiadó, Budapest, 1999. 1–172.
[16] Stevens W. C., Turner N.: *Solid and laminated wood bending*. His Majesty's Stationery Office, London, 1948. 1–100.
[17] Peres M. L., Gatto D. A., Delucis R. A., Beltrame R.: *Vergamento madeira sólida: quallade de processo e matéria-prima*. Nativa-Agricultural and Environmental Research, 1. (2013) 56–61.
[18] ISO 13061-6: Physical and mechanical properties of wood - Test methods for small clear wood specimens - Part 6: Determination of ultimate tensile stress parallel to grain. 2014.
[19] Báder M., Németh R.: *The effect of the relaxation time on the mechanical properties of longitudinally compressed wood.* Wood Research, 63/3. (2018) 383–398.

sciendo

Acta Materialia Transylvanica 6/1. (2023) 53–58.
DOI: Hungarian: https://doi.org/10.33923/amt-2023-01-09
English: https://doi.org/10.33924/amt-2023-01-09

ACTA MATERIALIA TRANSYLVANICA

Investigation of Welding Forces and Weld Strength for Friction Stir Welding of Acrylonitrile-Butadiene-Styrene (ABS) Plates

Róbert Gábor STADLER,[1] Richárd HORVÁTH[2]

[1] *Óbuda University, Bánki Donát Faculty of Mechanical and Safety Engineering. Doctoral School on Materials Sciences and Technologies, Budapest, Hungary, stadler.robert@bgk.uni-obuda.hu*

[2] *Óbuda University, Bánki Donát Faculty of Mechanical and Safety Engineering, Budapest, Hungary, horvath.richard@bgk.uni-obuda.hu*

Abstract

The purpose of this study is to investigate the applicability of the friction stir welding technology to acrylonitrile butadiene styrene (ABS) type polymer and the effect of welding parameters on the force values and weld strength during he-welding. The tests were carried out on 4 mm thick ABS sheets using a conventional mould design. The input parameters (speed – n, feed rate – v_f) were varied in 3-3 steps and a complete set of experiments was performed. From the force measurements, it was concluded that the force values in the feed direction (F_y) and axial direction (F_z) are the dominant force values during welding. The force components decrease with increasing speed and n/v_f ratio, while they increase with increasing feed rate. The tensile strength of the weld improves with increasing speed and n/v_f ratio, while they deteriorate with increasing feed rate. The best weld strength (10.69 MPa) was measured at 1000 rpm and 50 mm/min feed rate.

Keywords*: friction Stir Welding, ABS, welding force, joint efficiency.*

1. Introduction

Friction stir welding (FSW) is a welding process based on the principle of mechanical friction, patented in the early 1990s [1]. The process has become particularly successful and popular, for example in the case of aluminium. It is used in industries such as the aerospace industry [2, 3, 4]. For the time being, it is only used with aluminium at an industrial level, but there are already publications on welding experiments of magnesium [5], titanium [6] and copper [7]. Friction stir welding is not only investigated for welding metallic materials. There are several studies on the friction stir welding of various polymers and fibre-reinforced thermoplastics [8] One of the greatest advantages of the technology is that it is also suitable for welding fibre-reinforced thermoplastics [9]. In addition, friction stir welding is energy-efficient and environmentally friendly, because neither auxiliary materials nor shielding gas is needed [10].

In friction stir welding, a rotating tool with a special shoulder and pin geometry moves between the workpieces which are in contact and to be welded together. Friction between the workpiece and the rotating tool produces the temperature required for welding. Also, the tool mixes and circulates the melted material in the welding zone, thus ensuring an even and uniform seam. The tool used during welding is sunk into the materials to be welded to a depth approaching the thickness of the workpieces to be welded. After the tool reaches the end of the welding path, it is lifted out of the welding zone. **Figure 1** shows a schematic diagram of friction stir welding, as well as the force components during welding.

ABS is one of the most common thermoplastics, which can be found in large quantities in vehicles or very often in various household appliances. This is because it can be easily processed, is stiff and is scratch resistant and durable [11].

In recent years, many publications have focused on the friction stir welding of ABS.

Arvin et al. [12] studied the friction stir welding of ABS sheets using a special tool with a heated shoulder. The diameter of the tool was 10 mm and

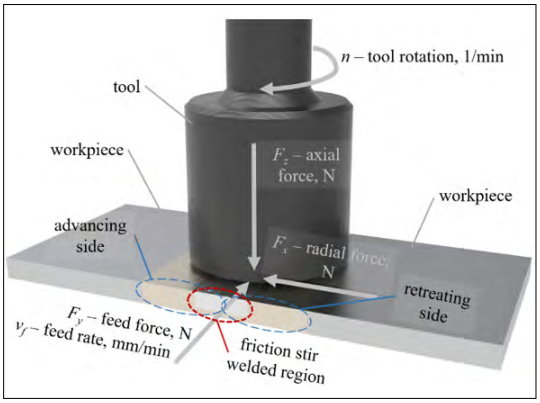

Figure 1. *Schematic diagram of friction stir welding.*

the pin was threaded. The shoulder was equipped with an electric heater, which was used to control the temperature of the shoulder. During their tests, they varied 3 parameters (tool rotational speed, feed and the initial temperature of the tool) at 3 levels. They used a complete design of experiments, therefore they carried out experiments at 27 measurement points. The output parameters were the tensile strength of the seam and bonding efficiency (the ratio of the tensile strength of the seam and the bulk material). They analysed their measurement results by analysis of variance (ANOVA) and the response surface method (RSM). The authors concluded that the tensile strength of the seam increases with increasing rotational speed and tool temperature, while with increasing feed, it decreases. The best welding efficiency (88% of that of the raw material) was achieved with a rotational speed of 1600 1/min, a feed of 20 mm/min and a tool temperature of 100 °C.

Sadeghian and Givi [13] studied the friction stir welding of 8 mm thick ABS sheets, using tools with cylindrical and conical pin geometries. The shoulder had a standing design, but was not heated. Among the input parameters, rotational speed, feed, as well as the inclination angle of the tool, the diameter of the shoulder and the pin, and the ratio of these diameters were changed at 3 levels. Here again, the output parameters were the tensile strength of the seam and bonding efficiency. From their measurement results, the authors concluded that the conical pin geometry, larger tool inclination angle and diameter ratio, as well as a low feed improve tensile strength.

Mendes et al. [14] studied the friction stir welding of ABS using a robotic system. In their study, they used a heated, standing shoulder tool design. The welding parameters examined were rotational speed, feed and the axial forces. After welding, they examined the strength and hardness of the seam. The authors concluded that high-quality seams can be achieved with robot-assisted friction stir welding; the high axial force promotes the compression of the polymer in the molten state, and rotational speed is responsible for heat production, which increases the strength of the seam.

Examining the welding of different polymer materials to each other is also an increasingly researched topic these days [15].

Gao et al. [16] investigated the weldability of ABS and high-density polyethylene (HDPE) sheets by stir friction welding. In addition to these two materials, the authors introduced carbon nanotubes into the joint to strengthen the seam. The tool had a pin with a tapered thread. In the study, the thickness of the welded plates was 4 mm, during welding, the two materials were placed overlapping each other, where the lower material was always ABS. The tool had a tapered thread pin geometry. The input parameters were rotational speed, feed and tool (welding) depth. These parameters were varied at 3 levels. They analysed the effect of changes in process parameters on the strength and microstructure of the seam. They achieved the best seam tensile strength (14.7 MPa) with a feed of 30 mm/min, a rotational speed of 2500 1/min and an immersion depth of 0.2 mm. They also point out that a lower feed rate increases mixing time, which ensures better mixing in the welding zone, while increasing the speed results in more heat.

Hajideh et al. [17] also investigated the friction stir welding of ABS and polypropylene (PP). At some measurement points, they introduced copper powder into the welding zone to investigate its effect on the strength and hardness of the weld. The tool was a heated, standing shoulder design, and the pin was threaded. The input parameters (rotational speed, feed and tool temperature) were varied at 3 levels. A complete experimental plan was used. The output parameters were the strength and hardness of the seam. The results indicated that copper powder significantly increases the strength and hardness of the weld.

In this study, we investigate the friction stir welding of 4 mm thick ABS plates. We examine the force components occurring during the welding process and the strength of the seams as a function of the input parameters.

2. Materials and methods

During the experiments, 4 mm thick DOCA-ABS R (Quattroplast Kft., Budapest, Hungary) plates were welded together. The welded specimens were 90 mm x 85 mm so that we could cut three 3 standard tensile test specimens from them. **Figure 2** shows the cutting and numbering of the test specimens.

The welding experiments were performed on a MAZAK Nexus VCN 410A-II type CNC milling machine. The force components occurring during welding (F_x, F_y, F_z – **Figure 1**) were measured with a Kistler9257B piezoelectric force meter clamped under the machine vice. The range of the dynamometer was $F_x = F_y = -5...+5$ kN and $F_z = 5...10$ kN **[18]**.

Using the three measured force components, we calculated the resulting force during welding as follows:

$$F_e = \sqrt{F_x^2 + F_y^2 + F_z^2} \quad (1)$$

The tensile testing of the 3 tensile specimens per measurement point was performed on a Zwick Z005 universal testing machine at a cross-head speed of 10 mm/min. In addition to the strength of the seam, the tensile strength of the bulk material was also determined based on 3 tests (29 MPa). We used this value when determining welding efficiency as follows:

$$JE = \frac{\sigma_{\max,welded\_specimen}}{\sigma_{base\_material}} \quad (2)$$

The pin geometry of the tool used during the welding tests was a cylinder. The diameter of the pin is 12 mm, the diameter of the shoulder is 29 mm, and the material of the tool is C45 steel. The welding tool used is shown in **Figure 3**.

Two of the welding parameters, tool rotational speed and feed, were changed at 3 levels. We determined the parameters used based on preliminary experiments (**Table 1**).

We used a complete experimental design. **Table 2** shows the measurement points and their welding parameters. The table also shows the value of the n/vf ratio for each measurement point. During the evaluation of the results, we also examined the results as a function of this parameter.

Table 1. *The welding parameters*

Parameters		Levels		
		–1	0	1
x_1	rotational speed – n, 1/min	500	750	1000
x_2	feed – v_f, mm/min	50	75	100

Table 2. *The measurement points and their welding parameters*

Measurement point	n [1/min]	v_f [mm/min]	n/v_f
1	500	50	10
2	500	75	6.67
3	500	100	5
4	750	50	15
5	750	75	10
6	750	100	7.5
7	1000	50	20
8	1000	75	13.3
9	1000	100	10

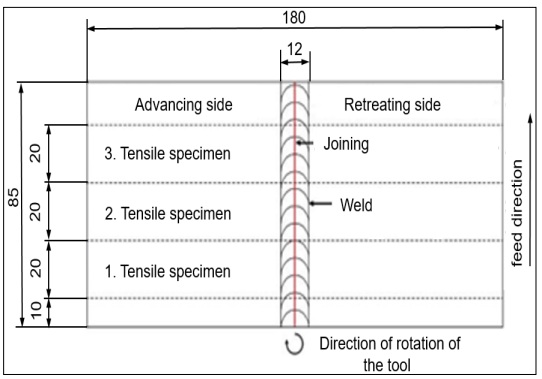

Figure 2. *Numbering of the tensile test specimens on the welded specimens (dimensions in mm).*

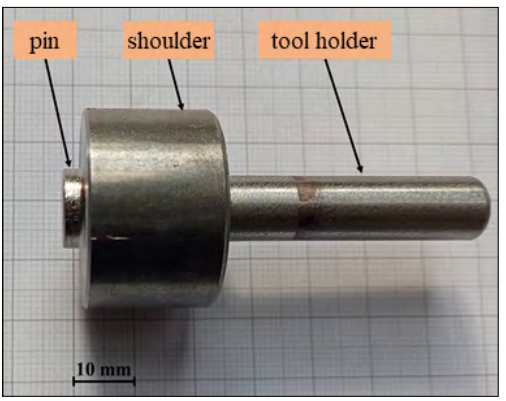

Figure 3. *The tool used in the experiments.*

3. Results

3.1. Analysis of forces

Figure 4 shows the force components during welding (F_x, F_y, F_z). No significant lateral force occurs during welding (F_y) the dominant forces are the force in the feed direction (F_z) For the latter force component, the force diagram can be divided into two significant sections. An increasing section, where the force suddenly jumps as a result of the tool entering the welding zone, and the subsequent, almost constant section. The force in the feed direction (F_y) remains nearly constant throughout the welding process.

During the evaluation of the forces, we always evaluated the average force measured in the constant section.

3.2. Results of the examination of forces

During the analysis of forces, we examined the force in the feed direction (F_y), the force components in the axial direction (F_z), and the resulting welding force (F_r). Figure 5 shows the effect of the force in the F_y direction as a function of the welding parameters. The force values decrease as rotational speed increases, while they increase as feed increases. In addition, increasing the n/v_f ratio decreases the force.

Figure 6. shows the main effect plots for the force in the F_z direction as a function of the welding parameters. Similar trends can be observed in this case as well. The value of the force component decreases with increasing speed and n/v_f ratio, while it increases with increasing feed.

Finally Figure 7 shows the main effect plots of the resultant force (F_r) Since this force comes from the two forces presented above and the lateral force component, the trends here are also similar. As the speed and the n/vf ratio increase, the resultant welding force decreases, while it increases as feed increases.

The dominant forces and the resulting welding force indicate that the temperature in the welding zone increases with increasing rotational speed, as a result of which the polymer can melt, thus the forces during welding are lower. Feed has a similar effect to welding time: the higher it is, the less time the tool stays in the welding zone, therefore it has less time to properly melt the material, and so the forces during welding increase.

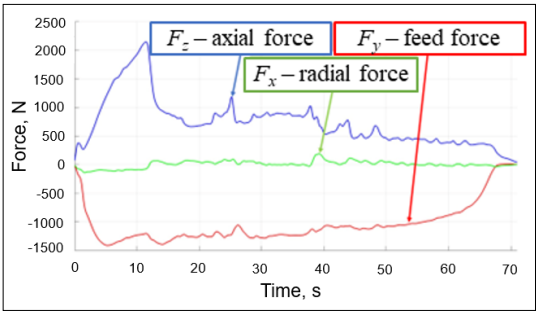

Figure 4. *The force components during welding.*

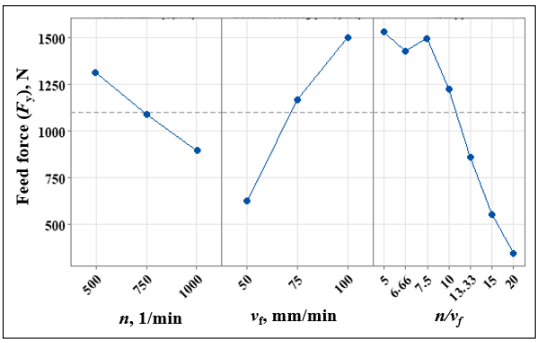

Figure 5. *The effect of welding parameters on the force in the feed direction (F_y).*

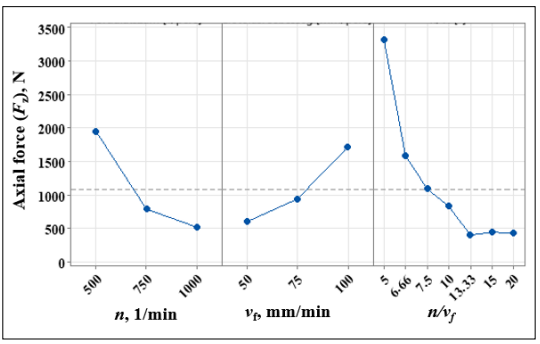

Figure 6. *The effect of welding parameters on axial force (F_z).*

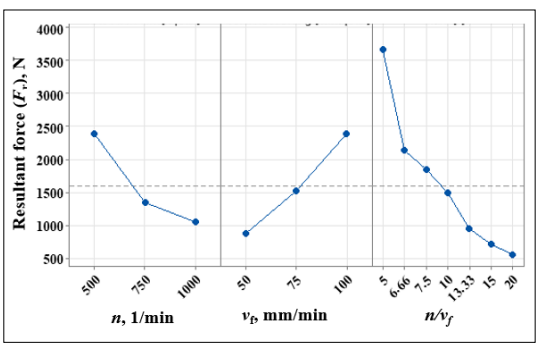

Figure 7. *The effect of welding parameters on the resulting welding force (F_r).*

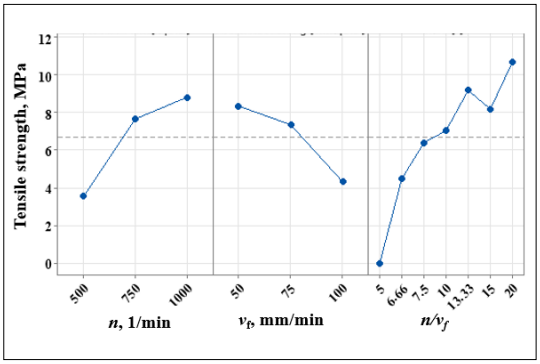

Figure 8. *The effect of welding parameters on the tensile strength of the seams.*

3.3. Tensile test results

The other output is the tensile strength of the seams. We performed 3 tests at each measurement point and calculated the average of the 3 test results. **Figure 8** shows the main effect plots of the tensile strength of the seams.

The strength of the seam tends to improve as the speed and the n/v_f ratio increase. In the case of a too small n/v_f ratio (measurement point 3, $n/v_f = 5$) no detectable bond was created between the two plates. Increasing the feed rate results in worsening seam stiffness. The best seam strength (10.69 MPa) was obtained at measurement point 7, with a rotational speed of 1000 1/min and a feed of 50 mm/min.

4. Conclusions

In this paper, we performed the friction stir welding testing of 4 mm thick ABS plates with a conventionally designed tool. During the tests, we changed the rotational speed of the tool and feed at 3 levels. When evaluating the experiments, we analysed the effect of the welding parameters on the forces during the process and the strength of the seam. Based on the results, the following conclusions can be drawn:

- Among the forces during welding, the dominant forces are the force in the feed direction (F_y) and the axial force (F_z).
- As rotational speed (n) and the n/v_f ratio are increased during welding, the force in the feed direction (F_y), the axial force (F_z) and the resultant welding force (F_r) decrease, while the strength of the weld increases.
- As feed (v_f) is increased, the force in the feed direction (F_y), the axial force (F_z) and the resultant welding force (F_r) increase, while the strength of the seam decreases.
- The best seam strength (10.69 MPa) was achieved with a rotational speed of 1000 1/min and a feed of 50 mm/min. This is 37% of the tensile strength of the bulk material.

Acknowledgements

This project was completed with the assistance the New National Excellence Program of the Ministry for Innovation and Technology (code: ÚNKP-22-3).

References

[1] Thomas W. M., Nicholas E. D., Needhan J. C., Murch M. G., Temple-Smith P., Dawes C. J.: *Friction-stir butt welding. "International patent application PCT/GB92/02203 and GB patent application 9125978.8."*. UK Patent Office, London 6. 1991.

[2] Kovács Zs., Hareancz F.: *Joining of non-weldable AA7075 and weldable AA6082 aluminium alloy sheets by friction stir welding*. IOP Conference Series: Materials Science and Engineering, 448/1. (2018) 012001. https://doi.org/10.1088/1757-899X/448/1/012001

[3] Çam G.: *Friction stir welded structural materials: beyond Al-alloys.* International Materials Reviews, 56/1. (2011) 1–48. https://doi.org/10.1179/095066010X12777205875750

[4] Salih O. S., Ou H., Sun W., McCartney D. G.: *A review of friction stir welding of aluminium matrix composites.* Materials & Design, 86. (2015) 61–71. https://doi.org/10.1016/j.matdes.2015.07.071

[5] Singh K., Singh G., Singh H.: *Review on friction stir welding of magnesium alloys*. Journal of magnesium and alloys, 6/4. (2018) 399–416. https://doi.org/10.1016/j.jma.2018.06.001

[6] Gangwar K., Ramulu M.: *Friction stir welding of titanium alloys: a review.* Materials & Design, 141. (2018) 230–255. https://doi.org/10.1016/j.matdes.2017.12.033

[7] Rao A. N., Naik L. S., Srinivas C.: *Evaluation and impacts of tool profile and rotational speed on mechanical properties of friction stir welded copper 2200 alloy.* Materials Today: Proceedings, 4/2. (2017) 1225–1229. https://doi.org/10.1016/j.matpr.2017.01.141

[8] Huang Y., Meng X., Xie Y., Wan L., Lv Z., Cao J., Feng J.: *Friction stir welding/processing of polymers and polymer matrix composites*. Composites Part A: Applied Science and Manufacturing, 105. (2018) 235–257. https://doi.org/10.1016/j.compositesa.2017.12.005

[9] Czigány T., Kiss Z.: *Friction stir welding of fiber reinforced polymer composites*. In: Proceedings of the 18th International Conference on Composite Materials, Jeju, South Korea, 2011. 21–26.

[10] Gibson B. T., Lammlein D. H., Prater T. J., Longhurst W. R., Cox C. D., Ballun M. C., Dharmaraj K. J., Cook G. E., Strauss A. M.: *Friction stir welding: Process, automation, and control.* Journal of Ma-

nufacturing Processes, 16/1. (2014) 56–73. https://doi.org/10.1016/j.jmapro.2013.04.002

[11] Arif M., Kumar D., Siddiquee A. N.: *Friction stir welding and friction stir spot welding of acrylonitrile butadiene styrene: A review.* Materials Today: Proceedings, 62/1. (2022) 300–308. https://doi.org/10.1016/j.matpr.2022.03.269

[12] Bagheri A., Azdast T., Doniavi A.: *An experimental study on mechanical properties of friction stir welded ABS sheets.* Materials & Design, 43. (2013) 402–409. https://doi.org/10.1016/j.matdes.2012.06.059

[13] Sadeghian N., Givi M. K. B.: *Experimental optimization of the mechanical properties of friction stir welded Acrylonitrile Butadiene Styrene sheets.* Materials & design, 67. (2015) 145–153. https://doi.org/10.1016/j.matdes.2014.11.032

[14] Mendes N., Loureiro A., Martins C., Neto P., Pires J. N.: *Morphology and strength of acrylonitrile butadiene styrene welds performed by robotic friction stir welding*. Materials & Design, 64. (2014) 81–90. https://doi.org/10.1016/j.matdes.2014.07.047

[15] Rudrapati R.: *Effects of welding process conditions on friction stir welding of polymer composites: A review.* Composites Part C: Open Access, 8. (2022) 100269. https://doi.org/10.1016/j.jcomc.2022.100269

[16] Gao J., Li C., Shilpakar U., Shen Y.: *Microstructure and tensile properties of dissimilar submerged friction stir welds between HDPE and ABS sheets.* The International Journal of Advanced Manufacturing Technology, 87. (2016) 919–927. https://doi.org/10.1007/s00170-016-8539-y

[17] Hajideh M. R., Farahani M., Ramezani N. M.: *Reinforced dissimilar friction stir weld of polypropylene to acrylonitrile butadiene styrene with copper nanopowder*. Journal of Manufacturing Processes, 32. (2018) 445–454. https://doi.org/10.1016/j.jmapro.2018.03.010

[18] KISTLER Multicomponent Dynamometer 9257b datasheet, 2009, Kistler Group

sciendo

Acta Materialia Transylvanica 6/1. (2023) 59–63.
DOI: Hungarian: https://doi.org/10.33923/amt-2023-01-10
English: https://doi.org/10.33924/amt-2023-01-10

ACTA MATERIALIA TRANSYLVANICA

Investigation of Bonded Joints in Glass Fiber Reinforced Flat Profiles

Valentin SZABÓ,[1] Dániel VACZKÓ[2]

[1] *John von Neumann Unversity, GAMF faculty, Department of Innovative Vehicles and Materials. Kecskemét, Hungary, szabo.valentin@gamf.uni-neumann.hu*

[2] *John von Neumann Unversity, GAMF faculty, Department of Innovative Vehicles and Materials. Kecskemét, Hungary, vaczko.daniel@gamf.uni-neumann.hu*

Abstract

Nowadays, raw material shortage is a characteristic problem that affects every sector of the industry. Composite materials reinforced with fiberglass, manufactured through the pultrusion process, have extremely favorable properties. In our research, we examined the application of surface treatments on pultruded profiles to enhance surface energy. We roughened the surfaces to be bonded using manual sanding and sandblasting techniques, and then performed wetting measurements using various degreasing agents. To demonstrate the occurrence of surface treatment and determine its magnitude, we inspected the surfaces with a roughness tester. The bonds were created using two different structural adhesives as well as epoxy resin. The shear strength values of the flat profiles were compared through tensile tests, and the effects of the surface treatments were determined. Based on the results, the appropriate surface treatment and adhesive type greatly influence the developed bond strength.

Keywords*: bonding, pultrusion, composite, surface energy, glass fibre.*

1. GFRP profiles

The profiles produced by pultrusion, which are glass fiber reinforced plastic (GFRP) composite materials, are used in the pultrusion process to manufacture continuous fiber-reinforced polymer matrix composites. During pultrusion, the fibers and resin are typically pulled through a heated die, where the resin cures and solidifies, taking on a solid shape.

The pultrusion process enables the production of high-strength, lightweight, and durable composite components and structural elements. This method is increasingly popular in the construction, automotive, electrical, and other industries that rely on strong, lightweight, and durable materials resistant to corrosion and chemicals. One of the main advantages of pultrusion is its ability to manufacture complex shapes with consistent dimensions and high precision, which is why more and more people choose this process for producing structural elements. Pultruded materials exhibit excellent corrosion and chemical resistance. Despite their low weight, these structural elements have high mechanical strength, providing them with great stability and reliability [1].

The surface energy of pultruded profiles is typically low due to the surface treatment applied during the manufacturing process. As a result, bonding such components can present a challenge. By implementing appropriate surface treatments, it is possible to increase the surface energy and the area of the bonded surface, thereby significantly improving the adhesion [2].

In our research, we treat the surfaces using manual sanding and sandblasting techniques, followed by cleaning with various degreasing agents. We examine the effects of these treatments through wetting angle measurements and surface roughness analysis, and then determine the shear strength of the bonded joint using a tensile testing machine.

The ratio of the length of the test specimen to the bonded area is 4:1. We applied this ratio based on the clamping length, so the bonded area is far enough from the clamping point. The flat profiles are 6mm thick, 50mm wide and 100mm

long. The bonding and clamping lengths are both 25mm. The bonded area is 1250mm2 in size. The required number of samples for the flat profile is listed in **Table 1.** We conducted three breaks for each type of test specimen. The labels of the test specimens are shown in the table below, where the numbers of breaks within each type of test specimen are indicated in parentheses.

2. Boundary surface analysis

One fundamental aspect of bond strength is the ability of the adhesive material to adequately wet the adherend surface. The wetting ability can be determined by the spreading of a liquid on a solid surface. The contact angle (θ) serves as a measurement of the contact angle formed at the interface of the three phases. The contact angle was examined on untreated, manually sanded and sandblasted surfaces. In their study **[3],** Stazi, F., Giampaoli, M., Rossi, M., and Munafò, P. achieved better results with manual sanding and sandblasting compared to untreated surfaces. Therefore, we roughened the test samples' surfaces using conventional manual sanding with P80 grit sandpaper.

2.1. Surface roughness measurement

We employed two types of surface roughening techniques on the test specimens: sandblasting and manual sanding, in addition to the untreated surface. To measure the surface roughness, we conducted roughness measurements on the roughened surfaces. The roughness we measured serves only to determine the differences between the surfaces.

Table 1. *Ahe labels used during the experiments*

Types of surface treatments	Types of adhesives		
	Loctite HY4090	Sikapower 4720	Ipox MR 3010 gyanta
Untreated	Lo_S_(1-3)	S_S_(1-3)	Gy_S_(1-3)
Sandblasted	Lo_H_(1-3)	S_H_(1-3)	Gy_H_(1-3)
Polished	Lo_Cs_(1-3)	S_Cs_(1-3)	Gy_Cs_(1-3)

Table 2. *Interpretation of the results obtained from the roughness test*

	Untreated	Polished	Sandblasted
R_a (µm)	1.77	3.72	3.73
R_z (µm)	8.38	21.51	22.20
R_t (µm)	11.22	31.73	33.63

We examined the surfaces using a Mitutoyo Formtracer SV-C3100 instrument. The average roughness (R_a) is twice as high for the sanded and sandblasted surfaces compared to the untreated surface. **Table 2** presents the averaged values obtained from the measurements.

The surface roughness parameter known as the peak-to-valley height (R_z) is significantly increased due to the surface treatments. In fact, compared to the untreated surface, this value has grown to slightly more than 2.5 times higher. When considering the average maximum peak-to-valley height (R_t), the values for the sanded and sandblasted surfaces are nearly three times higher than that of the smooth surface.

2.2. Wettability test

We captured the contact angle using a video camera. The droplets were applied to the surfaces using an Accumax Pro pipette, and we used distilled water as the probing liquid. The number of measurements we conducted is the product of the surface type and the number of cleaning agents (including one without any treatment). Therefore, we performed 12 measurements, using 3 droplets per measurement. The left and right contact angles were calculated using image analysis. We measured three different surface types: untreated, sandblasted, and manually sanded surfaces. In terms of degreasing, we applied four cleaning methods. Initially, we examined an untreated surface as a reference for comparing the different degreasing agents. We used two types of degreaser: acetone and Loctite Super Cleaner cleaning spray, as well as methanol as an alcohol-based degreaser **[4]**.

The images of the two extreme values obtained from the measurements can be seen in **Figure 1.** The droplet with the highest spreading occurred on the smooth surface without degreasing, while the other image shows the least spreading droplet on the sanded surface without degreasing.

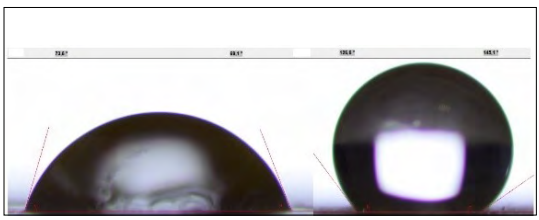

Figure 1. *The most widely spread (left) and the least widely spread (right) drop during the measurements.*

There are significant differences among the results. The most wettable surface was the untreated surface without any surface treatment or degreasing. We observed that the untreated surface showed better results compared to the other cleaning surfaces when Loctite Super Cleaner cleaning spray was applied, but still not better than the untreated surface without degreasing. For the manually sanded and sandblasted surfaces, degreasing with methanol proved to be the most effective, as it resulted in an average contact angle of 94.18° for the sanded surface and 94.25° for the sandblasted surface. In the case of the roughened surfaces, we noticed that acetone showed approximately 8-9° higher values compared to methanol in terms of contact angle deviation.

Based on the measured results, the wetting ability of the untreated surface without any treatment or degreasing reached the partially wettable range with contact angle values below 90°. Since the spreading of adhesives depends on viscosity, it would be beneficial to intervene. Some adhesive manufacturers specify in the instructions for use the spreading/application of the adhesive, for example, using a plastic spreader.

3. Measurements and test results

During the measurements, we compared different surface roughnesses by bonding the surfaces together, with a bonded area of 1250 mm^2 for each test specimen. We then conducted tensile tests. The measurements that yielded the best results were repeated with test specimens of two- and three-fold sizes to examine whether we obtain linearly increasing values.

The measurements were performed on an Instron 5900R 4482 tensile testing machine. For each measurement type, three tensile tests were conducted. In terms of shear strength, the performance of the adhesives was 17 N/mm^2 for Loctite (on steel test specimens), 14 N/mm^2 for Sikapower, while there is no factory-specified value for shear strength for the resin.

Based on the measurements on the untreated test specimens, the maximum load remained below 5000 N. For Loctite, two out of three tests yielded similar values (3113.1 N and 3118.3 N), while the third test resulted in a value that was approximately 800 N lower. The results obtained for Sikapower showed a higher variation, with the smallest result being 3097.3 N and the largest result being 4958.9 N. The resin exhibited the smallest variation, with values ranging between 2570.3 N and 3221.5 N. In terms of failure modes, the adhesive completely separated from the bonded surface in all cases. The values obtained for the untreated surfaces and the types of failures are shown in **Table 3.**The results obtained for the polished surfaces consistently showed lower values compared to the sandblasted surfaces, but they exhibited twice the load resistance compared to the untreated surfaces. The measurements results are shown in **Table 4.** In comparison to the untreated surfaces, the load resistance doubled, but complete detachment was still observed. The load values increased twofold compared to the untreated surfaces, but there was no difference in the nature of failure.

The results obtained on the sandblasted surfaces were better than the previous ones, as all three adhesions increased at least threefold compared to the smooth surface. The bonds made with Loctite adhesive and resin showed similar values. The Sikapower bond performed well compared to itself, as it not only showed more than three times the strength of the smooth surface bonding, but also achieved 93% of the maximum shear strength value provided by the manufacturer. **Table 5** shows the values of the results obtained on the sandblasted surfaces and the types of failures.

We observed significant improvement in the quality of the bonded joint when using Sikapower adhesive on the test specimens. Besides the bond-

Table 3. *Results obtained on untreated surface*

Sample labeling	Mean maximum load (N)	Shear strength (N/mm^2)	Failure types
Resin untreated	2907.9	2.33	Peeled off the entire surface
Loctite untreated	2841.9	2.27	Peeled off the entire surface
Sikapower untreated	4896.7	3.92	Peeled off the entire surface

Table 4. *Results obtained on polished surfaces*

Sample labeling	Mean maximum load (N)	Shear strength (N/mm^2)	Failure types
Resin polished	6060.7	4.85	Peeled off the entire surface
Loctite-polished	7345.7	5.88	Peeled off the entire surface
Sikapower-polished	9115.1	7.29	Peeled off the entire surface

ed joint, the failure occurred in the counterbored hole profile, as shown in **Figure 2.**

The ratio of adhesive to cohesive failures was approximately 60-40%. In the case of resin adhesive, there was a minimal occurrence of cohesive failure. Compared to smooth surfaces, the sandblasted surfaces exhibited more than three times the shear stress values, which was consistent for all three types of adhesives. The Sikapower adhesive almost met the factory shear stress specification, as we measured an average of 93% of the specified value on the test specimens.

In **Figure 3** it is evident that the surfaces treated with sandblasting resulted in the strongest bond. During fracture, both adhesive and cohesive failures occurred on the sandblasted rough surface. When testing flat profiles, the combination of Sikapower adhesive and sandblasted surface treatment yielded the highest result. Therefore, further investigation was conducted using this combination. In the subsequent analysis, we increased the surface roughness and examined how shear forces followed this modification.

Table 5. *Results obtained on sandblasted surfaces*

Sample labeling	Mean maximum load (N)	Shear strength (N/mm^2)	Failure types
Resin-sandblast.	8851.4	7.08	Partially peeled off
Loctite-sandblast.	8987.2	7.19	Peeled off the entire surface
Sikapower-sandblast.	16339	13.07	Partially peeled off

Figure 2. *The partially peeled off adhesive bond on the sandblasted profile with Sikapower adhesive.*

4. Conclusions

The effectiveness of adhesive technology is most influenced by a properly prepared surface. In our case, the interface with low surface energy was removed using simple surface treatment (roughening) procedures, thus increasing both the surface energy and the bonding area. This resulted in a surface area favourable to bonding. In this way, the sandblasted specimens showed an improvement of over 300% over the untreated surface for all three types of adhesive. Sandblasted surfaces bonded with Sikapower performed best. There are two possible reasons for this, one is that sandblasting creates a more homogeneous surface roughness distribution, resulting in a more uniform bond. The other possible reason is that Sikapower adhesive contains 0.25mm spacer glass beads, which provide the optimum bonding gap during bonding. This ensures that the correct gap is almost guaranteed when forming the bonded joint.

Acknowledgements

The research presented in the article was created with the support of the grant numbered 2020-1.1.2-PI-ACI-KFI-2020-00052. The project was implemented within the framework of the call announced by the Ministry of Innovation and Technology and the National Research, Development and Innovation Office.

References

[1] Encinas N., Lavat-Gil M., Dillingham R. G., Abenojar J., Martínez M. A.: *Cold plasma effect on short glass fibre reinforced composites adhesion proper-*

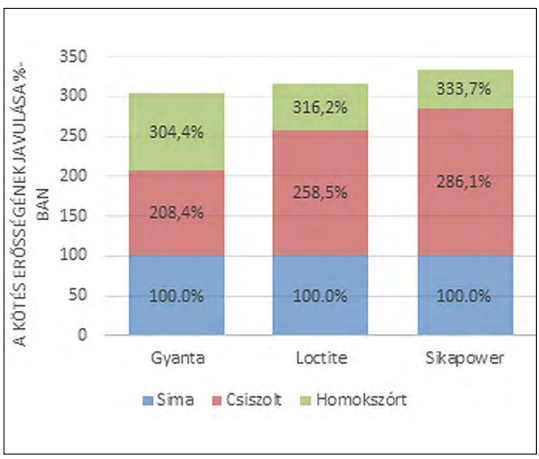

Figure 3. *Effect of surface treatments compared to untreated surface.*

ties. International Journal of Adhesion and Adhesives, 48. (2014) 85–91. https://doi.org/10.1016/j.ijadhadh.2013.09.026

[2] Volk M., Yuksel O., Baran I., Hattel J. H., Spangenberg J., Sandberg M.: *Cost-efficient, automated, and sustainable composite profile manufacture: A review of the state of the art, innovations, and future of pultrusion technologies*. Composites Part B: Engineering, 246. (2022) 110135. https://doi.org/10.1016/j.compositesb.2022.110135

[3] Stazi F., Giampaoli M., Rossi M., Munafò P.: *Environmental ageing on GFRP pultruded joints: comparison between different adhesives.* Composite Structures, 133. (2015) 404–414. https://doi.org/10.1016/j.compstruct.2015.07.067

[4] Berczeli M., Weltsch Z.: *Enhanced wetting and adhesive properties by atmospheric pressure plasma surface treatment methods and investigation processes on the influencing parameters on HIPS polymer*. Polymers, 13/6. (2021) 901. https://doi.org/10.3390/polym13060901